

Design, Fabrication, and Analysis of a Multi-Layer,
Low-Density, Thermally-Invariant Smart Composite via
Ultrasonic Additive Manufacturing

A Thesis

Presented in Partial Fulfillment of the Requirements for
the Degree Master of Science in the
Graduate School of The Ohio State University

By

Joshua D. Pritchard, B.S.

* * * * *

The Ohio State University

2014

Master's Examination Committee:

Dr. Marcelo Dapino, Adviser

Dr. Mark Walter

Approved by

Adviser

Graduate Program in
Mechanical Engineering

© Copyright by
Joshua D. Pritchard
2014

ABSTRACT

Smart materials are a class of materials that couple different regimes, such as thermal, mechanical, electrical, and magnetic. Shape memory alloys (SMAs) are classified as such due to their ability to couple the thermal and mechanical regimes. One particular type of SMA is nickel-titanium (NiTi), which can recover up to 8% elastic strain. In this study, the large strain recovery of NiTi is used in the development of a metal matrix composite that exhibits low to near-zero coefficient of thermal expansion. This is done by utilizing the strain recovery of NiTi fibers to offset the expansion of the aluminum matrix in which they are embedded. The fabrication of this metal matrix composite is made possible through the use of ultrasonic additive manufacturing (UAM).

Ultrasonic additive manufacturing combines ultrasonic welding with subtractive machining operations to create complex parts from dissimilar metals. The resulting parts can be made of similar or dissimilar materials. In UAM, 20kHz vibrations created by piezoelectric transducers are transferred to a textured steel horn, which presses a thin strip of metal to a substrate with a normal force in excess of 5000 Newtons. Under these conditions, the surface oxides and asperities are broken down, producing atomically clean faces on both pieces, allowing for pure metal-to-metal contact and instantaneous bonding to take place. Unique to UAM is its low-temperature, solid-state operation, which means no melting of the constituent materials takes place.

This feature provides the unprecedented opportunity to embed materials that are thermally sensitive, such as SMAs.

This study focuses on the fabrication and characterization of NiTi-Al UAM composites with an emphasis on developing a method of producing composite structures. Process parameters that were studied include securing the NiTi ribbons during fabrication, ensuring proper placement of the ribbons in the composite, and applying the necessary pre-stress to produce the appropriate recovery strain in the SMA. In addition, the weld parameters and the surface treatment of the NiTi ribbons were tested via fiber pull-out tests to quantify the bond strength between the fibers and matrix. Characterization of the composites was conducted to obtain experimental values for thermal diffusivity, electrical conductivity, and coefficient of thermal expansion (CTE). The CTE was measured in a thermal chamber by recording strain variations via strain gages over given temperature variations. The final focus of this study was an analysis between the experimental results from these methods and NiTi-Al composite characterization models.

ACKNOWLEDGMENTS

I would like to begin by thanking and acknowledging those who have helped and supported me thus far in my life. For without them, I surely would not be where I am today.

First, thank you God, for Your many blessings each and everyday of my life. You have given me the many family, friends, mentors, and colleagues that I turn to so often for guidance and support. All the skills I have utilized to achieve so many things are also a gift from You, and I am very grateful.

Thank you Prof. Marcelo Dapino, my research advisor, for the opportunity to be a member of the Smart Materials and Structures Lab. I will always appreciate your willingness to share your passion and knowledge of intelligent materials and structures with me. You have provided the opportunity to grow both as a professional and as a technical engineer. In addition, thank you Prof. Dapino and Prof. Mark Walter for being the members of my thesis committee.

My family, you are by far the most important people in my life, and it is your support that I am most thankful for when it comes to my life. You have always been by my side to help make my life a success. Thank you to my parents, Yvonne and Dave, and my step-parents, Cheryl and Jim, for the unending encouragement to follow my heart and strive for whatever it desires. Heather, my sister, I appreciate

you more than I think you know, as you have been an excellent role model and given me courage over the years.

Sarah, I appreciate all your help throughout the time spent on this study and document. You were always there to assist me in whatever capacity I needed you. Whether listening to me or bringing meals to me late at the lab, you continuously supported my research and the tasks I undertook outside of it.

My friends, you have always maintained a presence in my life and been there to listen and be interested in me and my work. Your never-ending support of my goals in life is something that I will not forget. I also appreciate you providing many opportunities to relax during the pursuit of my M.S.

Finally, thank you to the many others who have aided my research. Dr. Phillip Evans, I appreciate your continued willingness to support the project on which my research was focused. Thanks to Cameron Benedict and Mark Norfolk of Fabrisonic, LLC. for the many enlightening conversations and for assisting with the ultrasonic additive manufacturing efforts. Walter Green, I thank you for your many insightful recommendations and assistance during the many hours I spent working in the machine shop. In addition, thanks to Chad Bivens, Kevin Wolf, Steve Bright, and Ross Baldwin for providing machining and microscopy assistance. The students in the Smart Materials and Structures Lab, thank you for making the time I spent on my master's degree enjoyable. The OSU UAM Center staff, Adam Hehr, Justin Scheidler, and Paul Wolcott, I am glad we got to work together as I learned a lot from each of you and enjoyed the company.

VITA

June 8, 1988Born - Massillon, Ohio

June 2007 Honors Diploma, Perry High School

June 2012 B.S. Mechanical Engineering Cum
Laude, The Ohio State University

December 2013 Engineering Intern / Passed Funda-
mentals of Engineering Examination

FIELDS OF STUDY

Major Field: Mechanical Engineering

Studies in Smart Materials and Structures: Dr. Marcelo Dapino

Major Field: Mechanical Engineering

TABLE OF CONTENTS

	Page
Abstract	ii
Acknowledgments	iv
Vita	vi
List of Tables	x
List of Figures	xii
Chapters:	
1. Introduction	1
1.1 Thesis Organization	1
1.2 Purpose / Motivation	1
1.3 Shape Memory Alloys	2
1.4 Metal Matrix Composite Fabrication Techniques	7
1.4.1 Casting	8
1.4.2 Rolling and Swaging	8
1.4.3 Ultrasonic Additive Manufacturing	11
2. Design of Composites via Shape Memory Alloy and Shape Memory Alloy Composite Models	16
2.1 SMA Bivariant Constitutive Model	16
2.1.1 Brinson Model	16
2.1.2 Hahnlen Model	18
2.2 SMA Composite Model	20
2.3 Composite Model Implementation for Composite Design	24
2.3.1 Design of Al-NiTi Composites	24

3.	Fabrication of Multi-Layer Al-NiTi Composites	31
3.1	Material Detwinning	31
3.1.1	Pseudoelastic Nickel-Titanium	31
3.1.2	Shape Memory Nickel-Titanium	34
3.2	Consolidation Methods	37
3.2.1	Coupon Samples	37
3.2.2	Large Geometry Samples	40
3.3	Consolidation Results	41
3.3.1	Coupon Samples	41
3.3.2	Large Geometry Samples	47
3.4	Sample Removal and Post-Processing Procedures	51
3.4.1	Coupon Samples	51
3.4.2	Large Geometry Samples	54
4.	Testing and Results of Multi-layer Al-NiTi Composites	60
4.1	Coefficient of Thermal Expansion Testing	60
4.1.1	Test Set-Up and Procedure	60
4.1.2	Results	62
4.1.3	Differential Scanning Calorimetry Tests	70
4.1.4	Microscopy	73
4.1.5	Comparison of Composite Performance to SMA Composite Model	77
4.2	Thermal Diffusivity	85
4.2.1	Test Set-Up and Procedure	85
4.2.2	Results	88
4.3	Electrical Resistivity	91
4.3.1	Test Set-Up and Procedure	91
4.3.2	Results	92
5.	Conclusion	95
5.1	Summary of Work	95
5.2	Future Work	97
	Bibliography	100

Appendices:

A.	Characterization of NiTi Material	103
A.1	Isothermal Tensile Tests	103
A.2	Differential Scanning Calorimetry	104
A.3	Phase Diagram Development	106
B.	Mechanical Drawings of Parts and Fixtures	112
C.	Coefficient of Thermal Expansion Test Results	123

LIST OF TABLES

Table		Page
1.1	Materials that exhibit negative thermal expansion or low coefficients of thermal expansion, the percent volume fraction required if embedded in aluminum, the density of each, and the temperature at which the given NTE or low CTE is observed. CTE data provided by matweb.com and Takenaka [21]. *Measurement is an average of anisotropic properties.	3
2.1	Material parameters for shape memory NiTi fibers used in NiTi-Al composites.	25
2.2	Material parameters for pseudoelastic NiTi fibers used in NiTi-Al composites.	26
3.1	Laser parameters used for the ablation of aluminum to make channels for the large geometry composites.	41
4.1	NiTi material type, fiber size, and NiTi volume fraction data on coupon composites produced for testing. Note: The numbering for the shape memory composites begins at 6, as previous composites had been built by a previous researcher within the lab.	61
4.2	CTE results for various pseudoelastic NiTi and shape memory NiTi composites. These results are reported $\pm 2.4 \mu\epsilon/^\circ\text{C}$ at 95% confidence. *Temperature range for CTE calculation was from 65°C to 125°C , as the transformation region was observed over this range. **Solder joint on strain gage wire failed during cooling portion of cycle. . . .	69
4.3	Thermal diffusivity results and comparison to the theoretical diffusivity for 6061 UAM aluminum in the out-of-plane direction.	89

4.4	Thermal diffusivity results and comparison to the theoretical diffusivity for 6061 UAM aluminum in the rolling direction.	89
4.5	Thermal diffusivity results and comparison to the theoretical diffusivity for 6061 UAM aluminum in the transverse direction.	90
4.6	Thermal diffusivity results for an Al-pseudoelastic NiTi composite with 14.0% austenitic NiTi material.	91
4.7	Resistivity results for 3003-H18 aluminum tape, UAM 3003-H18 aluminum in out-of-plane direction, and composite P-2 in rolling direction.	92

LIST OF FIGURES

Figure		Page
1.1	Phase transformation cycle of NiTi. The cycle begins in the low-temperature martensite phase, M, where the material can be loaded to form detwinned martensite, M+. By applying heat, the detwinned martensite can transform into austenite and recover the deformation caused via detwinning. Cooling the austenite returns the material to martensite again. Direct heating of the martensite can also cause the transformation to austenite. Finally, austenite can transform to detwinned martensite by inducing strain.	4
1.2	Example of phase diagram, stress (σ) versus temperature (T), for nickel-titanium. The temperature values of M_f , M_s , A_s , and A_f , represent the martensite finish, martensite start, austenite start, and austenite finish temperatures, respectively. The critical start and finish stresses are given as σ_{cr}^s and σ_{cr}^f respectively. C_M represents the martensite stress influence coefficient while C_A is the coefficient for austenite.	5
1.3	Stress vs. strain vs. temperature plot for transformation curves of shape memory and pseudoelastic NiTi.	7
1.4	Mold used by Furuya et al. for aligning TiNi fiber during casting process to produce TiNi / Al composite [5].	9
1.5	Micrograph of a typical cross section of the TiNi / Al-1100 composite produced by Furuya et al. [5].	9
1.6	Production of composite with NTE fibers by rolling as proposed by Jin and Mavoori [11].	10
1.7	Production of composite with NTE fibers by swaging as proposed by Jin and Mavoori [11].	10

1.8	Time lapse of foil surfaces during ultrasonic welding process.	12
1.9	Ultrasonic additive manufacturing process. [a] Ultrasonic welding system welds metal tapes to base plate; [b] successive welding of tapes over multiple layers builds solid part; [c] periodic subtractive machining shapes and maintains uniform welding surface. Illustrations courtesy of Fabrisonic, LLC.	13
1.10	Cross-section of part made on 1 kW power UAM machine.	14
1.11	Cross-section of part made on 9 kW power UAM machine.	15
1.12	Ultrasonic additive manufacturing system housed at The Ohio State University's UAM Center. This system produces 9 kW of ultrasonic power.	15
2.1	Phase diagrams of NiTi according to (a) Liang and Rogers model [14] and (b) Brinson's bivariant model [3].	18
2.2	Phase diagrams of NiTi according to (a) Brinson's bivariant model [3] and (b) Hahnlen's new bivariant model [6].	20
2.3	Diagram of composite theory based on (top) no initial preload of NiTi fibers before being embedded and (bottom) prestrain applied to NiTi before being embedded.	22
2.4	Composite performance model results for Al-NiTi composite manufactured with 7.0% to 9.0% shape memory NiTi fibers.	25
2.5	Composite performance model results for Al-NiTi composite manufactured with 15.6% to 17.6% pseudoelastic NiTi fibers.	27
2.6	Cross-sections (as viewed from side) and effects of ribbon concentration on composite expansion.	29
2.7	Cross-sections and effects of asymmetric fiber placement on composite expansion, where the dashed-dot lines represent an axis of symmetry.	30
2.8	Example of cross-section style deployed in the Al-NiTi composites within this study.	30

3.1	Ribbon pack used for collecting and arranging the NiTi ribbons to be embedded into the aluminum matrix.	33
3.2	Clamps used for detwinning packs of pseudoelastic NiTi ribbons. The upper clamp was threaded into a cantilever fixture while weights were suspended from the lower clamp.	33
3.3	Assemblies used in transferring ribbons (either detwinned or twinned) from one location to another without the geometry being affected or strain recovered in the process.	35
3.4	Backbones of coupon style (upper) and large geometry style (lower) transfer assemblies.	35
3.5	Ribbon clamps used as part of the transfer assemblies to maintain geometry and prestrain on the base plate. (Top left) Upper ribbon clamp for coupon size samples, (Top right) upper ribbon clamp for large geometry samples, and (Bottom) lower ribbon clamp.	36
3.6	Base plates used for the production of coupon-size (left) and large geometry (right) Al-NiTi composites.	36
3.7	Load frame used for the detwinning of shape memory NiTi ribbons.	38
3.8	Production of coupon-sized sample before welding pass with ribbons lying on structure surface.	39
3.9	Production of coupon-sized sample following the milling of channels for the NiTi ribbons.	39
3.10	Rendering of the large geometry composites used to develop fabrication methods for pieces approximately 27.31 cm (10.75") in length and 0.64 cm (0.25") tall. Concentration of ribbons within center provides appropriate area of study.	41
3.11	UAM machine's Nd:YVO ₄ laser system in use to make channels in large geometry composites.	42
3.12	Example of channel pattern formed by the UAM machine's laser system.	42

3.13	Bunching of ribbons after a welding pass without the use of channels to maintain ribbon placement.	44
3.14	Area where aluminum did not weld because the ribbons kept the aluminum tape from making appropriate contact with the structure.	44
3.15	NiTi ribbons splitting through an aluminum tape. This defect occurred when the aluminum failed around the harder NiTi material. .	45
3.16	Failure of ribbon encapsulation (center ribbons) when the channel depth was too great. Failure allowed for ribbons to be pulled from the channels or be rotated within them.	46
3.17	Extenal view of delamination within a composite.	47
3.18	Cross-sectional view of delamination failure. The crack propagation from the corners of the NiTi fibers are the result of stress concentrations at the shape geometric changes.	48
3.19	Area within the first large geometry sample, where aluminum did not weld to underlying structure.	49
3.20	Failure of aluminum to weld to composite structure in the second large geometry sample.	50
3.21	Defect at a corner within the second attempt at large geometry build produced by the face mill catching a loose tape end and ripping a portion of the structure apart. Following weld attempts over this region were unsuccessful, because the uneven surface prevented bonding from occurring.	50
3.22	Defects along the seam lines within the composite due to an uneven surface, which could not be repaired as recovery of the surface would result in additional damage to the corner defect already present. . .	51
3.23	Coupon size sample following CNC milling operations within the UAM machine to mill the component to the proper width.	52
3.24	Milling operation using a four-flute, 0.63 cm (1/4") diameter, square, carbide, end-mill to remove the build plate from the composite structure.	53

3.25	Coupon sample following the removal of build plate using milling and vertical band saw. The only remaining parts are found of the ends of the composite.	54
3.26	SXJ2 Precision Wire Saw used to trim off the ends of the coupon samples.	55
3.27	Example of final coupon sized Al-NiTi composite produced via UAM.	55
3.28	Large geometry sample following CNC milling operations within the UAM machine to achieve the desired outline.	56
3.29	Large sample following the drilling of holes and the milling of a slot.	57
3.30	Haas ® CNC milling machine, removing the build plate from the large geometry sample.	58
3.31	Fixture used for securing the build plate of the large samples while CNC milling operations were performed to remove sections of the build plate from the composite.	58
3.32	Pockets produced by the removal of the build plate from the large geometry composites. Bridges were left to maintain stability during milling operation, and later removed once the pockets were completed.	59
3.33	Final large geometry part produced following the electrical discharge machining of the composite ends.	59
4.1	Set-up used for conducting coefficient of thermal expansion tests on coupon sized Al-NiTi composites.	63
4.2	Al-NiTi composite sample and reference aluminum sample mounted in cantilever position for performing CTE tests.	63
4.3	Example of CTE testing results for the top strain. C-7's results are shown here.	66
4.4	Example of CTE testing results for the bottom strain. C-7's results are shown here.	66

4.5	Example of CTE testing results for the average strain. C-7's results are shown here.	67
4.6	Stress-temperature plot of C-9's first cycle during CTE testing with fitted lines over the transformation region.	68
4.7	Plot of C-9's instantaneous CTE versus temperature based on the derivatives of the fitted lines in Figure 4.6.	68
4.8	Example of samples cut for performing differential scanning calorimetry testing. Samples from P-3 are shown.	71
4.9	TA Instruments 2920 Differential Scanning Calorimetry system utilized for carrying out DSC tests.	72
4.10	Buehler, Isomet, Low-speed, rotary saw with a diamond coated blade used for cutting of Al-NiTi DSC samples.	72
4.11	Results of the DSC tests performed on the pseudoelastic NiTi ribbons, composite P-3, and composite P-5.	73
4.12	Series of optical micrographs taken of C-7's cross-section prior to being thermally cycled.	74
4.13	Series of optical micrographs taken of C-7's cross-section after being thermally cycled via the CTE test process. The micrographs are in reversed order from Figure 4.12 and mirrored due to the samples coming from opposite sides of a cutting plane.	75
4.14	Series of optical micrographs taken of C-9's cross-section prior to being thermally cycled.	76
4.15	Image of the failed fiber-matrix interfaces within C-9, as the fibers are no longer flush with the matrix's face.	76
4.16	Series of optical micrographs taken of C-9's cross-section after being thermally cycled via the CTE test process. The micrographs are in reversed order from Figure 4.12 and mirrored due to the samples coming from opposite sides of a cutting plane.	76

4.17	Plot of C-7's average strain on its first cycle compared to the SMA composite model results for an Al-NiTi composite of 19.8% NiTi material.	79
4.18	Plot of C-7's average strain on its first cycle compared to the SMA composite model results for an Al-NiTi composite of 8.9% NiTi material.	80
4.19	Plot of C-7's average strain on its first cycle compared to the SMA composite model results for an Al-NiTi composite of 8.9% NiTi material and the inclusion of an initial stress of 400 MPa.	81
4.20	Plot of C-9's average strain on its first cycle compared to the SMA composite model results for an Al-NiTi composite of 7.9% NiTi material.	82
4.21	Plot of C-9's average strain on its first cycle compared to the SMA composite model results for an Al-NiTi composite of 7.9% NiTi material and the inclusion of an initial stress of 350 MPa.	83
4.22	Plot of C-9's average strain on its first cycle compared to the SMA composite model results for an Al-NiTi composite of 6.4% NiTi material and the inclusion of an initial stress of 350 MPa.	84
4.23	Illustration of how the flash method for the determination of thermal diffusivity works.	86
4.24	Anter Flashline-5000 Thermal Diffusivity Meter used to perform the thermal diffusivity tests.	86
4.25	Rendering of UAM Al thermal diffusivity samples as cut from a larger UAM Al piece, where a, b, and c are the rolling, transverse, and out-of-plane directions respectively.	87
4.26	Rendering of UAM Al-NiTi thermal diffusivity sample in the out-of-plane direction.	87
4.27	UAM 6061-Al samples cut and machined for thermal diffusivity testing where a, b, and c are the rolling, transverse, and out-of-plane directions respectively.	87
4.28	UAM Al-NiTi thermal diffusivity sample in the out-of-plane direction.	88

4.29	Voltage versus current and fitted curve for 3003-H18 Al tape.	93
4.30	Voltage versus current and fitted curve for UAM 3003-H18 Al in the out-of-plane direction.	93
4.31	Voltage versus current and fitted curve for Al-NiTi composite P-2. . .	94
A.1	Example of stress versus strain as a result of data analysis from a isothermal tensile tests at various temperatures. Result of SMA material is shown.	105
A.2	Example of heat flow per mass versus temperature plot as the result of differential scanning calorimetry tests. SMA material is shown. . .	106
A.3	Example of stress versus strain plot after regression analysis conducted on the various regions of the curve. SMA material at 30°C cycle temperature shown.	108
A.4	Example of transformation points gathered from the intersection of regression lines on a stress versus strain plot. SMA material at 30°C cycle temperature shown.	108
A.5	Example of the determination of the stress influence coefficients from the stress versus temperature plot produced using the collected transformation data of the isothermal tensile tests. SMA material is shown.	109
A.6	Example of the determination of the critical starting and finishing stresses from the stress versus temperature plot produced using the collected transformation data of the isothermal tensile tests. SMA material is shown.	110
A.7	Example of using regression analysis to determine the transformation temperatures of NiTi material at zero stress. SMA material is shown.	110
A.8	Pseudoelastic NiTi material phase diagram produced via the characterization process outlined in Appendix A.	111
A.9	Shape memory NiTi material phase diagram produced via the characterization process outlined in Appendix A.	111

B.1	Dimensional drawing of base plate for producing coupon samples. Sheet 1 of 2.	113
B.2	Dimensional drawing of base plate for producing coupon samples. Sheet 2 of 2.	114
B.3	Dimensional drawing of base plate for producing large geometry sam- ples. Sheet 1 of 2.	115
B.4	Dimensional drawing of base plate for producing large geometry sam- ples. Sheet 2 of 2.	116
B.5	Dimensional drawing of coupon size transfer assembly backbone. . .	117
B.6	Dimensional drawing of large geometry transfer assembly backbone.	118
B.7	Dimensional drawing of upper ribbon clamp used in coupon size trans- fer assembly.	119
B.8	Dimensional drawing of upper ribbon clamp used in large geometry transfer assembly.	120
B.9	Dimensional drawing of bottom ribbon clamp used in both coupon size and large geometry transfer assemblies.	121
B.10	Dimensional drawing of fixture design to assist in the removal of the build plate from the large geometry samples.	122
C.1	Plot of strain versus temperature results for bottom strain gage during CTE test of P-1.	124
C.2	Plot of strain versus temperature results for top strain gage during CTE test of P-1.	124
C.3	Plot of the average strain versus temperature results from the CTE test of P-1.	125
C.4	Plot of strain versus temperature results for bottom strain gage during CTE test of P-2.	126

C.5	Plot of strain versus temperature results for top strain gage during CTE test of P-2.	126
C.6	Plot of the average strain versus temperature results from the CTE test of P-2.	127
C.7	Plot of strain versus temperature results for bottom strain gage during CTE test of P-4.	127
C.8	Plot of strain versus temperature results for top strain gage during CTE test of P-4.	128
C.9	Plot of the average strain versus temperature results from the CTE test of P-4.	129
C.10	Plot of strain versus temperature results for bottom strain gage during CTE test of C-7.	130
C.11	Plot of strain versus temperature results for top strain gage during CTE test of C-7.	131
C.12	Plot of the average strain versus temperature results from the CTE test of C-7.	132
C.13	Plot of strain versus temperature results for bottom strain gage during CTE test of C-9.	132
C.14	Plot of strain versus temperature results for top strain gage during CTE test of C-9.	133
C.15	Plot of the average strain versus temperature results from the CTE test of C-9.	134

CHAPTER 1

INTRODUCTION

1.1 Thesis Organization

This thesis presents the design, manufacturing, and testing methods utilized to produce a low-density, thermally-invariant composite. The discussion of these topics is broken up into three chapters: Chapter 2 reviews the materials considered and the design models, Chapter 3 covers the manufacturing process, and Chapter 4 summarizes the test procedures used in this study and results. Concluding remarks are presented in conjunction with future work in Chapter 5.

1.2 Purpose / Motivation

There is a demand for systems that can be used in environments which require dimensional stability and high strength, while meeting increasing demands for structures with low density. Advancements in materials research has allowed for the first two requirements to be met with the use of Invar-36 ®, an iron-based material, whose coefficient of thermal expansion (CTE) is between 0.1 and 1.0 microstrain per degree Celsius, [$\mu\epsilon/^\circ\text{C}$] [21]. However, because of its iron-base, Invar-36 ® is dense, keeping it from meeting the need of a light weight material. Aside from Invar-36 ®, there are

a variety of other materials that exhibit low and even negative coefficients of thermal expansion (NTE), Table 1.1, but the majority of them lack the strength necessary for a stand-alone material.

The proposed material is a metal matrix composite (MMC) whose matrix is aluminum, a material that has a low-density and high strength, and whose fibers are NiTi, a shape memory alloy. NiTi was chosen for its durability as a metal, ability to recover large strains, and the low volume fraction required within the aluminum matrix to achieve a material that has a CTE between -5 and 5 $\mu\epsilon/^\circ\text{C}$. The estimated amounts of each material required within an aluminum matrix are based on a rule of mixtures [2, 7, 11, 16, 25]:

$$\alpha_{\text{comp}} = \nu\alpha_{\text{fiber}} + (1 - \nu)\alpha_{\text{Al}} \quad (1.1)$$

where the CTE of the composite (α_{comp}) is a sum of the products of each material's CTE and its corresponding volume fraction, ν and $(1 - \nu)$ for the fiber and matrix respectively.

1.3 Shape Memory Alloys

Shape memory alloys (SMAs) are a class of smart materials known for their mechanical properties' high dependence upon temperature and the ability to memorize trained shapes. Nickel-titanium (NiTi) is a particular type of SMA that can recover strains up to 8% [1, 17] and experience changes in elastic modulus from the martensite to austenite phase by as much as 500%. The recovery of such large strains is the result of temperature and stress-induced phase transformations between a low-temperature martensite phase and a high-temperature austenite phase, Figure 1.1.

Table 1.1: Materials that exhibit negative thermal expansion or low coefficients of thermal expansion, the percent volume fraction required if embedded in aluminum, the density of each, and the temperature at which the given NTE or low CTE is observed. CTE data provided by matweb.com and Takenaka [21]. *Measurement is an average of anisotropic properties.

Material	CTE [$\mu\epsilon/^\circ\text{C}$]	% Req'd	Density [g/cc]	Temp. Range [$^\circ\text{C}$]
NiTi	—	17.2	6.45	—
Kevlar 29	-2.2	66.8	1.44	—
Kevlar 49	-4.9	64.6	1.44	—
α -ZrW ₂ O ₈	-9.0	56.9	5.09	<152
β -ZrW ₂ O ₈	-6.0	62.1	—	152 – 757
β -eucryptite	-1.0 – -6.0*	75.0	2.53	26 – 626
Cd(CN) ₂	-33.5	31.9 – 49.5	2.23	-103 – 102
ReO ₃	-0.7	76.6	6.92	<-53
(HfMg)(WO ₄) ₃	-2.0	72.0	—	23 – 797
Sm _{2.75} C ₆₀	-100.0	14.6 – 22.8	—	<-243
Bi _{0.95} La _{0.05} NiO ₃	-82.0	17.2 – 26.7	—	47 – 107
Fe-36Ni	0.1 – 1.0	78.6	—	<227
Fe ₃ Pt	-30.0 – -6.0	34.0 – 62.1	—	-173 – 147
Tm ₂ Fe ₁₆ Cr	-9.0*	70.3	—	67 – 107
CuO	-36.0*	30.5 – 47.4	6.315	<-123
Mn ₃ Cu _{0.53} Ge _{0.47} N	-16.0	46.2 – 72.0	—	-8 – 67
Mn ₃ Zn _{0.4} Sn _{0.6} N _{0.85} C _{0.15}	-23.0	39.2 – 60.8	—	-3 – 62
Mn ₃ Zn _{0.4} Sn _{0.5} N _{0.85} B _{0.05}	-30.0	34.0 – 52.6	—	7 – 67

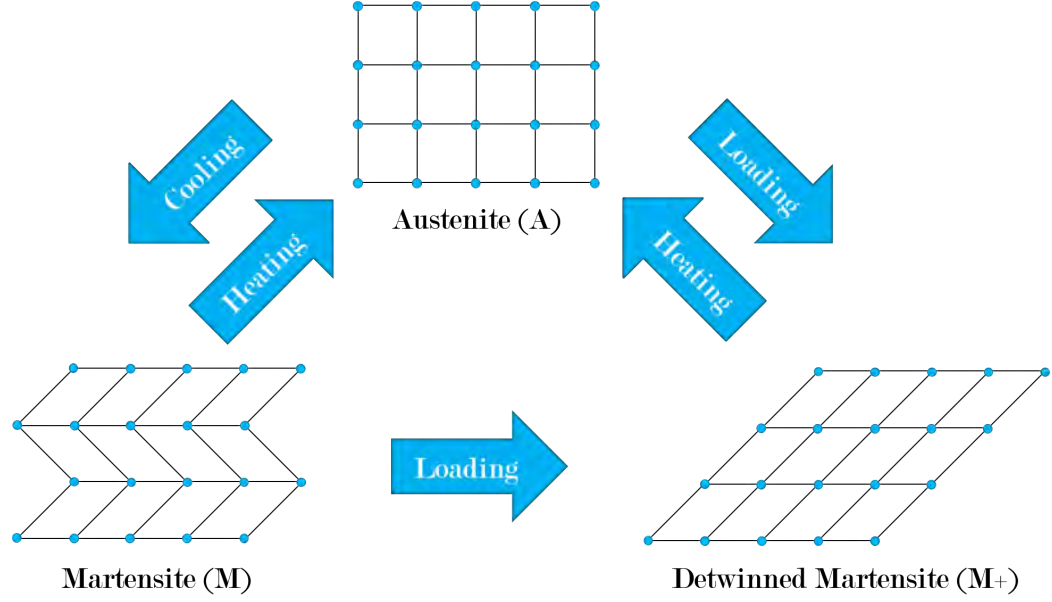


Figure 1.1: Phase transformation cycle of NiTi. The cycle begins in the low-temperature martensite phase, M, where the material can be loaded to form detwinned martensite, M+. By applying heat, the detwinned martensite can transform into austenite and recover the deformation caused via detwinning. Cooling the austenite returns the material to martensite again. Direct heating of the martensite can also cause the transformation to austenite. Finally, austenite can transform to detwinned martensite by inducing strain.

The martensite phase exists in two forms: a self-accommodating twinned form, M, and a detwinned phase, M+. Both have a monoclinic structure. The austenite phase, A, has a body-centered cubic structure [3, 30].

The process of transforming between the various structures of shape memory NiTi is dependent upon both the material's temperature and the loads applied to it. The twinned martensite phase occurs when the temperature of the NiTi is below the martensite finish temperature, M_f , and the stress is below the critical starting stress, σ_{cr}^s , Figure 1.2. From the self-accommodating martensite phase, the material begins to transform into the detwinned martensite phase by loading the material above σ_{cr}^s

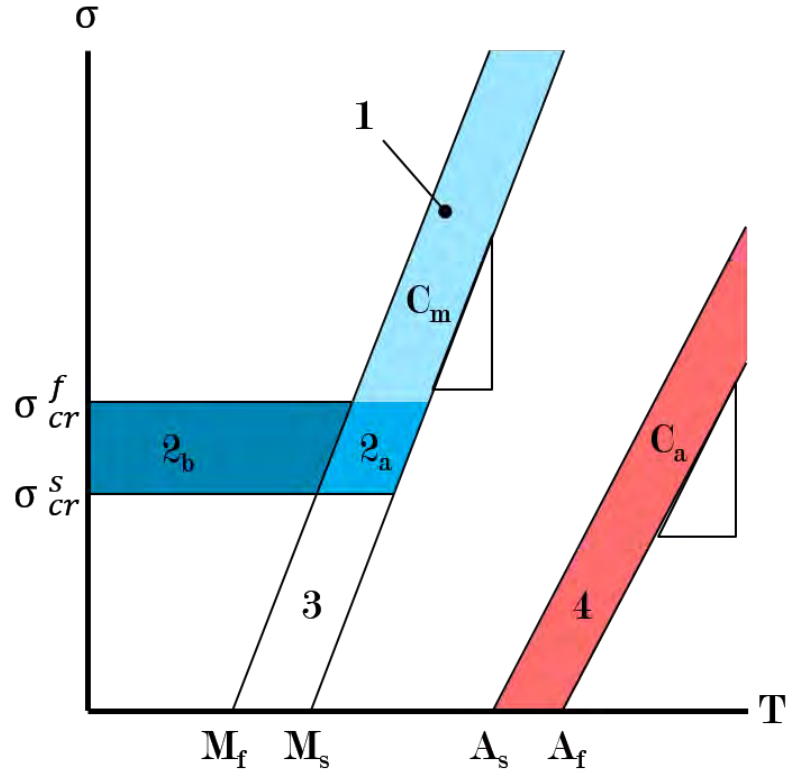


Figure 1.2: Example of phase diagram, stress (σ) versus temperature (T), for nickel-titanium. The temperature values of M_f , M_s , A_s , and A_f , represent the martensite finish, martensite start, austenite start, and austenite finish temperatures, respectively. The critical start and finish stresses are given as σ_{cr}^s and σ_{cr}^f respectively. C_M represents the martensite stress influence coefficient while C_A is the coefficient for austenite.

and completes the transformation when the load is increased to greater than or equal to the critical finishing stress, σ_{cr}^f .

To begin the transformation of NiTi into the austenite phase, the material (whether twinned or detwinned martensite) needs to be heated past the austenite start temperature, A_s . The transformation completes when the temperature increases past the austenite finish temperature, A_f . The process of transforming from the martensite

phase to the austenite phase is called “reverse transformation,” (M - A). Opposite of the reverse transformation is the “forward transformation,” (A - M), which is the transformation from austenite to martensite. The forward transformation begins when the austenite NiTi is cooled below M_s , and full transformation occurs when the temperature drops below M_f . Austenite can also transform directly to M+ by inducing stress within the material. All of these transformations are dependent upon stress since the critical temperature values depend upon the existing maintained stress within the material, Figure 1.2. The transition lines on the phase diagram are represented by:

$$M_f^\sigma = M_f + \frac{\sigma}{C_M} \quad (1.2)$$

$$M_s^\sigma = M_s + \frac{\sigma}{C_M} \quad (1.3)$$

$$A_s^\sigma = A_s + \frac{\sigma}{C_A} \quad (1.4)$$

$$A_f^\sigma = A_s + \frac{\sigma}{C_A} \quad (1.5)$$

where C_M and C_A are the stress influence coefficients for martensite and austenite respectively. The superscript σ represents the dependency on the material's stress.

In addition to being used as a shape memory material, NiTi can also act as a pseudoelastic material. This change in performance occurs when the NiTi material is in an environment whose ambient temperature is greater than A_f . Pseudoelastic NiTi, when unloaded from the M+ phase, does not remain in the M+ phase but will directly transform back to austenite. Both the shape memory and pseudoelastic NiTi material performance cycles still follow the stress-temperature phase diagram, but

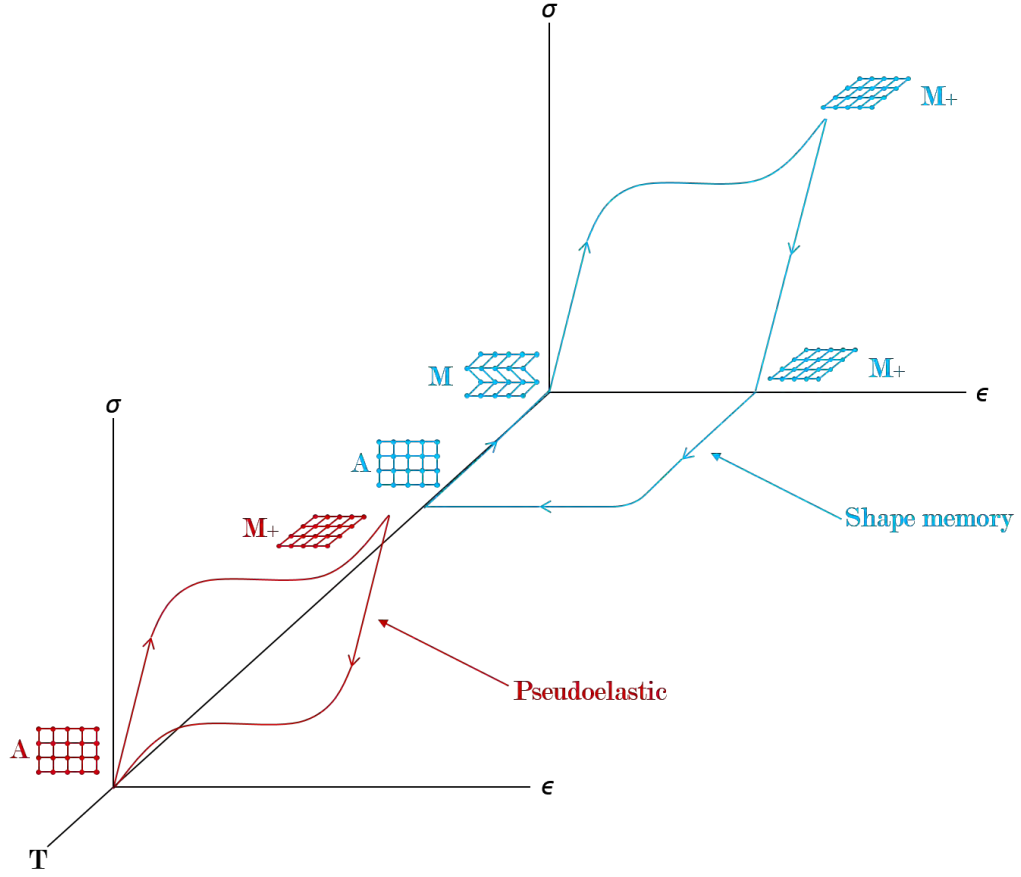


Figure 1.3: Stress vs. strain vs. temperature plot for transformation curves of shape memory and pseudoelastic NiTi.

each corresponding profile on a three-dimensional stress versus strain versus temperature plot is different, Figure 1.3, as the pseudoelastic NiTi does not require heating to recover the induced strain.

1.4 Metal Matrix Composite Fabrication Techniques

A variety of methods have been proposed over the years to produce composites containing NiTi fibers for either the purpose of adding strength to a part or controlling

expansion. These methods include casting [5, 15, 16], rolling [11], swaging [11], and ultrasonic additive manufacturing (also known as consolidation) [6, 7, 12, 13].

1.4.1 Casting

Casting of metals involves melting the material and pouring it into a mold to produce a desired shape. This process was implemented to produce Al-NiTi composite with 4% and 9% NiTi volume fraction [5]. Using a custom fiber holder, Figure 1.4, this study achieved cast material with no voids around the fibers, Figure 1.5. Even with this geometry achieved and the consolidation of the fibers, the method of casting involves a process that utilizes high-temperatures, making it difficult to embed the SMA in anything but its austenite phase unless an extremely large stress—one possibly too large for the fibers to withstand—is held on the fibers throughout the casting process.

1.4.2 Rolling and Swaging

Rolling and swaging are machining processes that force a material into an area smaller than its cross-section. The former process utilizes rollers to carry out the operation, while swaging uses a set of dies. Both processes can be performed cold or hot. Jin and Mavoorii [11] placed the NTE material between layers of the matrix material and then performed the rolling or swaging, Figures 1.6 and 1.7. In order to bond the materials to one another through these processes, the materials must be at high temperatures, which again creates issues with keeping the fibers in the desired phase.

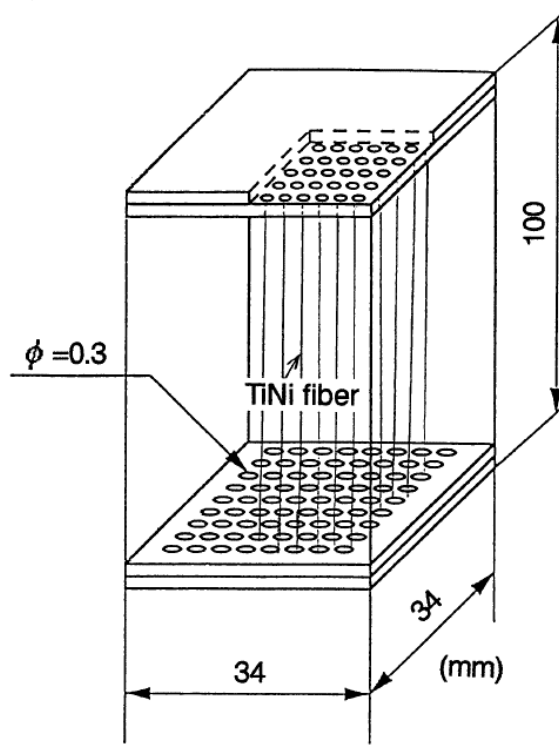


Figure 1.4: Mold used by Furuya et al. for aligning TiNi fiber during casting process to produce TiNi / Al composite [5].

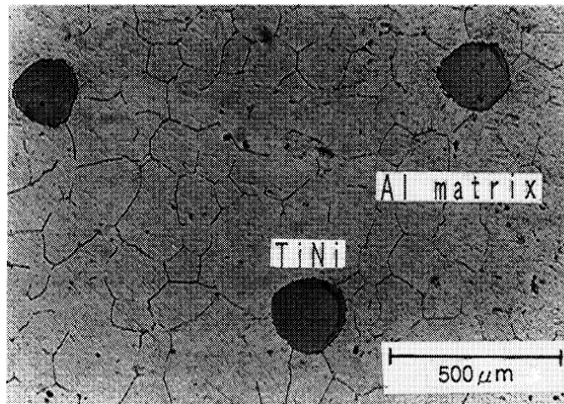


Figure 1.5: Micrograph of a typical cross section of the TiNi / Al-1100 composite produced by Furuya et al. [5].

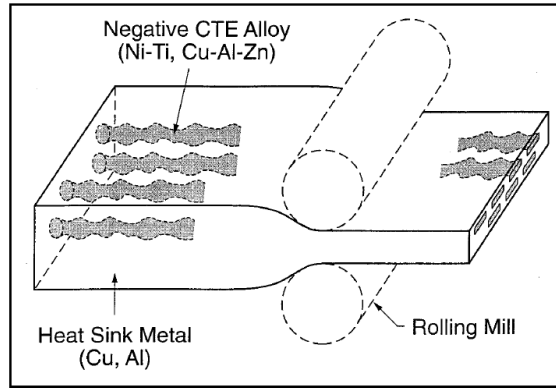


Figure 1.6: Production of composite with NTE fibers by rolling as proposed by Jin and Mavoori [11].

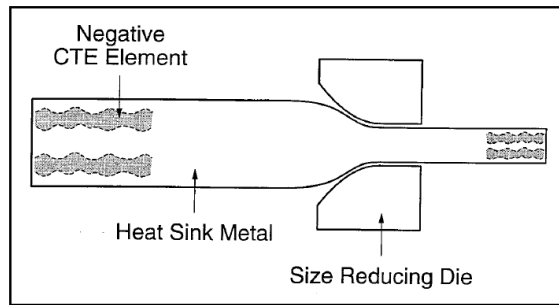


Figure 1.7: Production of composite with NTE fibers by swaging as proposed by Jin and Mavoori [11].

1.4.3 Ultrasonic Additive Manufacturing

Ultrasonic additive manufacturing (UAM) is a process that utilizes ultrasonic welding, a form of solid-state welding, in conjunction with subtractive computer numerical control (CNC) milling and laser machining operations to create metal parts. The process is different from the aforementioned manufacturing techniques in that the MMCs do not undergo the high temperatures associated with casting, rolling, swaging or other comparative welding operations that are fusion-based, requiring melting of the parent materials. This feature provides the unprecedented opportunity to embed thermally sensitive materials, such as SMAs, that would otherwise be destroyed through the use of other forms of welding and manufacturing [12, 13].

Ultrasonic welding is the foundation of the UAM process, as it is the ability to successively weld layers of metal foils, or tapes, that creates the bulk structures. The ultrasonic welding process occurs when ultrasonic vibrations, around 20 kHz, are applied by a sonotrode (horn) to a foil on top of another metal surface. The sonotrode is often roughened via electron discharge machining to create a surface typically around $R_a=7\text{ }\mu\text{m}$. The tape is held in place by a normal force, which can range in magnitude from 0.04 to 17800 Newtons [19]. The normal force brings surface asperities of the two materials into contact with one another, Figure 1.8. When the ultrasonic vibrations are applied via the sonotrode, surface oxides are broken down under a shear force, exposing nascent surfaces which bond due to grain growth across the clean metal-to-metal interface [20, 32].

Ultrasonic welding has extended into the UAM process by creating a translating anvil or table, a rotating sonotrode, a continuous tape feeding system, and subtractive processes, Figure 1.9. During production, the sonotrode revolves at the same speed as

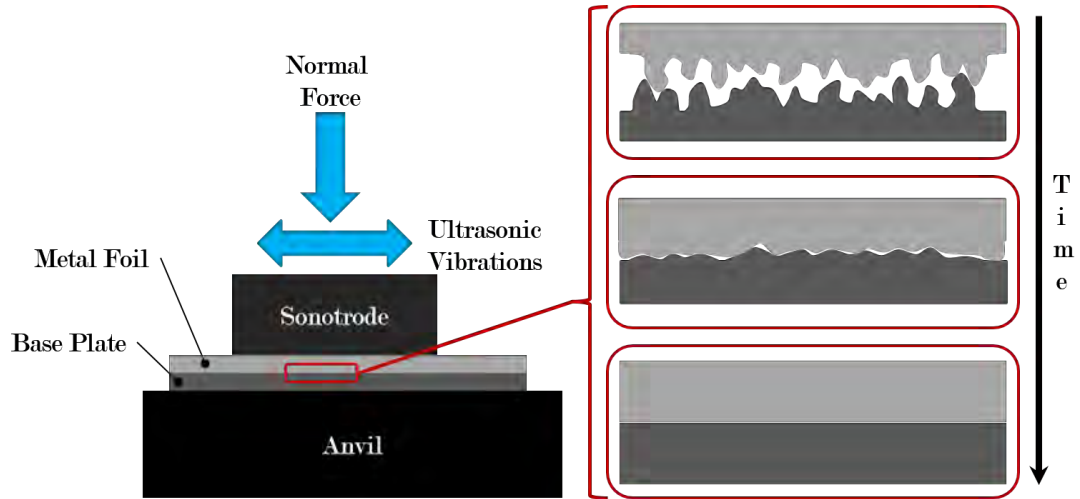


Figure 1.8: Time lapse of foil surfaces during ultrasonic welding process.

the table travels, such that a continuous linear weld is made between the tape and the base structure. The sonotrode, typically made of tool steel, oscillates perpendicular to the direction the table travels. Piezoelectric transducers produce the high frequency vibrations necessary for breaking down the surface oxides.

The UAM process is relatively new, patented in the early 2000s by Solidica, Inc. [31]. Early machines were modified welders that typically ran on power levels around 3 kW or less and had few parameters that could be controlled by the operator. Often, these parameters were limited to oscillation amplitude, contact force, and weld speed. Due to the low power levels of the machines, the materials that could be welded were restricted to softer aluminum alloys. A side effect of the low power systems were voids within the finished structures, Figure 1.10.

The latest UAM machines in development produce as much as 9 kW of power, making them capable of producing parts composed of aerospace grade materials and dissimilar materials without voids, Figure 1.11. The single transducer design has

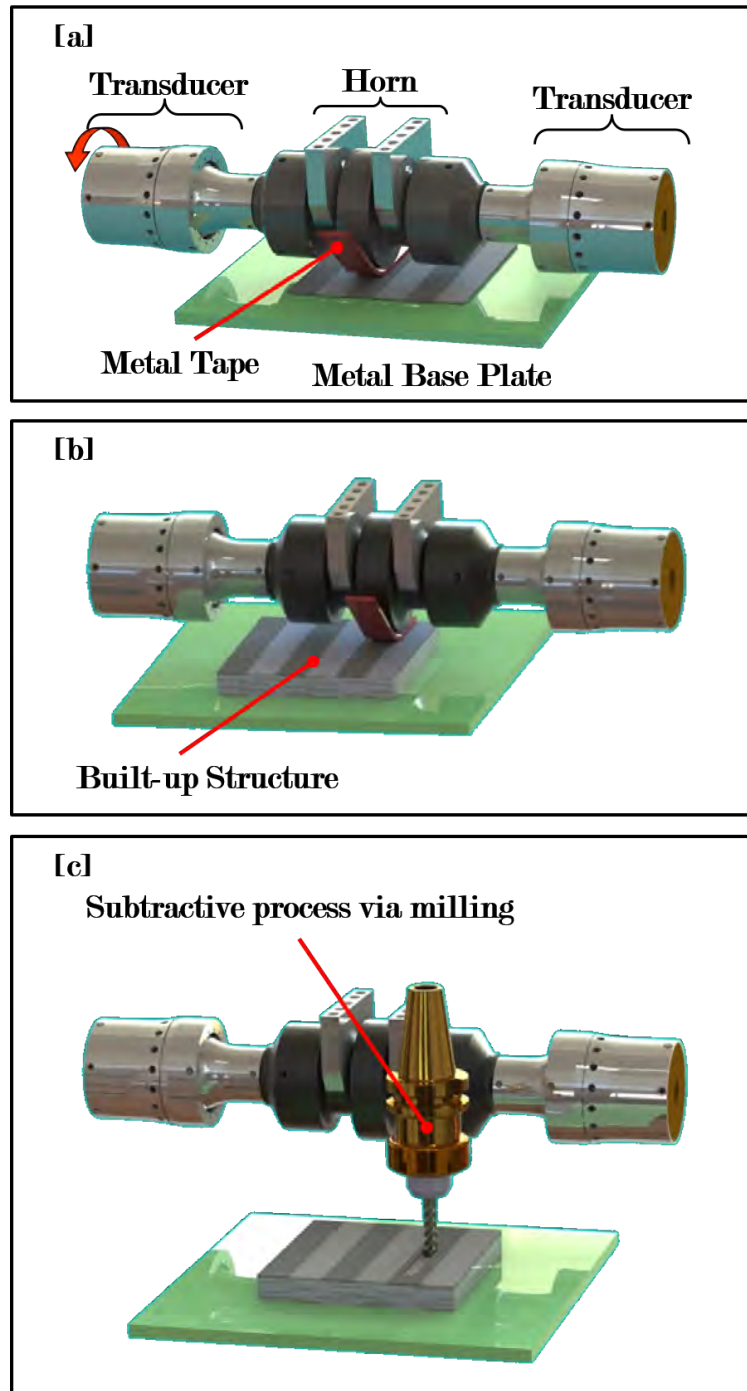


Figure 1.9: Ultrasonic additive manufacturing process. [a] Ultrasonic welding system welds metal tapes to base plate; [b] successive welding of tapes over multiple layers builds solid part; [c] periodic subtractive machining shapes and maintains uniform welding surface. Illustrations courtesy of Fabrisonic, LLC.



Figure 1.10: Cross-section of part made on 1 kW power UAM machine.

also been upgraded to twin transducers, which are mounted on opposite sides of the sonotrode. Electronic controllers ensure these pairs oscillate in phase. In addition to the transducer upgrades, the user-defined parameters available have broadened to include:

- Weld amplitude
- Weld speed
- Contact force
- Spot amplitude
- Spot duration
- Tape tension

Figure 1.12 shows a 9 kW system housed at The Ohio State University. By installing the welders into CNC machines, the subtractive processes are easily carried out, allowing for internal features to be incorporated into part geometries.

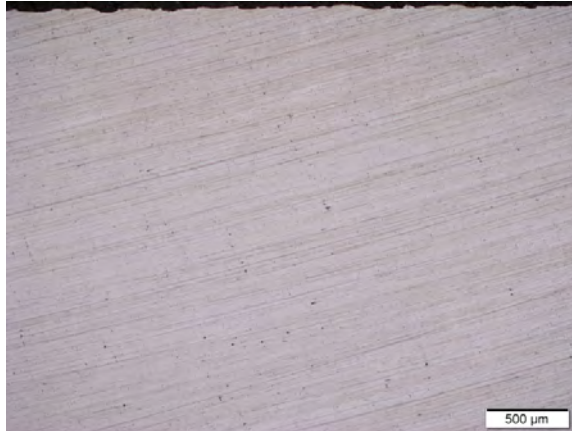


Figure 1.11: Cross-section of part made on 9 kW power UAM machine.



Figure 1.12: Ultrasonic additive manufacturing system housed at The Ohio State University's UAM Center. This system produces 9 kW of ultrasonic power.

CHAPTER 2

DESIGN OF COMPOSITES VIA SHAPE MEMORY ALLOY AND SHAPE MEMORY ALLOY COMPOSITE MODELS

Design of the composites within this thesis was conducted through the use of a numerical model developed by Hahnlen [6]. The Hahnlen composite model is based on an SMA composite model developed by Sittner [18]. Hahnlen utilizes a bivariant constitutive SMA model, altered from an earlier model developed by Brinson [3]. By use of these models, the composites developed for this study were designed to contain a specific volume fraction of NiTi fibers to achieve the goal of a near-zero CTE composite over a designated temperature range. This chapter will provide detail on both the new bivariant constitutive SMA model and the Hahnlen composite model. A discussion of how these models combine to assist in the design of the aluminum nickel-titanium will follow.

2.1 SMA Bivariant Constitutive Model

2.1.1 Brinson Model

The SMA bivariant model used for the NiTi fibers within this study was developed by Hahnlen [6]. The model is based on an earlier model produced by Brinson [3], which

combined the works of Tanaka [22, 24, 23] and Liang and Rogers [14]. The result of Brinson's model:

$$\sigma - \sigma_o = E(\epsilon - \epsilon_o) + \Omega(\xi_s - \xi_{so}) + \Theta(T - T_o), \quad (2.1)$$

is a constitutive relationship between the SMA's stress to its strain, martensitic volume fraction, and temperature which are represented by ϵ , ξ , and T , respectively. In addition, $E(\xi)$ is the elastic modulus, $\Omega(\xi)$ is the transformation tensor, and Θ is related to the coefficient of thermal expansion. Brinson enhanced the original model by separating the martensitic volume fraction into a stress-induced component (ξ_s) and a temperature-induced component (ξ_T):

$$\xi = \xi_s + \xi_T. \quad (2.2)$$

By changing the martensitic volume fraction to include these components, the phase diagram based on Liang and Rogers' empirical based cosine model also changed, Figure 2.1

The difference between the Liang and Rogers phase diagram and Brinson's is the inclusion of the transformation to martensite or detwinned martensite. Because Liang and Rogers did not stipulate the difference between the two forms, their model only requires one transformation region, whereas Brinson has four different regions: 1, 2_a, 2_b, and 3.

The value in the Brinson model is its ability to model not only the pseudoelastic effect but the shape memory effect within the nickel-titanium. In addition, the Brinson model only requires basic material values that can be determined through isothermal tensile tests and differential scanning calorimetry.

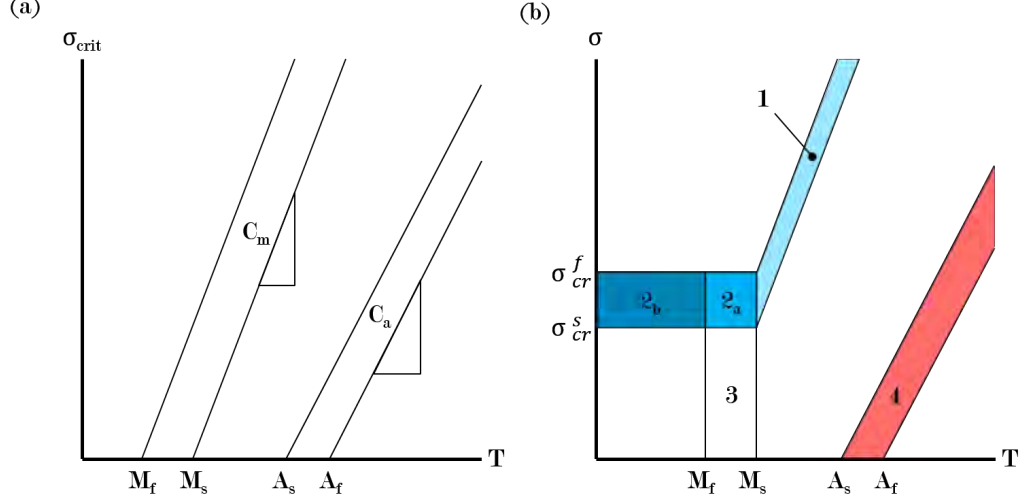


Figure 2.1: Phase diagrams of NiTi according to (a) Liang and Rogers model [14] and (b) Brinson's bivariant model [3].

2.1.2 Hahnlen Model

Hahnlen's bivariant model altered the work of Brinson by changing the dependent variable within the model from stress to strain. This change was made by first evaluating

$$(\sigma - \sigma_o) = E(\epsilon - \epsilon_o) + \Theta(T - T_o) + \Omega_T(\xi_T - \xi_{To}) + \Omega_s(\xi_s - \xi_{so}) \quad (2.3)$$

for various starting and ending states. The value of Ω_s was determined by considering maximum recovery of strain from an initial austenite phase. This situation yields the conditions of: $\sigma_o = 0, \epsilon_o = 0, T_o = T, \xi_{To} = 0, \xi_{so} = 0, \sigma = 0, \epsilon = \epsilon_L, \xi_T = 0$, and $\xi_s = 1$. Applying these conditions (2.3) gives:

$$\begin{aligned}
0 &= E(\epsilon_L) + \Theta(0) + \Omega_T(0) + \Omega_s(1) \\
&\implies \Omega_s = -E\epsilon_L.
\end{aligned} \tag{2.4}$$

In order to model the transition from fully martensite to having the maximum amount of recoverable strain requires the application of $\sigma_o = 0, \epsilon_o = 0, T_o = T, \xi_{To} = 1, \xi_{so} = 0, \sigma = 0, \epsilon = \epsilon_L, \xi_T = 0$, and $\xi_s = 1$ to (2.3). The result is:

$$\begin{aligned}
0 &= E(\epsilon_L) + \Theta(0) + \Omega_T(0 - 1) + \Omega_s(1) \\
&\implies \Omega_s - \Omega_T = -E\epsilon_L \\
&\implies \Omega_T = 0.
\end{aligned} \tag{2.5}$$

The final condition applied was free expansion based on thermal variance without any transformation taking place where: $\sigma_o = 0, \epsilon_o = 0, \sigma = 0, \xi_s = \xi_{so}$, and $\epsilon = \alpha(T - T_o)$.

These parameters yield:

$$\begin{aligned}
(0) &= E(\alpha(T - T_o)) + \Theta(T - T_o) + \Omega_s(0) \\
&\implies -E\alpha = \Theta
\end{aligned} \tag{2.6}$$

Applying the results of (2.4), (2.5), and (2.6) to (2.3) the model takes the form of

$$\begin{aligned}
(\sigma - \sigma_o) &= E(\epsilon - \epsilon_o) - E\alpha(T - T_o) - E\epsilon_L(\xi_s - \xi_{so}) \\
\frac{1}{E}(\sigma - \sigma_o) &= (\epsilon - \epsilon_o) - \alpha(T - T_o) - \epsilon_L(\xi_s - \xi_{so}) \\
\implies (\epsilon - \epsilon_o) &= \frac{1}{E}(\sigma - \sigma_o) + \alpha(T - T_o) + \epsilon_L(\xi_s - \xi_{so}),
\end{aligned} \tag{2.7}$$

where the last line is the constitutive strain equation used in the Hahnlen model.

In addition to changing the dependent variable, Hahnlen included the dependence on stress for the martensitic transformation temperatures below the critical starting

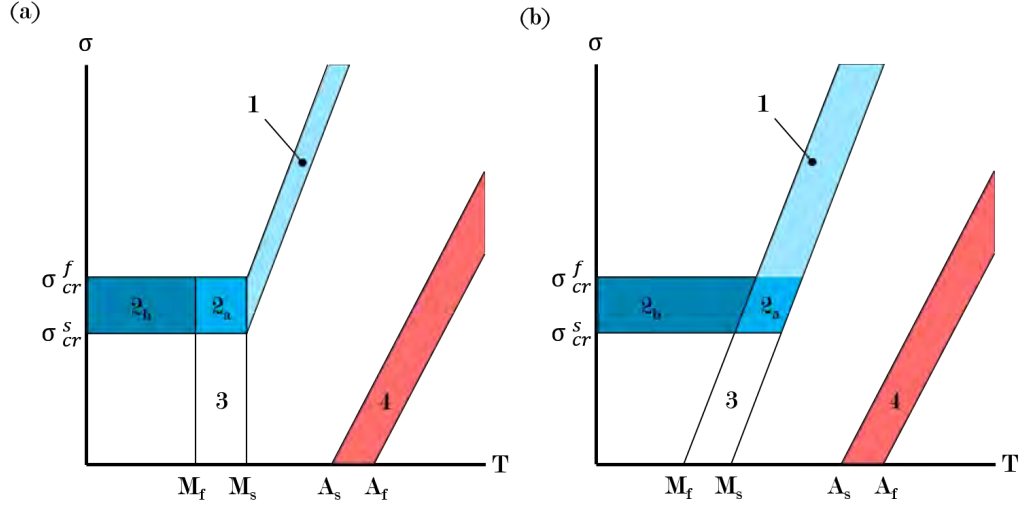


Figure 2.2: Phase diagrams of NiTi according to (a) Brinson's bivariant model [3] and (b) Hahnlen's new bivariant model [6].

stress. Therefore, the martensitic transformation temperatures vary from the zero stress temperature upwards according to a linear trend with a slope of C_M . The result is again a new phase diagram, Figure 2.2, with slightly different profiles to some of the transformation regions. The martensitic transformations occur over regions 1, 2_a , 2_b , and 3, and the austenite transformation over region 4.

2.2 SMA Composite Model

Modeling of the metal matrix composites within this work is based on a model produced by Hahnlen [6], who integrated the aforementioned Hahnlen SMA model into a phenomenological SMA composite model developed by Sittner [18]. The original model was designed for use with SMA-epoxy models, but was adopted as a basis for the MMC model due to its success in modeling the SMA-epoxy composites and use of time derivatives to simplify the transformation conditions. In addition, Hahnlen

used the concept of strain-matching. Strain-matching utilizes the idea that the strain of the composite is equivalent to the strain of the matrix which is in turn equivalent to the strain of the fibers, as shown by:

$$\epsilon_c = \epsilon_m = \epsilon_f \quad (2.8)$$

where ϵ_c , ϵ_m , and ϵ_f are the strains for the composite, matrix, and fibers, respectively. The concept of strain-matching assumes that the continuous fibers are fully constrained within the matrix along the direction of interest.

If the fibers are fully constrained, the composite can perform according to two different situations that depend on the state in which the NiTi fibers are embedded, Figure 2.3. In the first situation, the fibers are embedded in the twinned, or self-accommodating, martensite phase; in the second situation, the fibers are embedded in the detwinned martensite phase. According to the former condition, the NiTi fibers will not demonstrate any recovery upon heating above A_f , and the composite will not have an altered CTE other than what is produced by the difference in CTE between the matrix and fibers as given in the rule-of-mixtures. However, in the second situation, the fibers are prestrained through the application of a preload before being embedded in the matrix, which results in detwinned martensite. When the composite is heated above A_s , the NiTi fibers try to recover the prestrain. This attempt to recover the prestrain is blocked by the expansion of the Al matrix. By balancing the recovery forces of the NiTi fibers with the forces associated with the Al matrix's expansion a composite that has a low to near-zero CTE is possible.

Therefore, with the assumption of the fibers being fully constrained within the matrix and substituting the matrix strain equation,

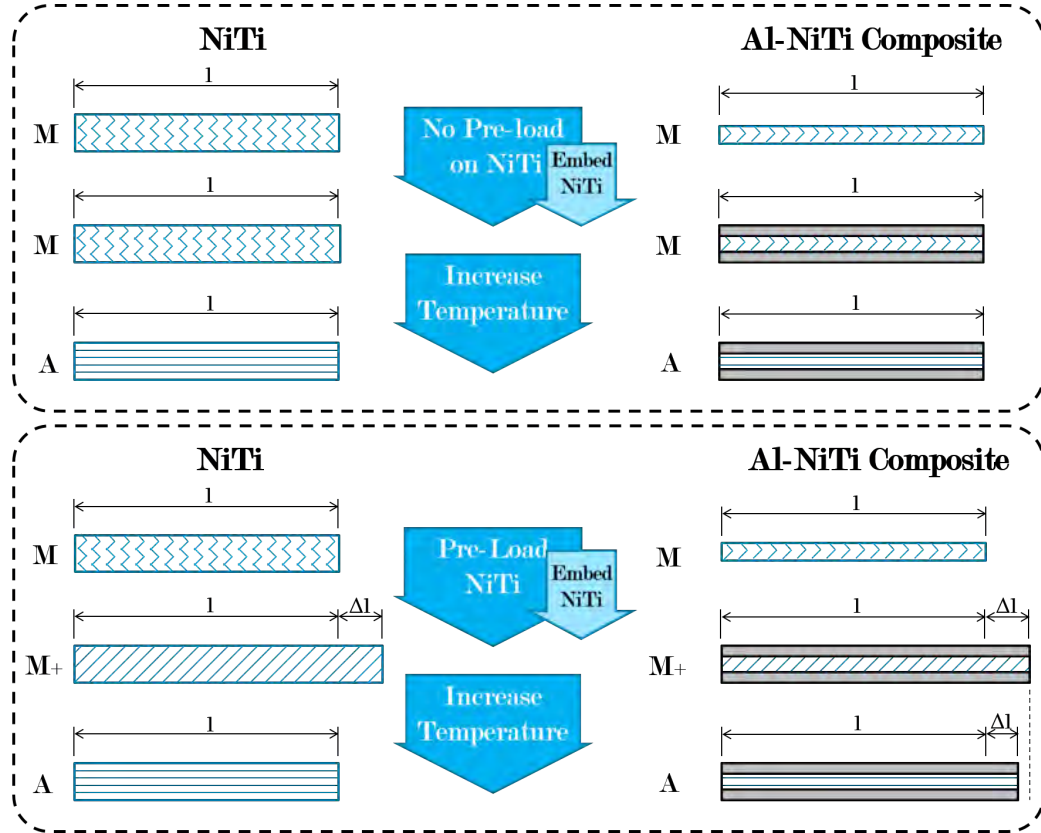


Figure 2.3: Diagram of composite theory based on (top) no initial preload of NiTi fibers before being embedded and (bottom) prestrain applied to NiTi before being embedded.

$$\epsilon_m = \frac{1}{E_m}(\sigma_m - \sigma_{mo}) + \alpha_m(T - T_o), \quad (2.9)$$

and (2.7) for ϵ_f in (2.8), the strain matching equation becomes:

$$\begin{aligned} \epsilon_c = \epsilon_m = \frac{1}{E_m}(\sigma_m - \sigma_{mo}) + \alpha(T - T_o) = \\ \frac{1}{E_f}(\sigma_f - \sigma_{fo}) + \alpha_f(T - T_o) + \epsilon_L(\xi_s - \xi_{so}) = \epsilon_f. \end{aligned} \quad (2.10)$$

Hahnlen goes on to apply the assumptions of no external loads, zero initial stresses, and that the composite is a long-fiber reinforced composite where the length of the fibers is equal to the length of the matrix. Based on these assumptions, (2.10) can be written in terms of the fiber stress (σ_f) and the SMA volume fraction (ν) to become:

$$\frac{1}{E_m} \left(\frac{-\nu}{(1-\nu)} \sigma_f \right) + \alpha(T - T_o) = \frac{1}{E_f}(\sigma_f - \sigma_{fo}) + \alpha_f(T - T_o) + \epsilon_L(\xi_s - \xi_{so}). \quad (2.11)$$

Solving σ_f :

$$\sigma_f = \frac{(\alpha_m - \alpha_f)\Delta T}{\frac{1}{E_f} + \frac{\nu}{E_m(1-\nu)}} - \frac{\epsilon_L(\xi_s - \xi_{so})}{\frac{1}{E_f} + \frac{\nu}{E_m(1-\nu)}}. \quad (2.12)$$

The model is finalized when (2.12) is substituted into (2.7):

$$\epsilon_c = \epsilon_f = \frac{1}{E_f} \left[\frac{(\alpha_m - \alpha_f)\Delta T}{\frac{1}{E_f} + \frac{\nu}{E_m(1-\nu)}} - \frac{\epsilon_L(\xi_s - \xi_{so})}{\frac{1}{E_f} + \frac{\nu}{E_m(1-\nu)}} \right] + \alpha_f\Delta T + \epsilon_L(\xi_s - \xi_{so}) \quad (2.13)$$

and simplified to the form:

$$\epsilon_c = \frac{E_f\nu\alpha_f + E_m(1-\nu)\alpha_m}{E_f\nu + E_m(1-\nu)}\Delta T + \frac{E_f\nu\epsilon_L(\xi_s - \xi_{so})}{E_f\nu + E_m(1-\nu)}. \quad (2.14)$$

The final form of the SMA composite model has two terms: the thermoelastic term (first term) that always exists and the term corresponding to transformation of the NiTi fibers within the composite (second term).

2.3 Composite Model Implementation for Composite Design

Three methods for implementing the Hahnlen SMA model exist: an incremental approach, an interpolation approach, and a simultaneous approach. Within this work, the interpolation method is used for composite design. The interpolation method was chosen for its ability to accommodate fibers with $\xi_{so} > 0$, its quick cycle time, and its ease of use (whereas the incremental method has instabilities for $\xi_{so} > 0.01$ and the simultaneous method is time intensive). The modeling of two Al-NiTi composites was performed for this study. The first composite modeled contained shape memory material while the second had pseudoelastic material.

2.3.1 Design of Al-NiTi Composites

The development of a low-CTE, Al-NiTi composite made with shape memory NiTi fibers first required the acquisition of material parameters to feed into the composite model. These parameters were obtained through a characterization process, Appendix A, that involved both differential scanning calorimetry (DSC) and isothermal tensile testing. The results of the characterization process for the shape memory material, Table 2.1, were used both in the model but also to create a stress-temperature phase diagram, Figure A.9, for the material. Using MATLAB, the composite model simulated the performance of an Al-NiTi composite with volume fractions of NiTi material varying by 0.2% from 7.0% to 9.0% over the temperature range of 23.8°C to 150.0°C, Figure 2.4.

Table 2.1: Material parameters for shape memory NiTi fibers used in NiTi-Al composites.

Material Parameter	Value
Martensite start temperature, M_s	39°C
Martensite finish temperature, M_f	40°C
Austenite start temperature, A_s	53°C
Austenite finish temperature, A_f	68°C
Martensite stress influence coefficient, C_M	14.48 MPa/°C
Austenite stress influence coefficient, C_A	19.16 MPa/°C
Maximum strain recovery, ϵ_L	6.3%
Elastic modulus of martensite, E_M	29.8 GPa
Elastic modulus of austenite, E_A	61.2 GPa

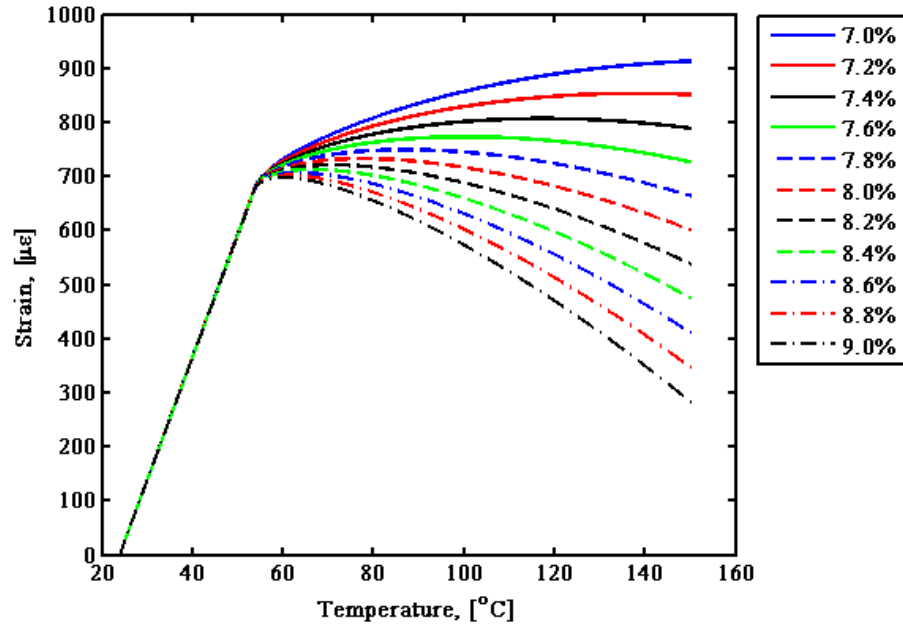


Figure 2.4: Composite performance model results for Al-NiTi composite manufactured with 7.0% to 9.0% shape memory NiTi fibers.

Table 2.2: Material parameters for pseudoelastic NiTi fibers used in NiTi-Al composites.

Material Parameter	Value
Martensite start temperature, M_s	-86°C
Martensite finish temperature, M_f	-90°C
Austenite start temperature, A_s	15°C
Austenite finish temperature, A_f	16°C
Martensite stress influence coefficient, C_M	3.21 MPa/°C
Austenite stress influence coefficient, C_A	7.56 MPa/°C
Maximum strain recovery, ϵ_L	6.0%
Elastic modulus of martensite, E_M	21.4 GPa
Elastic modulus of austenite, E_A	50.4 GPa

The results of the composite model show that for the given shape memory material, 7.6% NiTi volume fraction is needed to achieve the desired CTE of $0.00 \mu\epsilon/^\circ\text{C}$ over the given temperature range. This was determined by use of linear regression on the various model results over the temperature range of 55.0°C to 150.0°C. Because it is just above the austenite start temperature, 55.0°C was chosen as the starting temperature for the regression analysis.

The characterization process was repeated for the pseudoelastic NiTi material to determine the parameters, Table 2.2, for running the composite model. The pseudoelastic NiTi ribbons were embedded within the composite in a strained state to produce the detwinned martensite phase. By starting in the detwinned state, the composite would display low-CTE results immediately rather than needing to wait until the austenite start temperature was reached. As with the shape memory composite, the model was run for a range of volume fractions, 15.6% to 17.6%, with increments of 0.2%, Figure 2.5. The results show a volume fraction of 16.2% NiTi material provides a CTE of $0.00 \mu\epsilon/^\circ\text{C}$.

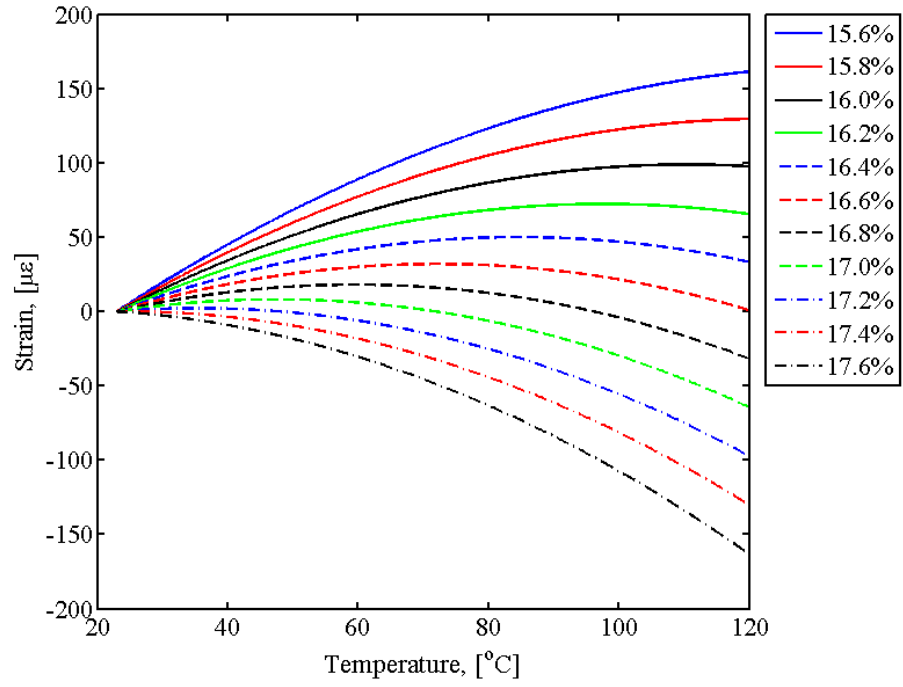


Figure 2.5: Composite performance model results for Al-NiTi composite manufactured with 15.6% to 17.6% pseudoelastic NiTi fibers.

Once the necessary volume fractions were calculated using the composite model, the cross-sectional geometry of each Al-NiTi composite was designed based on the desired cross-sectional area of the composite. First, using the desired cross-section area of the composite (A_{comp}) the number of NiTi fibers (n_f) could be solved for using:

$$A_{comp} = wt, \quad (2.15)$$

$$A_{NiTi} = A_{comp}\nu, \quad (2.16)$$

and

$$n_f = A_{NiTi}/A_f, \quad (2.17)$$

where w, t, A_{NiTi} , and A_f are the composite width, composite thickness, total NiTi cross-sectional area, and the NiTi fiber cross-sectional area, respectively. By knowing the necessary number of fibers, the placement of the fibers within the cross-section could be determined.

The goal for the fiber layout was to spread the fibers throughout the cross-section while maintaining both a horizontal axis of symmetry and a vertical axis of symmetry. By spreading out the fibers, the expansion of the aluminum matrix would be counteracted throughout the composite rather than just in one region, Figure 2.6. The axes of symmetry ensure that when blocking forces are present in the composite, they do not produce a bending moment. If such a moment occurred, the composite would deflect in the direction of the greater internal stresses, (the side of the line of symmetry with the greater number of fibers), Figure 2.7. Therefore, the final cross-sections

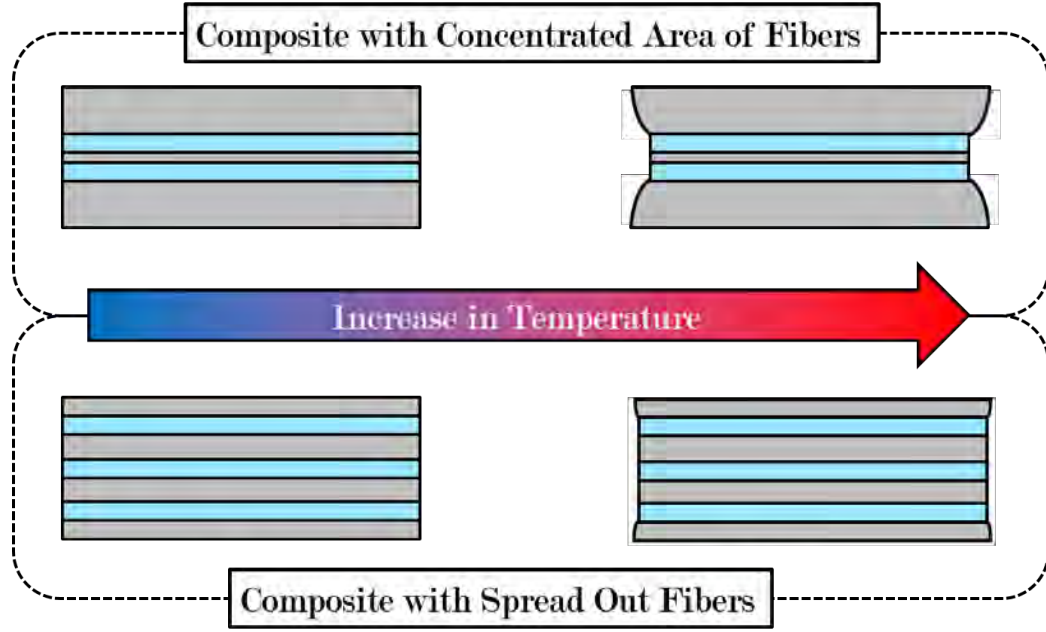


Figure 2.6: Cross-sections (as viewed from side) and effects of ribbon concentration on composite expansion.

for the composites in this study were designed to stagger the ribbons from one layer to the next, Figure 2.8, to achieve the desired geometry. The distances between the ribbons within each layer and the distance between layers are parameters that can change with each new composite; however, equispacing between the ribbons within each layer is desired and typically applied to the final geometry in an effort to keep the ribbons from becoming too concentrated.

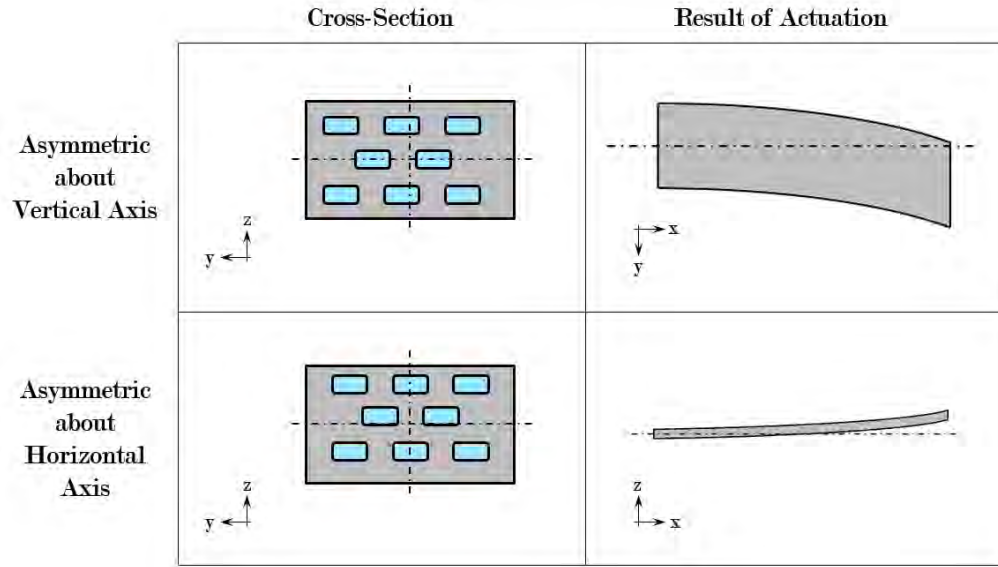


Figure 2.7: Cross-sections and effects of asymmetric fiber placement on composite expansion, where the dashed-dot lines represent an axis of symmetry.

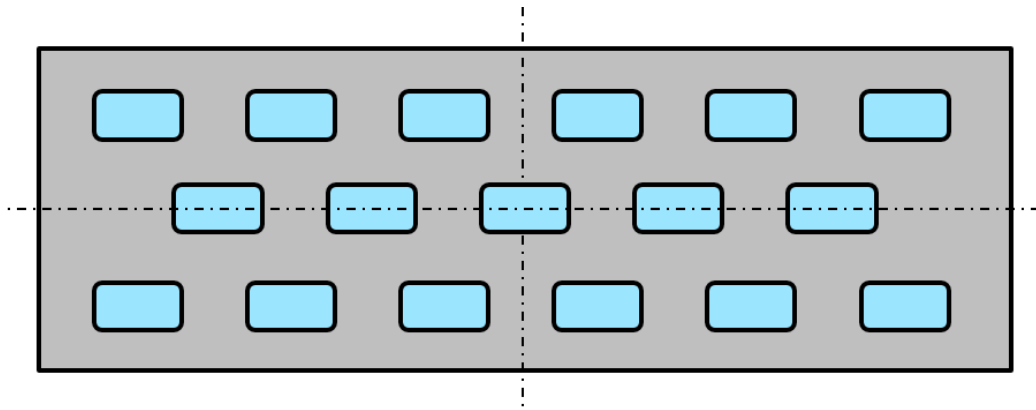


Figure 2.8: Example of cross-section style deployed in the Al-NiTi composites within this study.

CHAPTER 3

FABRICATION OF MULTI-LAYER AL-NITI COMPOSITES

Two styles of multi-layer composites were produced for this study. The first were smaller, coupon-style samples measuring between 7.62 cm to 9.53 cm (3.00" to 3.75") in length, less than 1.27 cm (0.50") in width, and under 0.25 cm (0.10") in height. These were made with both shape memory and pseudoelastic nickel-titanium fibers. This style was fabricated to study if actuation of the fibers and a reduction of CTE across multiple layers are possible as well as thermal and electrical properties. The other style of composites manufactured were pieces designed to be both longer and taller than the coupon samples. The purpose of these pieces was to develop a method for producing composites with larger geometries that could be machined to desired forms.

3.1 Material Detwinning

3.1.1 Pseudoelastic Nickel-Titanium

Pseudoelastic nickel-titanium ribbons were one type of fiber used in the making of composites within this study because of the opportunity they provided to generate the necessary blocking stresses within the composite at lower temperatures than

shape memory NiTi material. The lower austenite start and finish temperatures of the pseudoelastic material make this possible. Because the pseudoelastic NiTi ribbons are in the austenite phase at room temperature—the temperature at which the consolidation occurs—a straining process was developed to ensure the material was detwinned martensite before being embedded into the aluminum.

To detwin the ribbons for a layer in a composite, the ribbons were cut to lengths roughly 15.24 cm (6.00”) longer than the length of the composite to be produced. The additional length was to aid in the detwinning of the fibers and ensure the detwinned section of the ribbons was long enough for the composite. They were then arranged parallel to one another with the spacing required to meet the dimensions of the composite. Feeler gages were used to help provide the appropriate spacing between one ribbon and those next to it. Once the ribbons were in position, tape was used on the ends to create a ribbon pack, Figure 3.1, that helped maintain the geometry throughout the detwinning process. The ribbon pack was then clamped on each end, using custom detwinning clamps developed by Hahnlen, Figure 3.2 [6]. These clamps allowed for the ribbon pack to be suspended vertically. In this position, dead weights were added manually to apply the necessary force to detwin the ribbons.

With the ribbons detwinned, a custom-designed and machined transfer clamp assembly, Figure 3.3, was used to hold the ribbons in the detwinned martensite phase. The transfer assembly was machined from steel to ensure the stress from the strained ribbons did not cause significant deflection of the clamp, as any deflection in the assembly would mean a decrease in the strain of the ribbons and the possibility of the ribbons transforming back into the austenite phase. Two transfer assemblies were manufactured: one for the coupon size samples, with all parts made completely

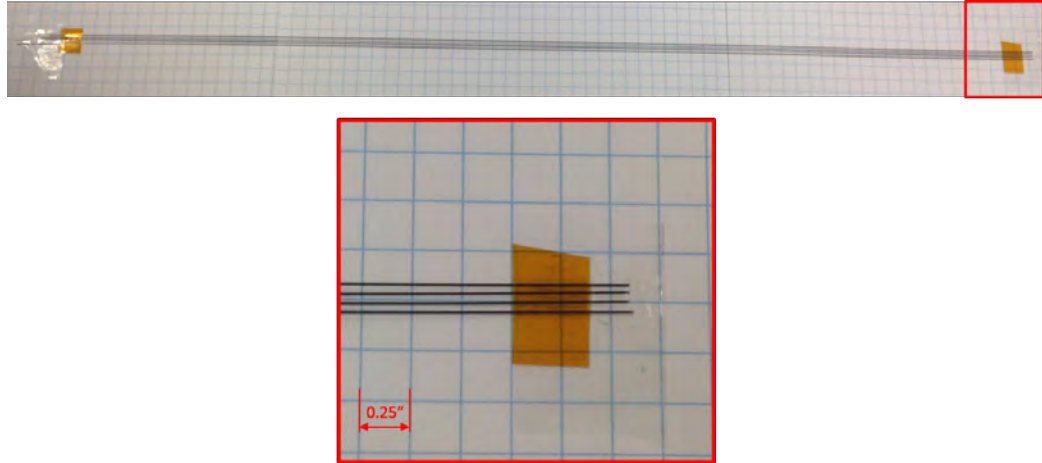


Figure 3.1: Ribbon pack used for collecting and arranging the NiTi ribbons to be embedded into the aluminum matrix.

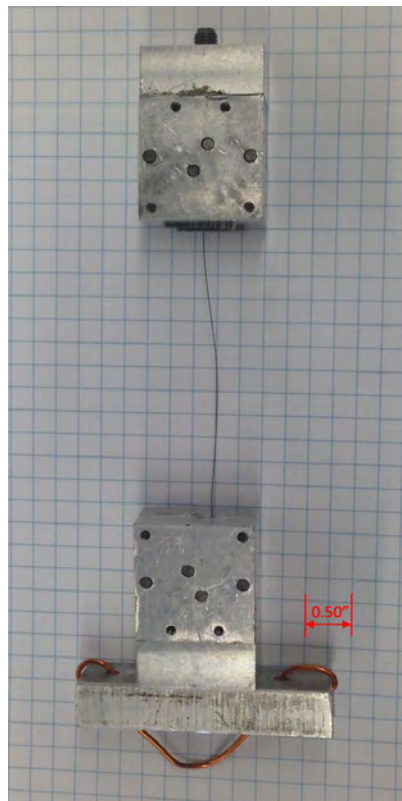


Figure 3.2: Clamps used for detwinning packs of pseudoelastic NiTi ribbons. The upper clamp was threaded into a cantilever fixture while weights were suspended from the lower clamp.

from low-carbon steel, and a longer one for the larger geometry composites, produced from multiple types of steel. The transfer clamp assemblies consisted of three main components: the backbone, the upper portions of the ribbon clamps, and the lower portions of the ribbon clamps, Figures 3.4 and 3.5. The backbone and lower ribbon clamp pieces were produced from low-carbon steel in both assemblies, while the upper ribbon clamps were AR-500 steel and low-carbon steel for the larger and smaller assemblies, respectively. The shape of the ribbon clamps for the larger assembly were altered to a C-shaped piece. The changes to the clamps were made to better resist the stresses induced by the ribbons when clamped to the base plate and to stop the abrading of the clamp's surface by the NiTi ribbons. Using the transfer assembly, the ribbons were kept in their current detwinned state as they were removed from the detwinning clamps and moved to a custom base plate, Figure 3.6. The base plate, also made from low-carbon steel, was designed to fit the vacuum chuck system within the Ohio State UAM machine. The base plate also held the sacrificial build plate in place using multiple 8-32, counter-sunk screws, while allowing for the detwinned ribbons to be clamped in place using the pockets milled into the plate. Once on the base plate, the ribbon clamps were bolted to the base plate and detached from the backbone of the assembly. This left the ribbons clamped in the proper phase and location.

3.1.2 Shape Memory Nickel-Titanium

The other material used in this study was shape memory NiTi, which was also in the form of ribbons. Shape memory material was considered in addition to the pseudoelastic material for its ability to be embedded within the aluminum without

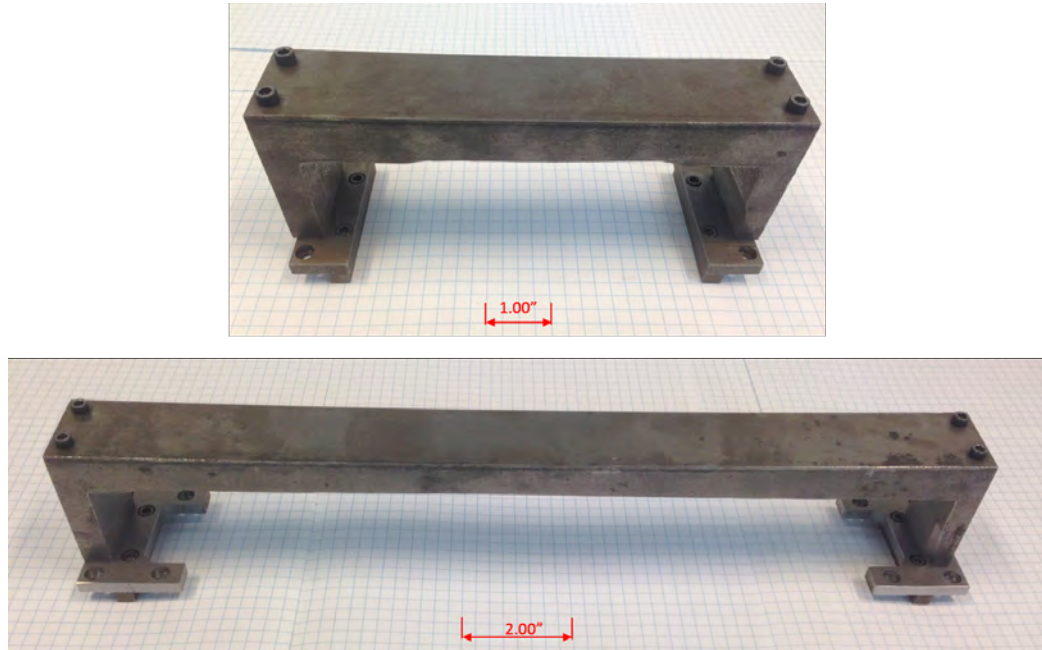


Figure 3.3: Assemblies used in transferring ribbons (either detwinned or twinned) from one location to another without the geometry being affected or strain recovered in the process.

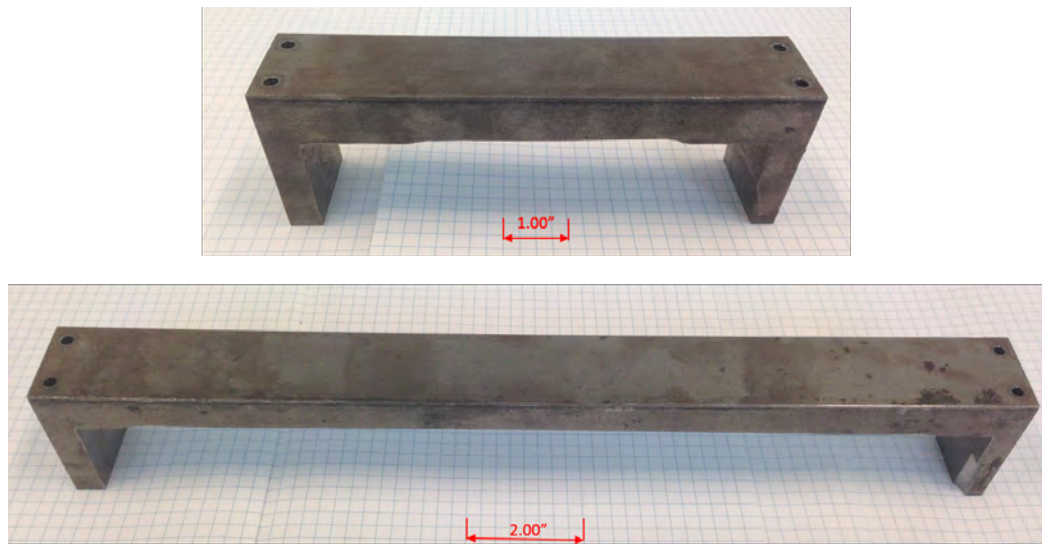


Figure 3.4: Backbones of coupon style (upper) and large geometry style (lower) transfer assemblies.

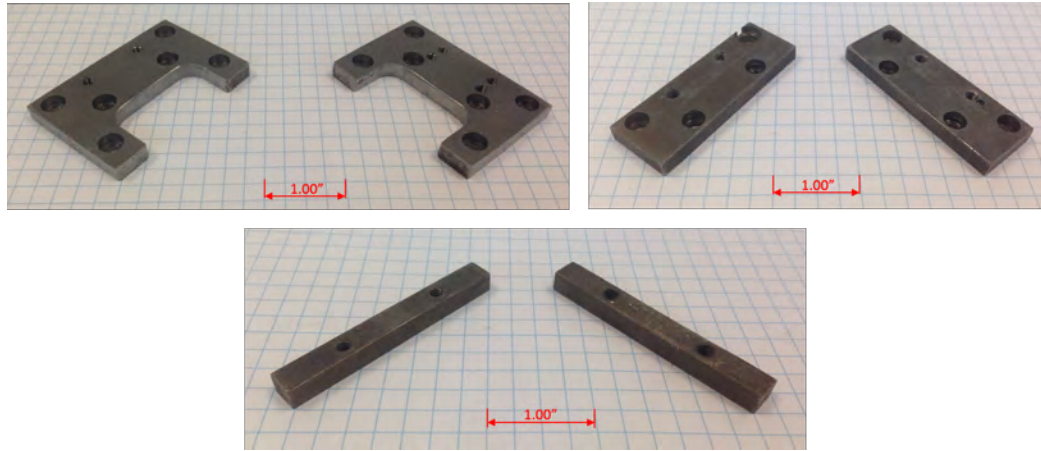


Figure 3.5: Ribbon clamps used as part of the transfer assemblies to maintain geometry and prestrain on the base plate. (Top left) Upper ribbon clamp for coupon size samples, (Top right) upper ribbon clamp for large geometry samples, and (Bottom) lower ribbon clamp.

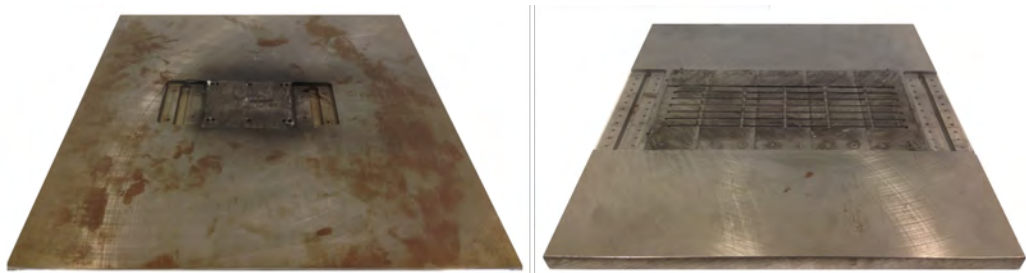


Figure 3.6: Base plates used for the production of coupon-size (left) and large geometry (right) Al-NiTi composites.

having to be constrained in a stressed state for detwinned martensite to be present. Because of the shape memory material's ability to remain in the detwinned martensite phase at room temperature, the process for preparing the ribbons for consolidation was different than that of the pseudoelastic material.

Detwinning of the shape memory material was again performed on ribbons that were roughly 15.24 cm (6.00") longer than the composite to be fabricated. This additional length allowed the ribbons to be held for both the detwinning and the embedding process. The detwinning process for the shape memory material was carried out one ribbon at a time using a 2224 N (500 lbf) capacity table top load frame, Figure 3.7. The load frame was used for the shape memory material because of the relatively low volume fraction of NiTi material needed in the composite as compared to that of the pseudoelastic material. Additionally, the material would not transform out of detwinned martensite upon unloading. Following the detwinning, ribbon packs were again made to help control the geometry of the ribbons throughout the rest of the composite building process. These ribbons packs were then loaded into the transfer assembly to use the ribbon clamps with the base plate for holding the ribbons in position.

3.2 Consolidation Methods

3.2.1 Coupon Samples

Two methods for consolidating the ribbons within the aluminum were attempted following the detwinning of the NiTi ribbons. The first method did not involve any pretreatment to the previously welded layers of aluminum, Figure 3.8. Therefore,

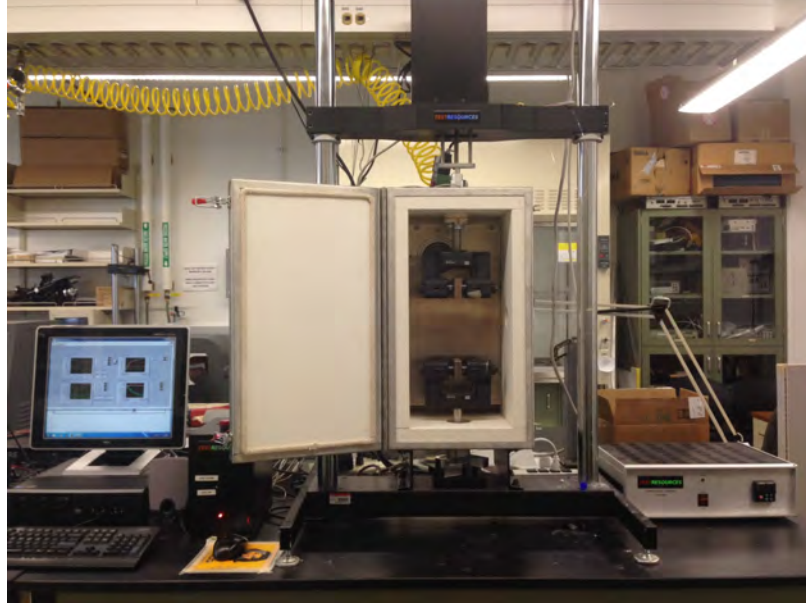


Figure 3.7: Load frame used for the detwinning of shape memory NiTi ribbons.

a single welding pass was made over the detwinned ribbons that were held in position by the clamps on either end. The second method involved milling channels in the aluminum matrix using the CNC milling feature of the UAM machine prior to clamping the ribbons to the base plate, Figure 3.9. The milling was performed with a 0.41 mm (0.016") diameter, two-fluted, square, carbide end mill, with a travel speed of 1.83 cm (0.72") per minute and rotational speed of 6000 revolutions per minute. The number of passes varied according to the width necessary to accommodate the size of the material. The coolant used during the milling processes was 2-propanol that was 90 percent pure or greater. It also aided in chip removal during the milling operations. The coolant was used to ensure the surface remained clean and dried quickly for welding following the machining operations; conversely, traditional CNC milling systems use a cutting fluid that leaves the surface covered in a thin layer

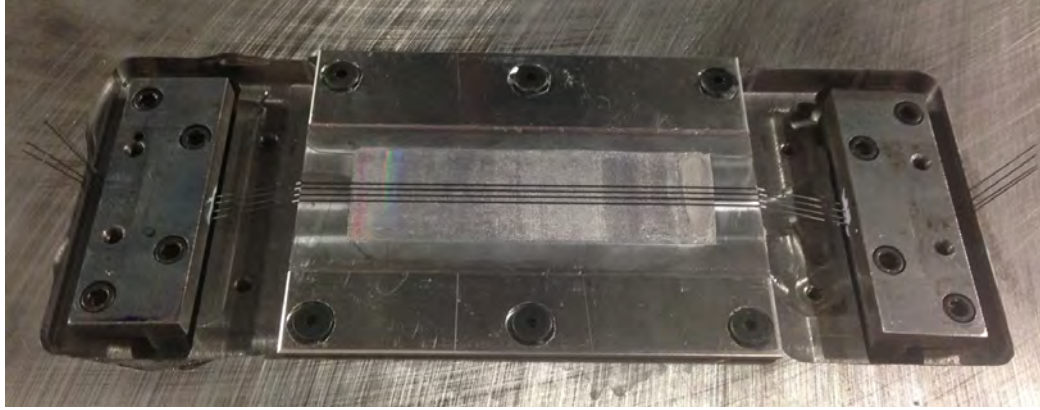


Figure 3.8: Production of coupon-sized sample before welding pass with ribbons lying on structure surface.

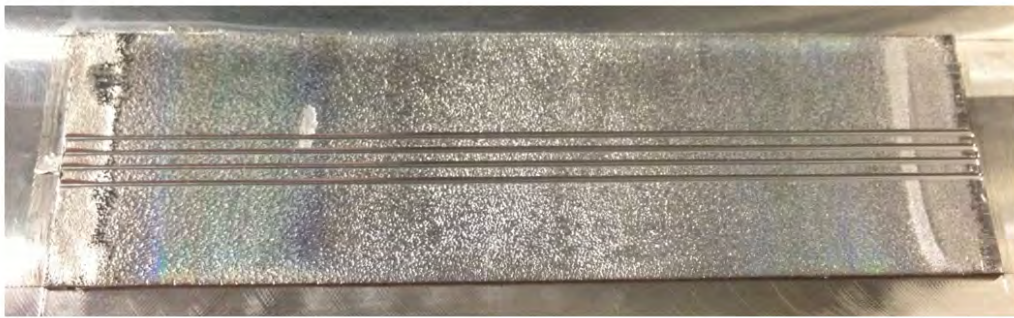


Figure 3.9: Production of coupon-sized sample following the milling of channels for the NiTi ribbons.

of fluid. The high purity enabled the use of 2-propanol without causing significant oxidation of the components within the UAM machine. Following the machining of the channels, the ribbons were transferred and bolted to the base plate.

3.2.2 Large Geometry Samples

The large geometry samples prepared in this study were fabricated to determine if it is possible to produce pieces greater than 25.40 cm (10.00”) in length and reach a build height of at least 0.64 cm (0.25”). Because this was the goal of the larger pieces, the fibers were only embedded within the central portion of the final structure, Figure 3.10. In addition, the ribbons for the larger composites were not de-twinned. Therefore, the ribbon packs were directly loaded into the longer transfer assembly. Because the channels proved successful in consolidating the NiTi ribbons in the coupon samples, they were also used for the large scale composites. With a travel speed of only 1.83 cm (0.72”) per minute, it would have taken approximately two hours to complete the channels for a single layer of NiTi fibers as well as a considerable amount of 2-propanol. To avoid these issues, production of the channels was done by the UAM machine’s 40W, neodymium-doped yttrium orthovanadate (Nd:YVO₄) laser system. With adjusted parameters, Table 3.1, the laser system was able to create channels in about half the time than it would have taken the milling system, Figures 3.11 and 3.12. The sequence for making a channel required eight passes side-by-side to achieve the desired width. This was repeated eight times over the same area to reach the desired depth. Because aluminum is highly reflective, a portion of the UV radiation used to cut the material was reflected away rather than being absorbed and utilized to ablate the material, forcing the number of passes to be higher than if the light was absorbed. Following the laser ablation process, the channels were cleaned out with a mechanics pick, a wire brush, and small amounts of 2-propanol to ensure any remnant particles from the process were no longer present. The ribbons were then placed in the channels using the larger transfer assembly, and

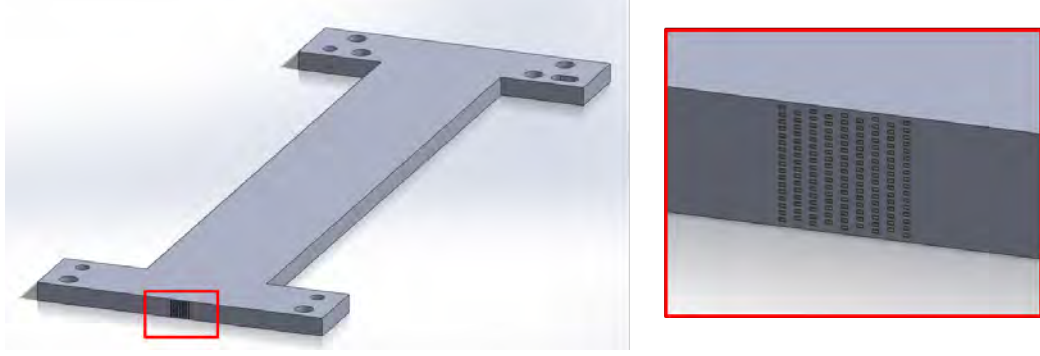


Figure 3.10: Rendering of the large geometry composites used to develop fabrication methods for pieces approximately 27.31 cm (10.75”) in length and 0.64 cm (0.25”) tall. Concentration of ribbons within center provides appropriate area of study.

Table 3.1: Laser parameters used for the ablation of aluminum to make channels for the large geometry composites.

Laser Parameter	Value
Travel speed	2.54 m/min (100 inches/min)
Power percentage	85%
Pulse width	4 μ s

the ribbons clamps were bolted to the base plate. To ensure the ribbons were seated in their respective channels, a pass was made over the ribbons with the horn and an aluminum tape without the ultrasonics activated.

3.3 Consolidation Results

3.3.1 Coupon Samples

Multiple attempts were made using each fabrication method to determine which process did a better job at consolidating the NiTi ribbons while maintaining the

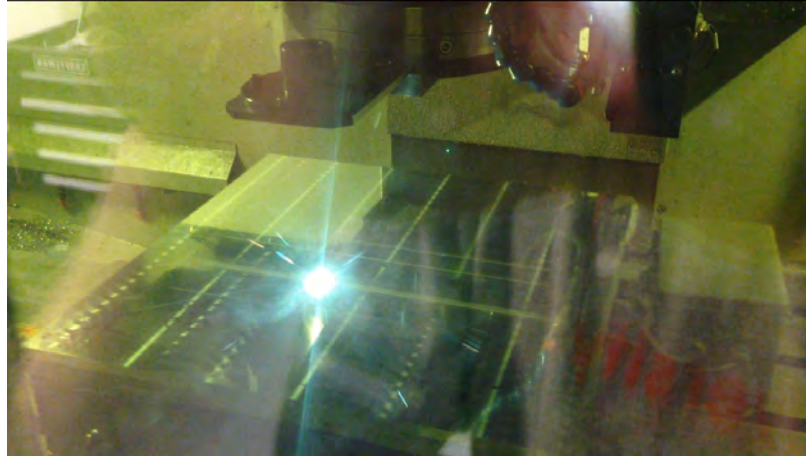


Figure 3.11: UAM machine's Nd:YVO₄ laser system in use to make channels in large geometry composites.



Figure 3.12: Example of channel pattern formed by the UAM machine's laser system.

desired geometry. The results of the first method were all failed attempts. From the failed attempts, three specific types of defects were consistently present within the product:

- Bunching of NiTi ribbons
- Aluminum not welding
- Splitting of the Al tape by the NiTi ribbons.

The bunching of the ribbons defect, Figure 3.13, was typically observed at the trailing edge of the composite being produced. This is caused by the ribbons having the freedom to move with little resistance in the direction perpendicular to the horn's movement at the end of the weld pass, where the leading edge was initially held in place by the normal force supplied by the horn. In cases where a section of the aluminum did not weld, Figure 3.14, the aluminum was unable to come into contact with the aluminum structure below the ribbons due to the interference provided by the ribbons. The final defect of the NiTi ribbons splitting the Al tape, Figure 3.15, is a result of the fiber being considerably harder than the aluminum material. These areas often yielded an uneven surface height that led to poor welding on subsequent layers.

The milling of channels yielded better results than trying to consolidate the ribbons without any prior machining. Initial efforts did involve some failures as the necessary channel depth for welding to occur was being determined. If the channel was milled too shallow the ribbons would bunch and split through the aluminum tape being welded. If the channels were at a depth that was greater than the ribbon's thickness, the ribbon would not be held in place. In this case, the ribbon could



Figure 3.13: Bunching of ribbons after a welding pass without the use of channels to maintain ribbon placement.

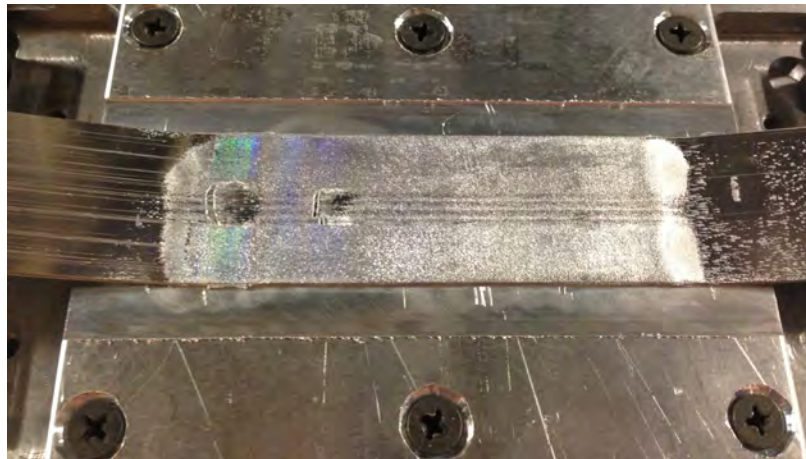


Figure 3.14: Area where aluminum did not weld because the ribbons kept the aluminum tape from making appropriate contact with the structure.



Figure 3.15: NiTi ribbons splitting through an aluminum tape. This defect occurred when the aluminum failed around the harder NiTi material.

easily be removed out of the matrix by pulling on one of the exposed ribbon ends, Figure 3.16. A final depth of approximately 0.03 mm to 0.05 mm (0.001" to 0.002") less than the ribbon thickness was determined to be the best depth for producing welds without visible defects.

If the channel milling process was utilized with too high of a volume fraction or there was a layer with a poor quality weld, delamination did occur, Figure 3.17. Delamination was the development of cracks between the layers of tape within the composite. Delamination was often observed when the composite had five or more layers of NiTi ribbons embedded within it. The issue of delamination above five layers is the result of the welded structure becoming more compliant as it becomes taller. To further investigate this defect, microscopy was used to study the cross-sections of the delaminated composites. Figure 3.18 shows the cross-section of an Al-NiTi composite that failed during the welding process by delamination. The cracks within

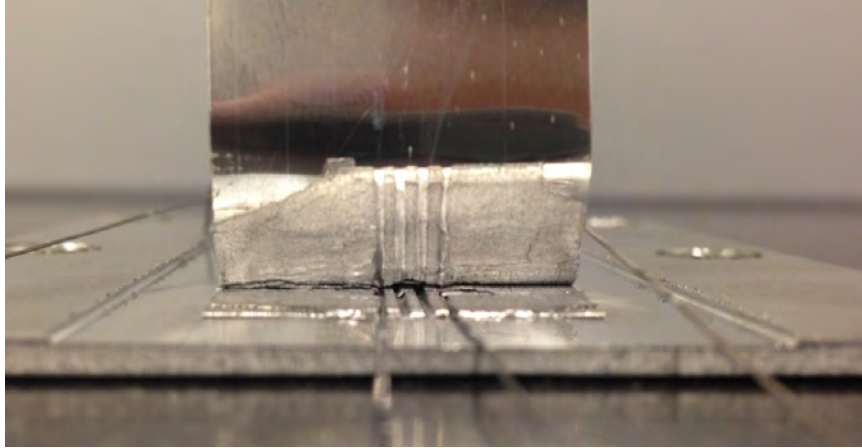


Figure 3.16: Failure of ribbon encapsulation (center ribbons) when the channel depth was too great. Failure allowed for ribbons to be pulled from the channels or be rotated within them.

the composite are more severe at the upper most layers, as would be the result from the increased compliance of the structure at the taller build heights. In addition, it is apparent that the cracks propagate from the corners of the ribbons as well as along planes within the composite. The development of cracks from the corners of the ribbons suggests that large amounts of stress exist in these regions. The geometry of the ribbons with their corners produce stress concentrations in these areas. Once the cracks began, the planes produced by the geometry of the ribbons facilitate shear failure between the tape layers. To reduce this issue, the top of the ribbons in one layer were offset from the bottom of the ribbons in the next. Coupons with shape memory ribbons rarely displayed the delamination defect. The lack of delamination in the shape memory composites is the result of the lower volume fraction of NiTi fibers within the composite, implying that a larger amount of aluminum between

Delamination
Line



Figure 3.17: Extrenal view of delamination within a composite.

the embedded ribbons helps carry the shear load within the matrix thus preventing delamination.

3.3.2 Large Geometry Samples

Two attempts at the large geometry builds were made for this study. The first attempt was unsuccessful due to significant defects within the regions containing the fibers. The second attempt was completed with minimal defects within the composite region. In both attempts, regions were present where the aluminum tape did not weld to the structure, Figures 3.19 and 3.20 for the first and second attempts, respectively. The cause of the unwelded regions was unevenness of the weld surface. During the first attempt, nothing was able to be implemented to correct the defect. However, during the second attempt, a recovery process was used to correct this issue. Recovery involves the use of a face mill to level the top surface of the structure. The recovery process helped to level the weld surface in the second build, but the face mill caught the free end of the one of the aluminum tapes along the leading edge and pulled a corner of the piece apart, Figure 3.21. The section of the structure around the defective corner did not weld afterwards. Furthermore, this region propagated into the structure as subsequent layers of aluminum were unable to be welded near this

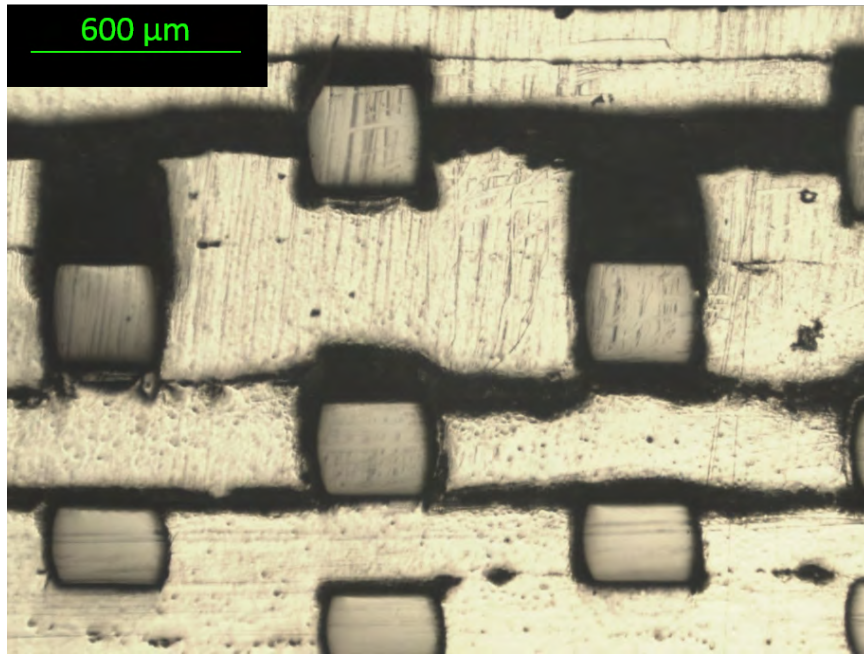


Figure 3.18: Cross-sectional view of delamination failure. The crack propagation from the corners of the NiTi fibers are the result of stress concentrations at the shape geometric changes.

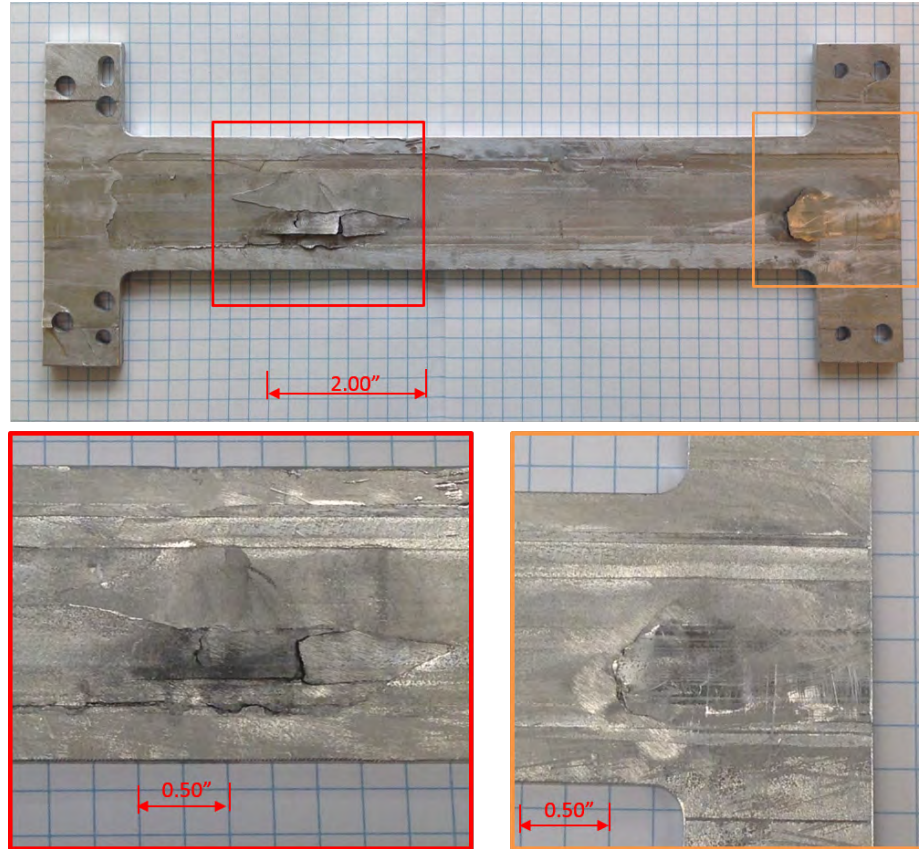


Figure 3.19: Area within the first large geometry sample, where aluminum did not weld to underlying structure.

area due to the surface becoming increasingly uneven. Recovery was not attempted to rectify this issue, as it would have exacerbated the defect.

Once the composite was removed from the build plate, more regions of unwelded areas were noticeable primarily along the seams of tapes where the overlapping of tapes caused unevenness of the surface, Figure 3.22. Because no further attempts were made to level the surface using recovery following the corner defect, the defects along the seams increased as the number of aluminum tapes increased. From views of the composite's ends, the seam issue lead to welding errors near the ribbons. NiTi

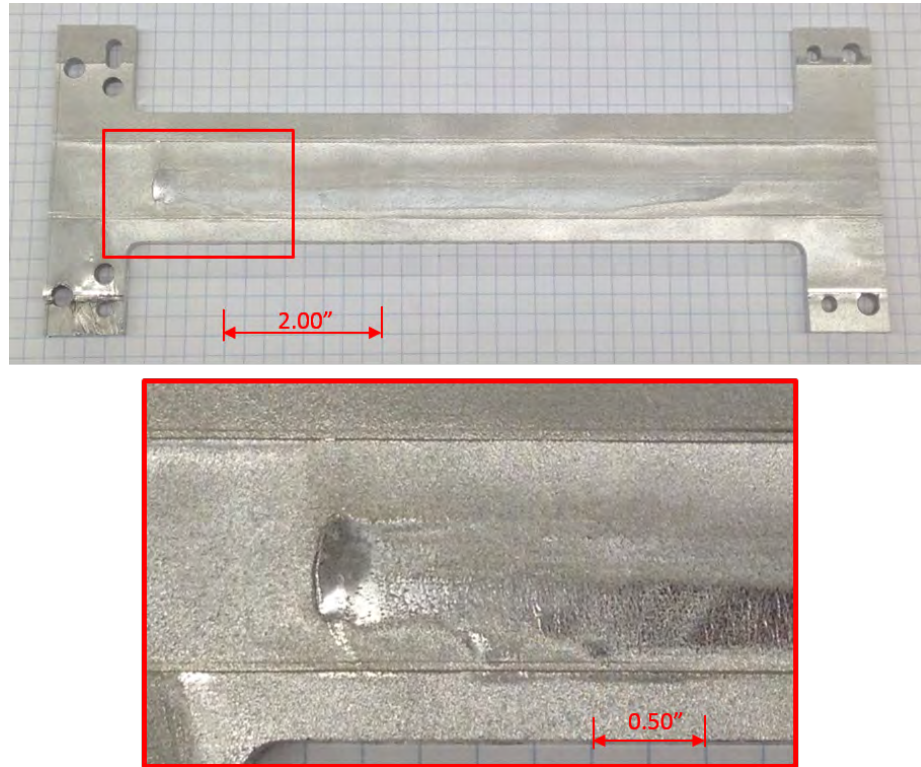


Figure 3.20: Failure of aluminum to weld to composite structure in the second large geometry sample.

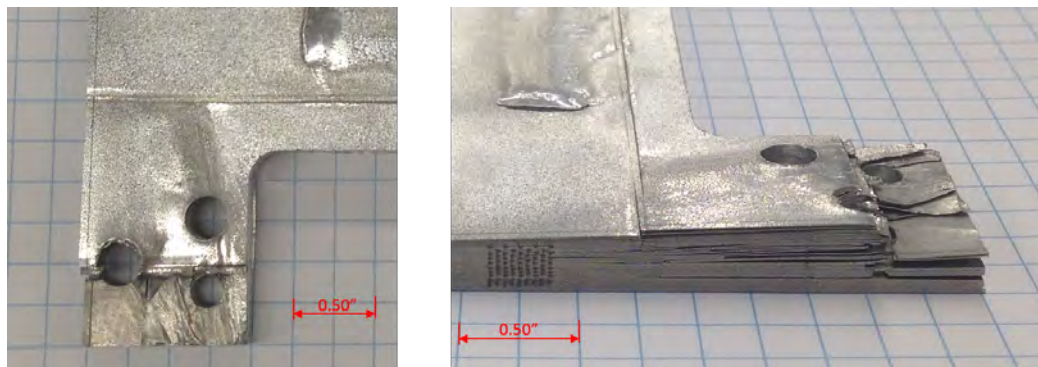


Figure 3.21: Defect at a corner within the second attempt at large geometry build produced by the face mill catching a loose tape end and ripping a portion of the structure apart. Following weld attempts over this region were unsuccessful, because the uneven surface prevented bonding from occurring.

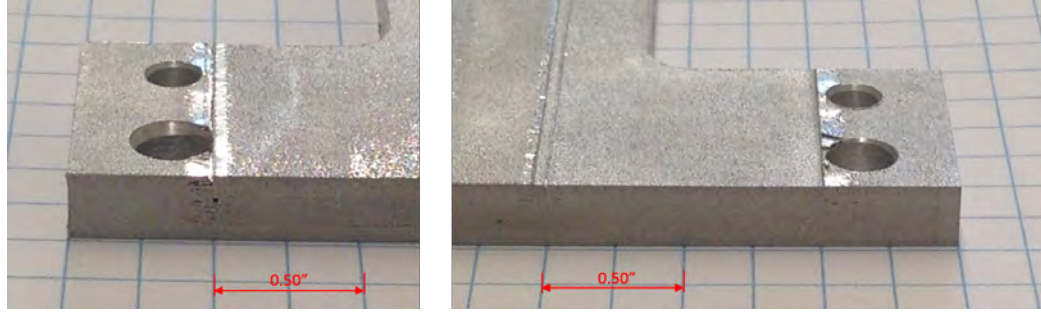


Figure 3.22: Defects along the seam lines within the composite due to an uneven surface, which could not be repaired as recovery of the surface would result in additional damage to the corner defect already present.

volume fraction also decreased as the composite's height increased. This reduction is the result of additional tapes of aluminum being welded between the NiTi layers to help stop the defects from spreading. Of the defects within the structure, the majority of the problems are primarily located near the ends and as part of the flanges.

3.4 Sample Removal and Post-Processing Procedures

Post-processing is required following any UAM build for at least the removal of the component from the sacrificial build plate. In addition, operations may be required to ensure the final geometry and features of the structure meet the design specifications. Post-processing of the pieces within this study were carried out both manually and via programmed machining operations.

3.4.1 Coupon Samples

The removal process of the coupon samples started with CNC milling operations in the OSU UAM machine using a four-flute, 0.95 cm (0.375") diameter, square, end mill to machine the excess aluminum away from the composite. Multiple passes were

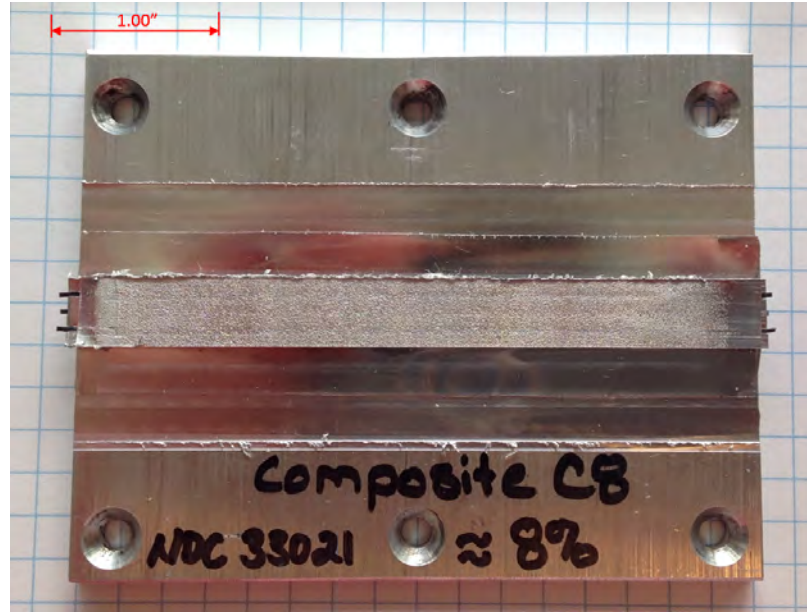


Figure 3.23: Coupon size sample following CNC milling operations within the UAM machine to mill the component to the proper width.

made to remove the material with a final finishing pass to ensure clean edges were left on the composite. After the final pass, the top of the build plate was left clean except for the composite which remained in the middle of the plate, Figure 3.23. By using the UAM milling system, it was ensured that the edges of the composite were nearly parallel to the embedded ribbons. Once the width of the composite was milled to size, the build plate was removed from the base plate.

A mill was then used to remove the build plate from the underside of the composite by clamping the build plate in a vice upside down. A four-flute, 0.63 cm (1/4") diameter, square, carbide, end-mill was used to make the pocket. Passes were made to remove 0.38 mm (0.015") of build plate material at a time to ensure the structure and plate did not build up significant amounts of heat, affecting the composite's

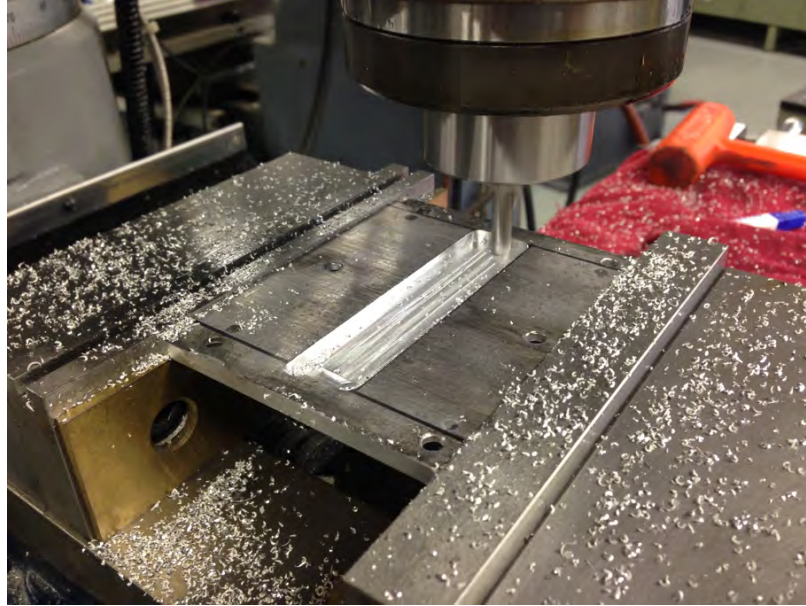


Figure 3.24: Milling operation using a four-flute, 0.63 cm (1/4") diameter, square, carbide, end-mill to remove the build plate from the composite structure.

integrity. Final passes were made removing 0.08 mm (0.003") at a time to reduce any unwanted downward force from the end-mill and to keep the end-mill from taking too much material off, exposing the NiTi ribbons, Figure 3.24. With the build plate removed, the composite remained, spanning a gap in the build plate from one end to the other that typically measured 8.89 cm (3.5").

From this point, all remaining post-processing was done by saw. First, the large sections of the build plate which ran parallel to the composite were removed using a vertical band saw running at 600 feet per minute. An airflow was used to remove the chips from the surface during the cuts and to keep the part cool. The resulting piece was the coupon with small sections of the build plate welded to the ends, Figure 3.25. These ends were the last part to be removed. The removal of the ends was completed



Figure 3.25: Coupon sample following the removal of build plate using milling and vertical band saw. The only remaining parts are found of the ends of the composite.

by a SXJ2 Precision Wire Saw with a diamond impregnated wire, Figure 3.26, running at 175 revolutions per minute. The slow cutting process with the diamond blade is one of the few ways NiTi material can be cut due to its hardness. During the wire cutting process, the sample was held in place on a graphite mounting block using mounting wax. Recirculated deionized water was used as coolant for the wire saw system. Because the range of the mounting stage was limited to 5.08 cm (2.00"), the composite had to be dismounted and remounted to cut both ends. Once the ends were removed, acetone was used to clean the coupon of any residual debris and mounting wax, Figure 3.27.

3.4.2 Large Geometry Samples

The removal process for the larger geometry samples started with CNC milling in the OSU UAM machine with the four-flute, 0.95 cm (0.375") diameter, square, end-mill, just as the coupon samples did, but required additional programming to



Figure 3.26: SXJ2 Precision Wire Saw used to trim off the ends of the coupon samples.



Figure 3.27: Example of final coupon sized Al-NiTi composite produced via UAM.

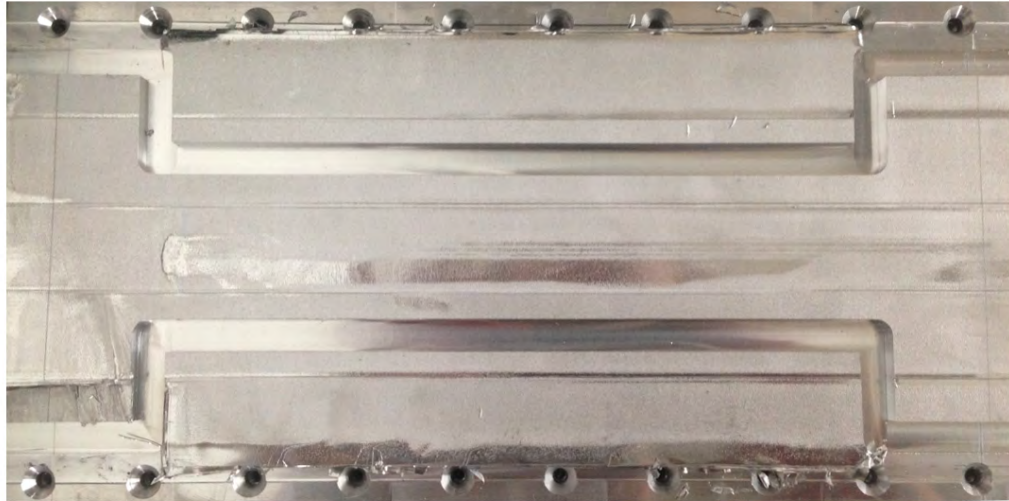


Figure 3.28: Large geometry sample following CNC milling operations within the UAM machine to achieve the desired outline.

produce the outline of the proposed structural component, Appendix B. As before, multiple passes were used to create the outline followed by a finishing pass for clean edges, Figure 3.28. The build plate was then removed from the base plate for drilling and milling of the holes and slot respectively, Figure 3.29. The machining for the holes and slot were done manually to ensure the placement was correct and the depth was sufficient.

As with the coupon, the build plate needed to be removed from the underside of the welded structure. To remove the build plate, a Haas ®, 3-axis, CNC milling machine was used. The Haas ® machine was utilized instead of the UAM CNC system because of the greater coolant flow rate, Figure 3.30. The build plate was bolted to a custom fixture, Figure 3.31, which was clamped in a vice. The fixture was used to help reduce vibrations within the plate during machining and to prevent buckling of the build plate as the material was removed from it. The removal of the build plate

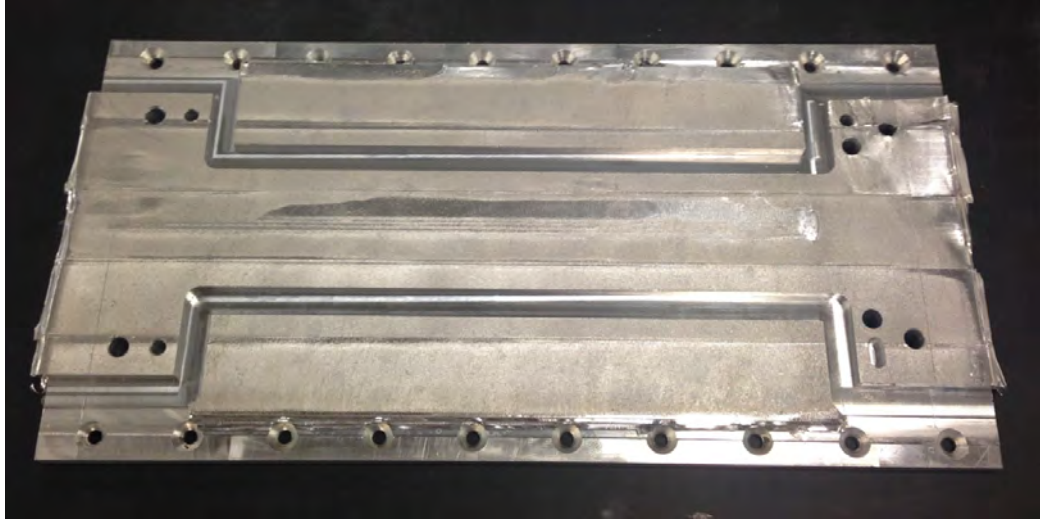


Figure 3.29: Large sample following the drilling of holes and the milling of a slot.

was done in two steps. The first involved the milling of four pockets to leave behind support bridges along both the length and width of the plate, Figure 3.32. Once the pockets were made, removal of the bridges was done to complete the removal of the build plate from the bottom of the welded structure.

Electrical discharge machining was the final step taken to remove the large structures from the build plate since the larger piece could not be accommodated in the wire saw. A cutting rate of 6.99 cm (2.75") per minute was used make the 10.16 cm (4.00") cuts on either end of the structure to produce the final part, Figure 3.33.



Figure 3.30: Haas ® CNC milling machine, removing the build plate from the large geometry sample.

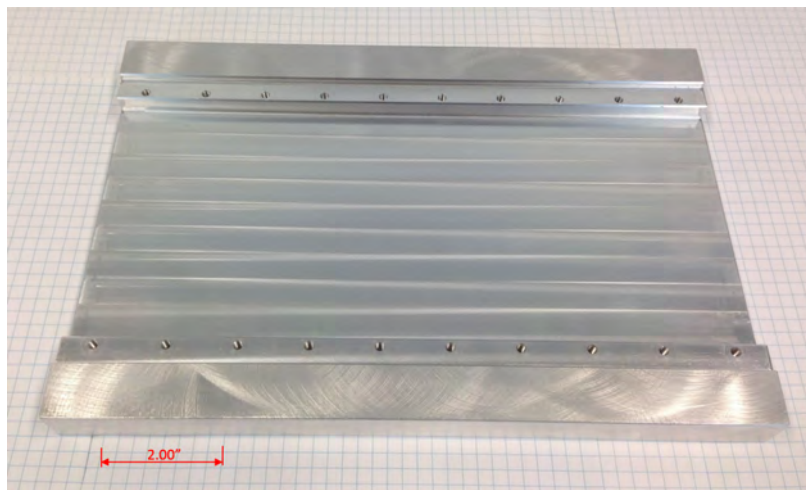


Figure 3.31: Fixture used for securing the build plate of the large samples while CNC milling operations were performed to remove sections of the build plate from the composite.

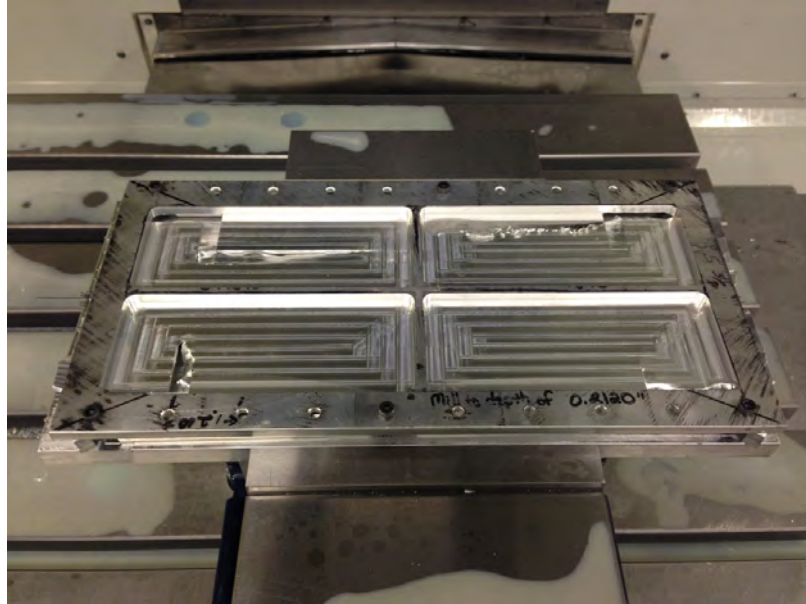


Figure 3.32: Pockets produced by the removal of the build plate from the large geometry composites. Bridges were left to maintain stability during milling operation, and later removed once the pockets were completed.

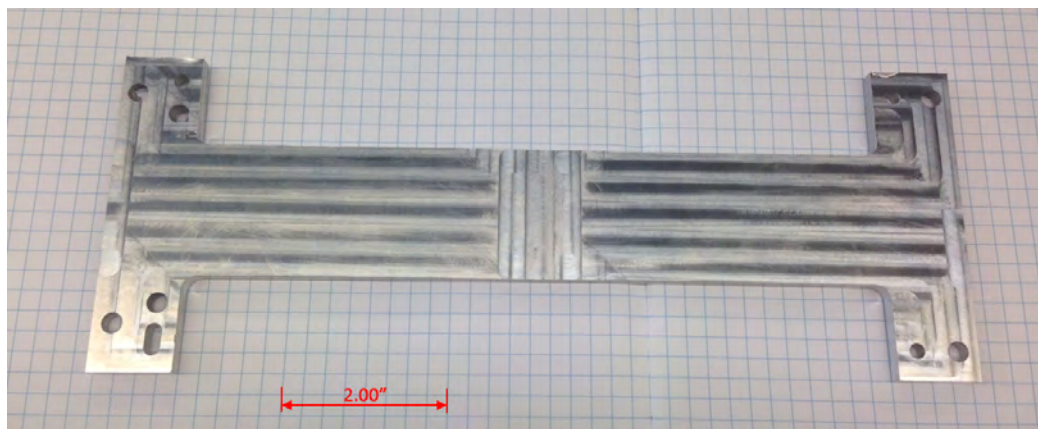


Figure 3.33: Final large geometry part produced following the electrical discharge machining of the composite ends.

CHAPTER 4

TESTING AND RESULTS OF MULTI-LAYER AL-NITI COMPOSITES

Using the production methods outline in Chapter 3, multiple Al-NiTi coupons were manufactured with either pseudoelastic or shape memory fibers, Table 4.1. These coupons were measured to determine various thermal, mechanical, and electrical properties of the composites. Specifically, procedures were performed to measure the coefficient of thermal expansion in the rolling direction, thermal diffusivity in the out-of-plane direction, and electrical conductivity in the rolling direction.

4.1 Coefficient of Thermal Expansion Testing

4.1.1 Test Set-Up and Procedure

Measurements were performed to determine the coefficient of thermal expansion of both pseudoelastic and shape memory fiber composites. The tests were performed using a custom thermal chamber made from a 15.24 cm x 15.24 cm (6" x 6") steel enclosure box lined with foil faced, fiberglass insulation, Figure 4.1. The top of the enclosure was machined to allow for viewing through a glass window. Two additional holes were made in the enclosure: the first was made to allow for heated air to be supplied to the chamber, and the second to allow sensor wiring to exit the chamber.

Table 4.1: NiTi material type, fiber size, and NiTi volume fraction data on coupon composites produced for testing. Note: The numbering for the shape memory composites begins at 6, as previous composites had been built by a previous researcher within the lab.

Composite		Composite Characteristics	
Material	Number	NiTi Area, [mm ²]	NiTi Vol. Fraction, [%]
Pseudoelastic	1	6.3e-2	9.8
	2	6.3e-2	16.1
	3	6.3e-2	9.3
	4	6.3e-2	12.4
	5	6.3e-2	10.0
	6	6.3e-2	Delmainated
	7	6.3e-2	14.0
Shape Memory	6	3.1e-1	12.8
	7	1.3e-1	19.8
	8	1.3e-1	6.2
	9	1.3e-1	7.9

The heated air in the tests was supplied by a Milwaukee Variable Temperature Heat Gun with Fahrenheit display, which was deflected upon entering the thermal chamber by a baffle made from an aluminum C-channel. The samples were mounted in the enclosure in a cantilevered condition to allow for free strain conditions, Figure 4.2. Two samples were mounted at a time: a UAM produced aluminum reference piece and the Al-NiTi composite. Each sample was equipped with two Micro-Measurements WK-13-031CF-350 strain gages [27] and a J-type thermocouple. The strain gages were chosen for their self-temperature compensation values of 13, which equates to $23.2 \mu\epsilon/^{\circ}\text{C}$ [28], the approximate CTE of aluminum. One strain gage was placed on the top-side of the sample and the other on the bottom [29]. Each strain gage was independent of the others. The strain gages were attached to the samples using M-Bond 200 for the pseudoelastic samples and M-Bond 300 for the shape memory

composites. Two different adhesives were used because the higher testing temperature of the shape memory coupons was outside the usable range of M-bond 200. The strain gages were capable of performing within both temperature ranges [26]. The outputs from the sensors were conditioned using a National Instruments cDAQ-9748 data acquisition system run by LabView. The data acquisition system used a NI 9237 module for the strain inputs and a NI 9214 module for the thermocouple inputs. Before the first cycle on any composite, the strain gages are zeroed within the LabView software. The test was broken up into four intervals:

1. Turn on heat gun to lowest fan speed and change the set point temperature on the heat gun to 240°F (pseudoelastic composite) / 350°F (shape memory composite) and insert heat gun nozzle into chamber. Run for 30 minutes.
2. Change the set point temperature on the heat gun to 70°F. Run for 20 minutes.
3. Remove the heat gun from the enclosure. Keeping the set point at 70°F, move the heat gun nozzle approximately 7.62 cm (3.00”) away from the hole it was in and direct the air flow into the chamber. Run for 30 minutes.
4. Turn the heat gun off. Run for 25 minutes.
5. End test.

These intervals were repeated a minimum of three times for each composite that was tested.

4.1.2 Results

Thermal expansion tests were conducted on composites P-1, P-2, P-4, C-7, and C-9, where "P" and "C" stand for pseudoelastic and shape memory, respectively, and

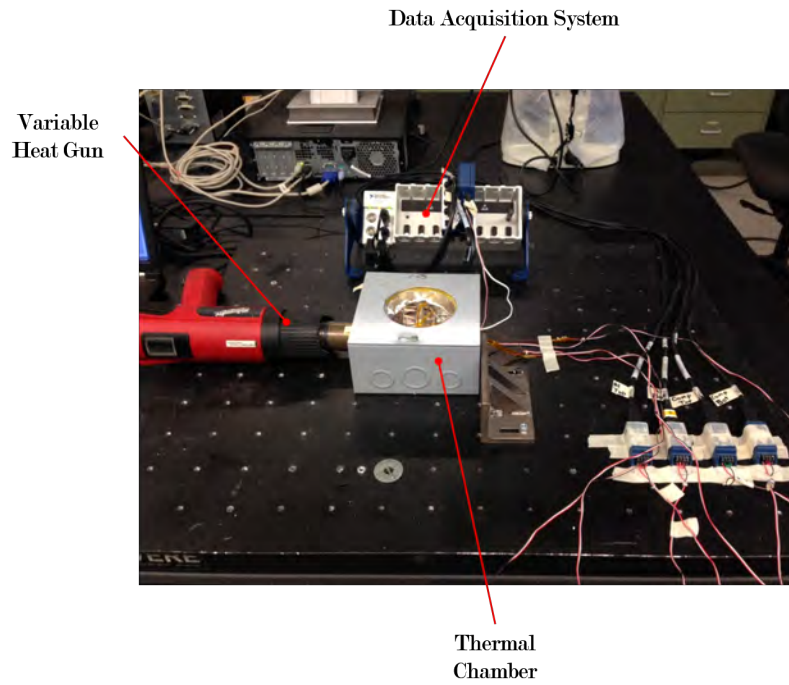


Figure 4.1: Set-up used for conducting coefficient of thermal expansion tests on coupon sized Al-NiTi composites.



Figure 4.2: Al-NiTi composite sample and reference aluminum sample mounted in cantilever position for performing CTE tests.

the number corresponds to those listed in Table 4.1. The data sets from the tests were analyzed using MATLAB. To carry out the analysis, the strain data from the aluminum reference was averaged according to:

$$\frac{\epsilon_{\text{top}} + \epsilon_{\text{bottom}}}{2} = \epsilon_{\text{avg}}. \quad (4.1)$$

The same averaging of data was done to the composite data. After averaging, the thermal strains, top, bottom, and average, from the reference sample were subtracted from the corresponding strains of the composite to determine the resolved strains of the composite by:

$$\begin{aligned} \epsilon_{\text{c,top}} - \epsilon_{\text{ref,top}} &= \epsilon_{\text{res,top}} \\ \epsilon_{\text{c,bottom}} - \epsilon_{\text{ref,bottom}} &= \epsilon_{\text{res,bottom}} \\ \epsilon_{\text{c,avg}} - \epsilon_{\text{ref,avg}} &= \epsilon_{\text{res,avg}}. \end{aligned} \quad (4.2)$$

This is possible due to the self-temperature compensated value of the strain gages, as mentioned previously, being approximately the CTE of aluminum. With the thermal strains removed, the theoretical expansion of aluminum is added back into strains of the composite to determine the actual strains of the composite:

$$\begin{aligned} \epsilon_{\text{res,top}} + \alpha_{\text{Al}}\Delta T &= \epsilon_{\text{act,top}} \\ \epsilon_{\text{res,bottom}} + \alpha_{\text{Al}}\Delta T &= \epsilon_{\text{act,bottom}} \\ \epsilon_{\text{res,avg}} + \alpha_{\text{Al}}\Delta T &= \epsilon_{\text{act,avg}} \end{aligned} \quad (4.3)$$

where ΔT is given by:

$$\Delta T = T - T_o. \quad (4.4)$$

Following the data processing, the actual results for each of the strains across all cycles were plotted versus temperature. Figures 4.3, 4.4, and 4.5 provide examples of these plots for top, bottom, and average strains from C-7, while the rest can be found in Appendix C. From the plots, a best fit analysis was performed on the data to determine the coefficient of thermal expansion both as the temperature was increased and decreased, Table 4.2. If the region studied was linear, the slope of the best fit line was the CTE of the material. For regions with curved results, a second-order polynomial was used to fit the data. In this case, the derivative of the second-order polynomial was evaluated over the region's temperature range, and the average of all the values was determined to be the average CTE of the composite over said range.

This process was used for C-9, but involved the fitting of second-order polynomials to three separate portions of the overall transformation region, Figure 4.6. The derivatives of these polynomials were evaluated over their respective temperature ranges, Figure 4.7, and an overall average was taken from them to determine the average CTE of $1.6 \mu\epsilon/^\circ\text{C}$ for the heating portion of C-9's first cycle.

Because the transformation temperature of the NiTi ribbons varied based on its material properties and embedded stress state, the CTE of each pseudoelastic NiTi composite was measured over the 23°C to 100°C range and the shape memory NiTi composite's from 55°C to the maximum temperature of each test. Any variance from these ranges was the result of a clearly defined transformation region that decreased the composite's overall CTE to a desired value within an alternate temperature range.

From Table 4.2 it is apparent that the composites with the pseudoelastic NiTi ribbons performed consistently from one cycle to the next, but the composites with the shape memory NiTi ribbons did not. Instead, these composites often performed

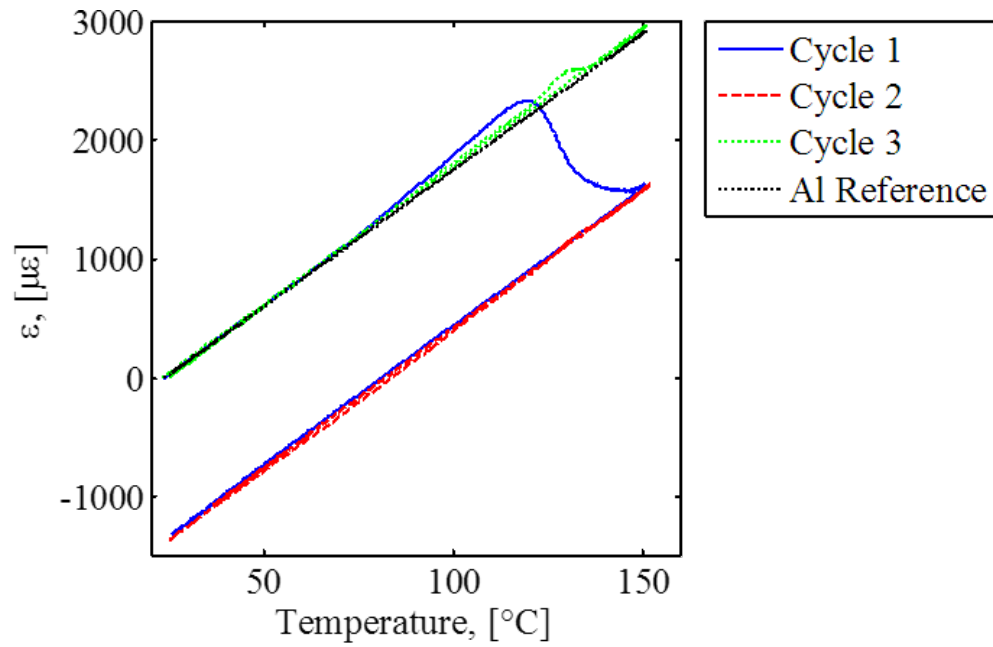


Figure 4.3: Example of CTE testing results for the top strain. C-7's results are shown here.

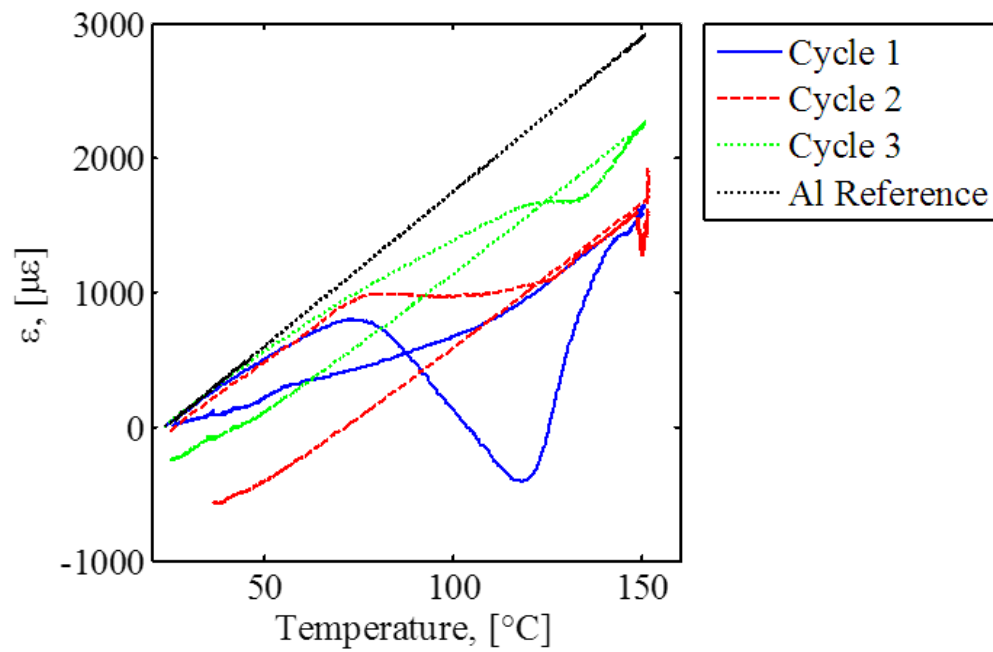


Figure 4.4: Example of CTE testing results for the bottom strain. C-7's results are shown here.

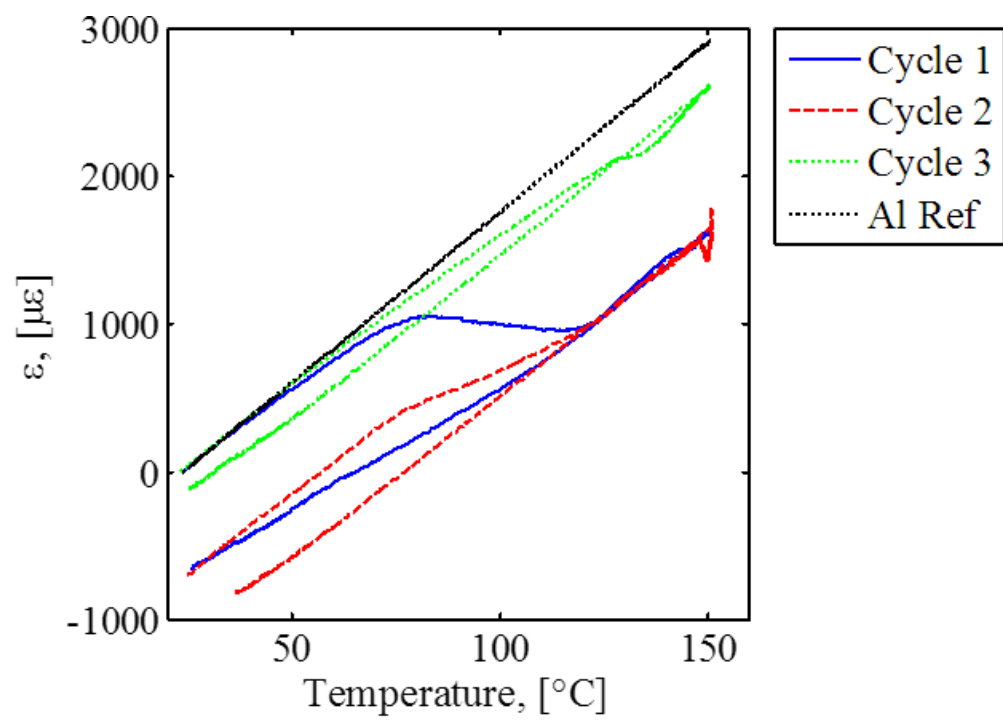


Figure 4.5: Example of CTE testing results for the average strain. C-7's results are shown here.

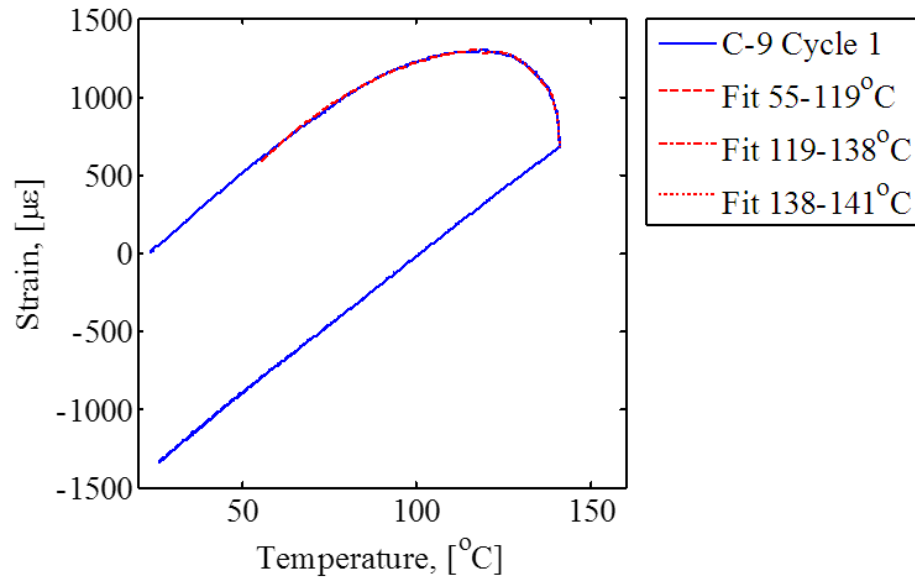


Figure 4.6: Stress-temperature plot of C-9's first cycle during CTE testing with fitted lines over the transformation region.

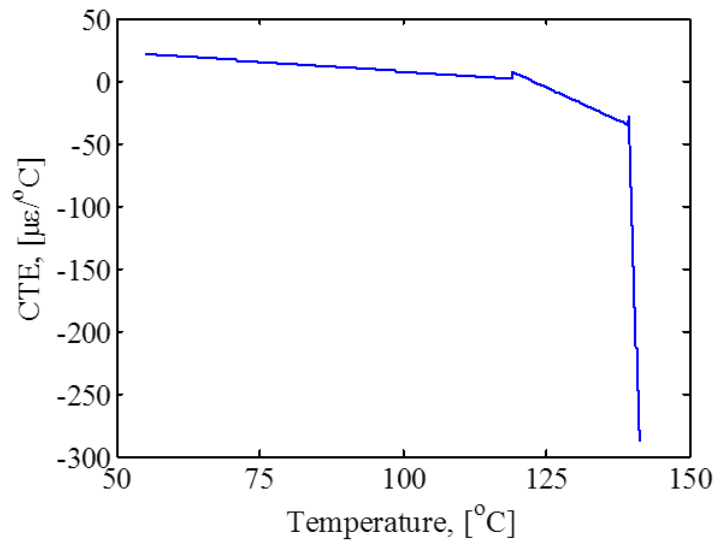


Figure 4.7: Plot of C-9's instantaneous CTE versus temperature based on the derivatives of the fitted lines in Figure 4.6.

Table 4.2: CTE results for various pseudoelastic NiTi and shape memory NiTi composites. These results are reported $\pm 2.4 \mu\epsilon/^\circ\text{C}$ at 95% confidence. *Temperature range for CTE calculation was from 65°C to 125°C , as the transformation region was observed over this range. **Solder joint on strain gage wire failed during cooling portion of cycle.

Composite	Coefficient of Thermal Expansion, [$\mu\epsilon/^\circ\text{C}$]					
	Cycle 1		Cycle 2		Cycle 3	
	Heat	Cool	Heat	Cool	Heat	Cool
P-1	20.7	20.8	20.8	21.3	20.8	20.8
P-2	13.9	13.4	13.7	13.5	14.1	13.6
P-4	17.7	21.3	20.7	21.1	20.7	21.1
C-7 *	9.6e-2	17.0	13.4	22.1	19.3	22.4
C-9	1.6	17.4	14.3	17.5	12.5	**

well on the heating portion of the first cycle, with average CTEs below $2 \mu\epsilon/^\circ\text{C}$, and with CTEs in excess of $10 \mu\epsilon/^\circ\text{C}$ for all other measured regions. These results suggest that the shape memory NiTi composites partially failed during the heating portion of the first cycle. Complete failure was not present as a reduction in CTE from pure aluminum was still achieved following the initial heating of the composites.

As mentioned, some of the CTE results demonstrated curved regions following the NiTi material's transformation. This curvature in the strain-temperature plot is caused by the NiTi material, as it lags in offsetting the expansion of the aluminum matrix. The lag is a result of the NiTi endothermic phase transformation process. During the phase transformation, energy is absorbed by the fibers to transform from the detwinned martensite phase to the austenite phase. The absorption of the energy by the fibers takes enough time to cause a delay and produce a curve within the CTE test results within the upper temperature regions of the CTE tests when the heating rate decreases as the steady state condition is approached.

Overall, the results of the CTE tests provide evidence that, aside from P-2, none of the pseudoelastic NiTi composites exhibited any reduction in CTE due to the transformation of the embedded ribbons, and the shape memory composites only exhibited the desired reduction in CTE for the heating portion of the first cycle. Differential scanning calorimetry (DSC) tests and microscopy were used to determine the cause of these results.

4.1.3 Differential Scanning Calorimetry Tests

Differential scanning calorimetry is a test that measures the difference between the heat flow into a sample piece versus a reference as they are exposed to a temperature profile. The result provides evidence to when endothermic and exothermic reactions are taking place within the sample. In this study specifically, the test was used to determine when the martensite to austenite transformation of the embedded pseudoelastic NiTi ribbons was taking place. For the test, composites P-3 and P-5 were tested. P-3 was made with the same process parameters and number of embedded ribbons as P-2, making its results directly comparable to the outcome of the CTE tests. P-5 was made with only one layer of embedded fibers that were held in the ribbon clamps throughout the entire build process. P-5 was made in this manner to determine if the ultrasonic vibrations from subsequent welding passes induced the recovery of the embedded ribbons during the fabrication process in a phenomenon known as ultrasonic lubrication [4].

Sample pieces were cut from both P-3, Figure 4.8, and P-5 using a Buehler, Isomet Low-speed, rotary saw with a diamond coated blade, Figure 4.10. The cut samples were cleaned with alcohol and rinsed with deionized water before being weighed for

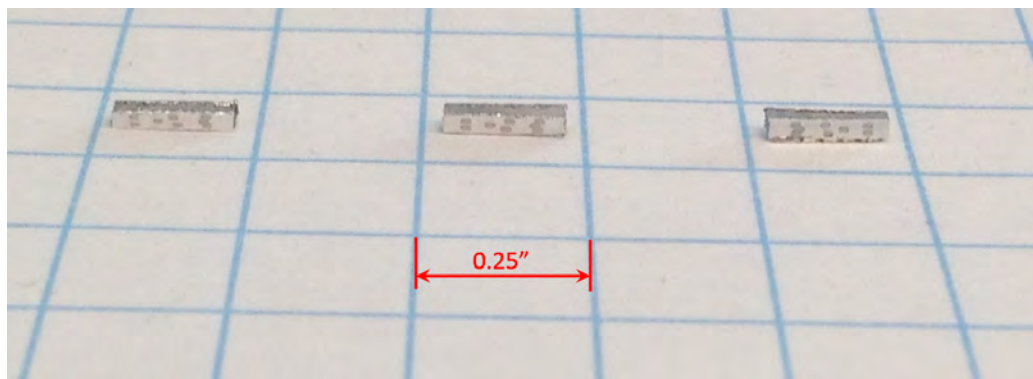


Figure 4.8: Example of samples cut for performing differential scanning calorimetry testing. Samples from P-3 are shown.

the DSC test. Once weighed, the samples were placed into aluminum measuring pans and sealed. A pan made with just pseudoelastic NiTi fibers and an empty reference pan were also made. Each sample was tested using a TA Instruments 2920 Differential Scanning Calorimeter with liquid nitrogen cooling and nitrogen purge gas, Figure 4.9. The temperature profile for which the tests were conducted started below -100°C and went to 150°C at a rate of 5°C per minute.

The results of the DSC tests, Figure 4.11, all show increases in heat flow per mass from around -30°C to 20°C , indicating that the ribbons within the composite were undergoing the endothermic transformation to austenite at the same temperatures as the fibers not in the composite. The only exception from this consistency, is the first sample of P-5, where the transformation did not begin until -5°C but still finished near 20°C . From these results, the conclusion was made that the pseudoelastic NiTi ribbons did not remain in the detwinned martensite phase upon being embedded within the aluminum matrix, or if they did, they did not remain there long before the ribbon-matrix interface failed, as was the case with the first sample of P-5. Furthermore, the



Figure 4.9: TA Instruments 2920 Differential Scanning Calorimetry system utilized for carrying out DSC tests.



Figure 4.10: Buehler, Isomet, Low-speed, rotary saw with a diamond coated blade used for cutting of Al-NiTi DSC samples.

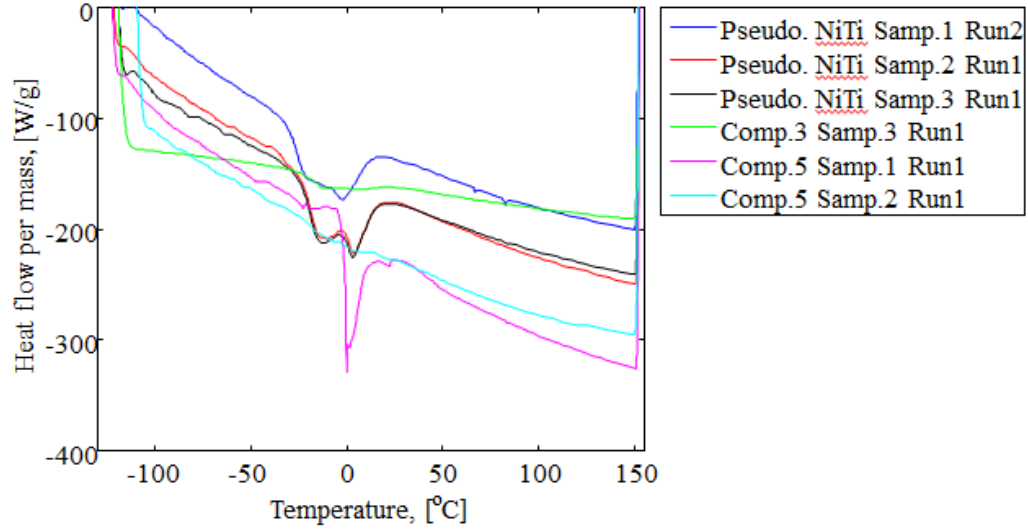


Figure 4.11: Results of the DSC tests performed on the pseudoelastic NiTi ribbons, composite P-3, and composite P-5.

results do not support the recovery of the prestress via ultrasonic lubrication, as the ribbons within composite P-5 still transform within the same temperature region as all the other composites and the pseudoelastic NiTi ribbons themselves.

4.1.4 Microscopy

Because the shape memory NiTi composites displayed a decreased CTE for at least a portion of one cycle, the interface between the matrix and fiber was determined to secure the ribbons as desired. Microscopy was used to determine why the composites stopped performing after the first cycle. To obtain micrographs of the cross-sections, samples were cut from the ends of the tested composites along with ends from the composites prior to testing. These samples were cold-mounted using Leco long-cure epoxy. After the epoxy cured, the mounted samples were removed from their molds

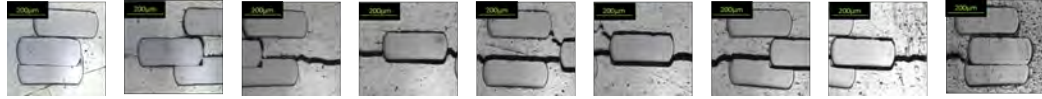


Figure 4.12: Series of optical micrographs taken of C-7's cross-section prior to being thermally cycled.

and underwent a polishing process. The polished samples were then viewed under an optical microscope.

The cross-section of the untested C-7 composite, Figure 4.12, first shows that the two outermost ribbons on each side of the first layer in the 5-6-5 pattern were encroached upon during the milling operation performed to make channels for the second layer of ribbons. In addition to the milling defects, there exists a number of cracks between the fibers. Both of these defects affected the interface between the fibers and the matrix, which in turn affected the ability of the fibers to offset the expansion of the aluminum. Following the CTE tests of C-7, the cross-section was again viewed under the microscope, Figure 4.13. The micrographs show that the cracks originally present within the composite grew and that additional cracks developed in the matrix around the fibers. This failure of the matrix in conjunction with the defects within the composite prior to testing were both causes of the composite's failure to produce the desired reduction in CTE past the first heating cycle.

The process of comparing the cross-sections before and after conducting the CTE tests was also performed on composite C-9. The cross-section of C-9 prior to testing, Figure 4.14, shows that that the aluminum under one of the fibers in the first layer developed a crack and was pulled away from the NiTi ribbon there. In addition, below each of the ribbons in the upper layer there are pits in the aluminum matrix



Figure 4.13: Series of optical micrographs taken of C-7's cross-section after being thermally cycled via the CTE test process. The micrographs are in reversed order from Figure 4.12 and mirrored due to the samples coming from opposite sides of a cutting plane.

suggesting that the tooling used to produce the channels for the ribbons was becoming dull and tore the aluminum rather than chipping it away. Despite these defects, no cracks due to stress concentrations were present. The micrographs after the CTE tests show a cross-section where the fibers and the matrix have still not developed any defects in addition to those seen before the testing. However, a majority of the fiber-matrix interfaces showed some partial form of failure during the test, as the ribbon ends are no longer flush with the face of the matrix, Figure 4.15. The recovery of the prestrain within only a fraction of the ribbons within C-9 support the results of a significant reduction in CTE for the heating portion of the first cycle and only a minor reduction in CTE for all additional cycles. The micrograph of the tested C-9 cross-section, Figure 4.16, displays this with the upper NiTi fibers being darkened, unpolished, and still having a saw cut finish. As the other fibers were not as recessed as the upper ribbons (indicating less recovery of the initial prestress than the upper fibers), they were made flush with the matrix face again during the removal of aluminum during the polishing process.

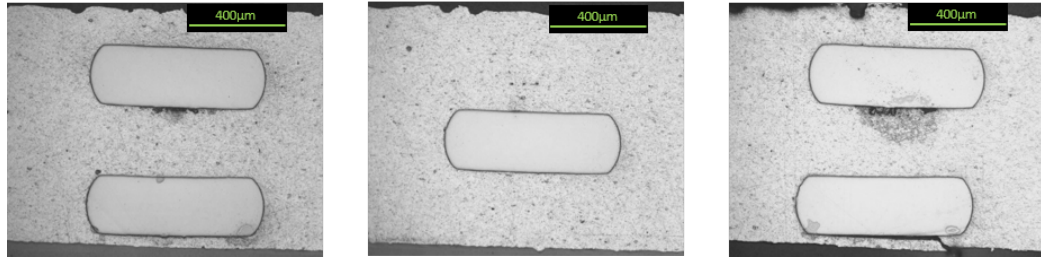


Figure 4.14: Series of optical micrographs taken of C-9's cross-section prior to being thermally cycled.

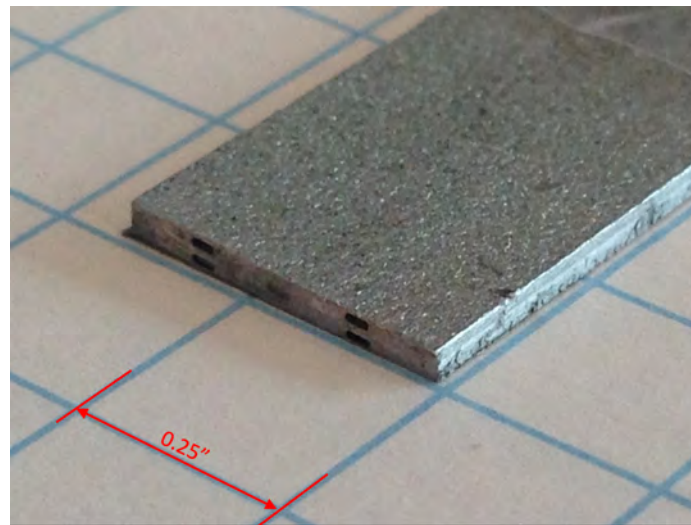


Figure 4.15: Image of the failed fiber-matrix interfaces within C-9, as the fibers are no longer flush with the matrix's face.

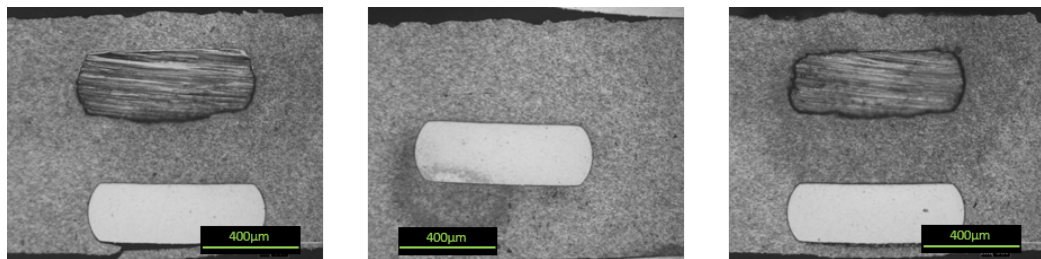


Figure 4.16: Series of optical micrographs taken of C-9's cross-section after being thermally cycled via the CTE test process. The micrographs are in reversed order from Figure 4.12 and mirrored due to the samples coming from opposite sides of a cutting plane.

4.1.5 Comparison of Composite Performance to SMA Composite Model

The results of the CTE tests show that the only composites that performed as desired were C-7 and C-9. Comparisons were therefore made between the test results of these two composite's first cycles and the predicted performance given by the SMA composite model. For composite C-7, the SMA composite model was run with the material property values for the shape memory material and a volume fraction of 19.8%. The result of the model was then plot versus the CTE test results for C-7's first cycle, Figure 4.17. From the plot, it is apparent that the performance of C-7 and the model are different, with the model transforming at a lower temperature than C-7 and the CTE of the model decreasing at a faster rate of $-43.2 \mu\epsilon/^{\circ}\text{C}$. The model indicates that C-7 had some layers of NiTi ribbons not contribute to the reduction of CTE, despite the performance of the composite meeting the desired results of a CTE within the $-5 \mu\epsilon/^{\circ}\text{C}$ to $5 \mu\epsilon/^{\circ}\text{C}$ range. The micrographs of C-7 support this evidence by showing that cracks developed around some of the ribbons and the interfaces between the fibers and the matrix were no longer secure. Because C-7 did produce a CTE of $9.6\text{e-}2 \mu\epsilon/^{\circ}\text{C}$, the model was used to determine the volume fraction of shape memory NiTi material necessary to produce the result shown by C-7. To determine the volume fraction, a guess and check method was utilized until the model result displayed a performance that was similar to C-7's first cycle. The result of the method came to the conclusion that an approximate NiTi volume fraction of 8.9% would have produced the results of C-7, Figure 4.18, where the regions of NTE following the transformation of the NiTi ribbons were both approximately $-3 \mu\epsilon/^{\circ}\text{C}$, (these regions were measured according to a different range than what was used for

Table 4.2). Although, the temperature at which the transformation began for C-7 is not the same temperature the model showed the transformation beginning. It was hypothesized that the reason for this variance was additional stress being applied to the fibers during the welding process. Therefore, the model was adjusted to include an initial stress of 400MPa, which shifted the model's result near the performance of C-7. The prestress of the NiTi ribbons was applied to the model in the form of σ_o which is found in Equation 2.7. The determination of an initial stress of 400 MPa was through the use of the shape memory material's phase diagram, which shows that to have an austenite start temperature of approximately 75°C, an initial stress of 400 MPa is required, Figure 4.19. By including the initial stress in the model, it indicates that there was some stress development within the fibers during the welding process, and C-7 produced the result it did during its first cycle with 8.9% NiTi volume fraction and an initial stress of 400 MPa.

Following the CTE test of C-9, the results were compared to the SMA composite model, as was done with C-7. The initial plot of C-9 and the model, Figure 4.20, once again do not match well, as the CTEs of the two are different, with the actual composite having a CTE of 6.1 $\mu\epsilon/^\circ\text{C}$ and the model -1.0 $\mu\epsilon/^\circ\text{C}$. The transformation temperatures at the start of transformation are also different, as the model shows the transformation starting at 53°C and the actual composite begins to show significant signs of transformation around 75°C. To make the transformation starting temperatures approximately the same, an initial stress of 350 MPa was added to the model. The initial stress was again determined by use of the phase diagram for the shape memory material. The result of the included initial stress shifted the transformation temperature near to the beginning of transformation in the composite, Figure 4.21.

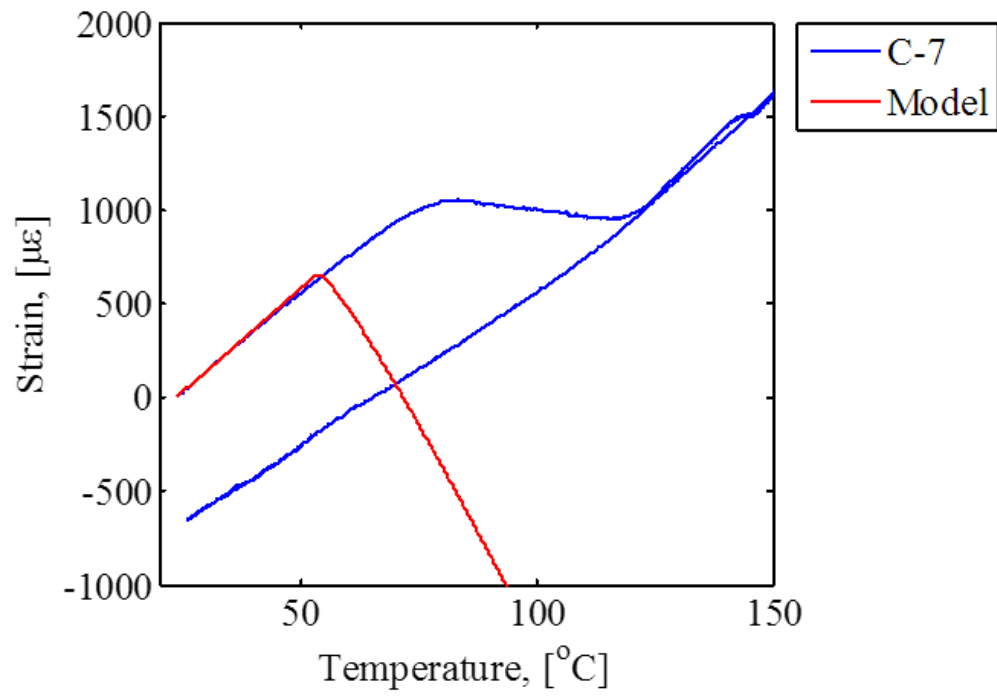


Figure 4.17: Plot of C-7's average strain on its first cycle compared to the SMA composite model results for an Al-NiTi composite of 19.8% NiTi material.

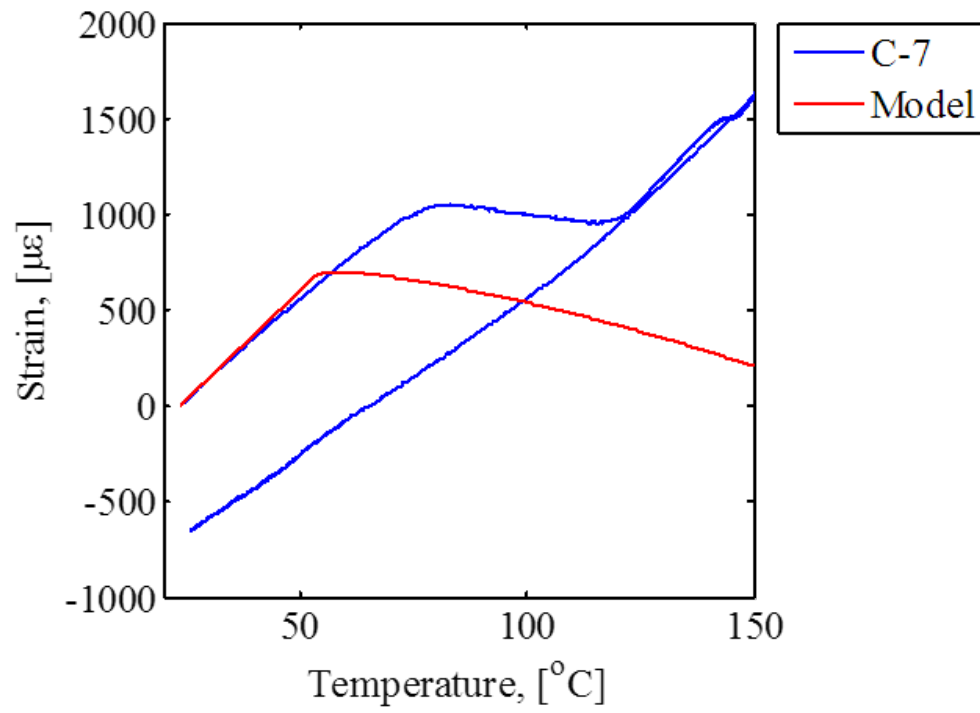


Figure 4.18: Plot of C-7's average strain on its first cycle compared to the SMA composite model results for an Al-NiTi composite of 8.9% NiTi material.

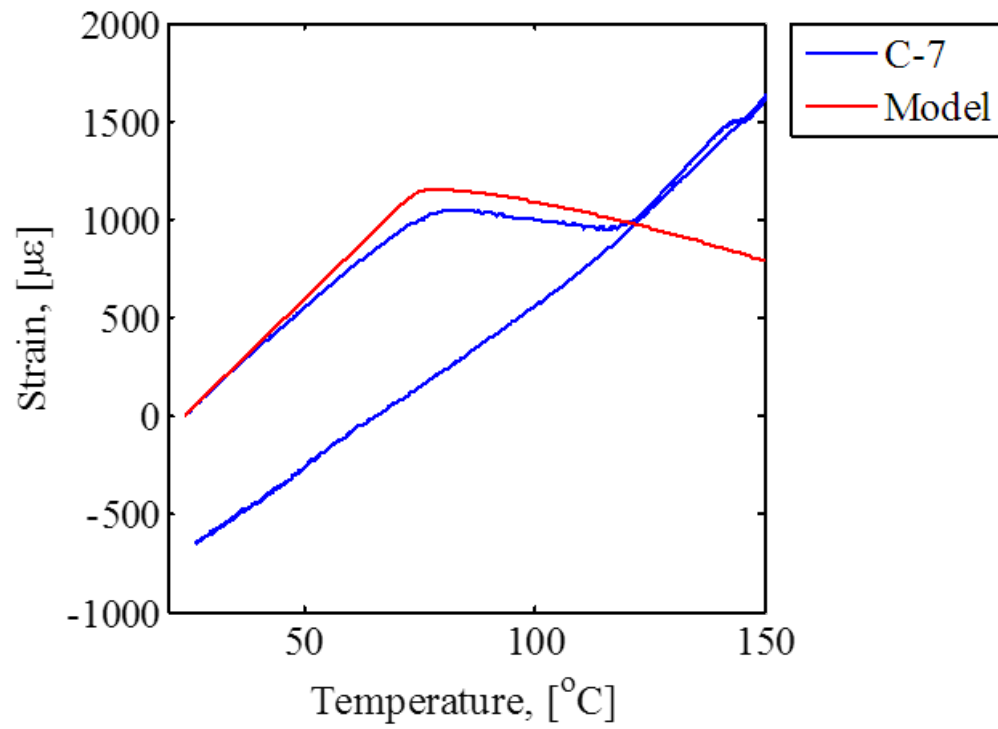


Figure 4.19: Plot of C-7's average strain on its first cycle compared to the SMA composite model results for an Al-NiTi composite of 8.9% NiTi material and the inclusion of an initial stress of 400 MPa.

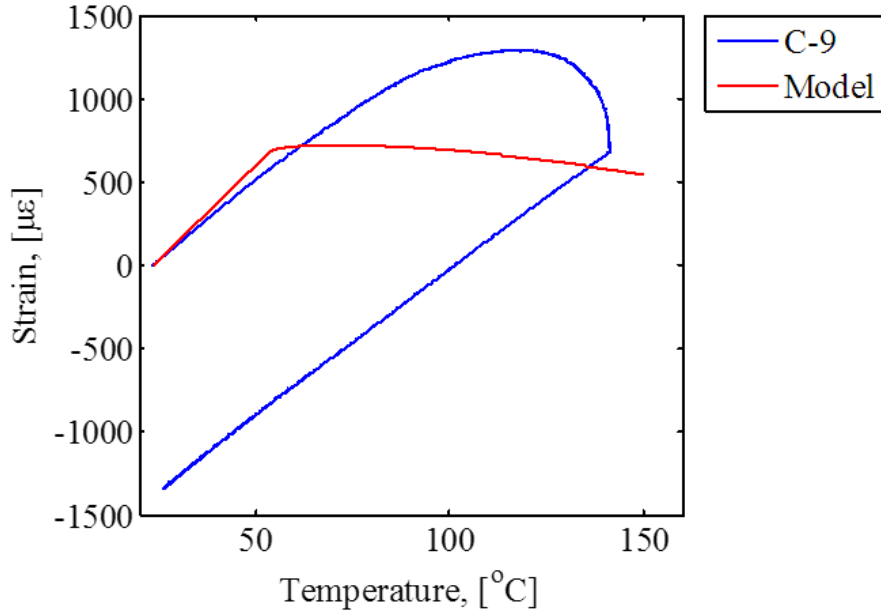


Figure 4.20: Plot of C-9's average strain on its first cycle compared to the SMA composite model results for an Al-NiTi composite of 7.9% NiTi material.

Because the CTE of the composite is higher than the model, the model was adjusted to determine the active NiTi volume fraction within the composite by decreasing the volume fraction of NiTi within the model. The result suggests that the active amount of NiTi material within the composite is approximately 6.4%, Figure 4.22.

Overall, the comparisons between the model and the actual composites show that there typically exists a decrease in the active volume fraction of NiTi material and the geometric volume fraction of NiTi material. In addition, there consistently seems to be an initial stress developed within the NiTi fibers as they are embedded within the composite that forces the austensite start temperature higher in the composite.

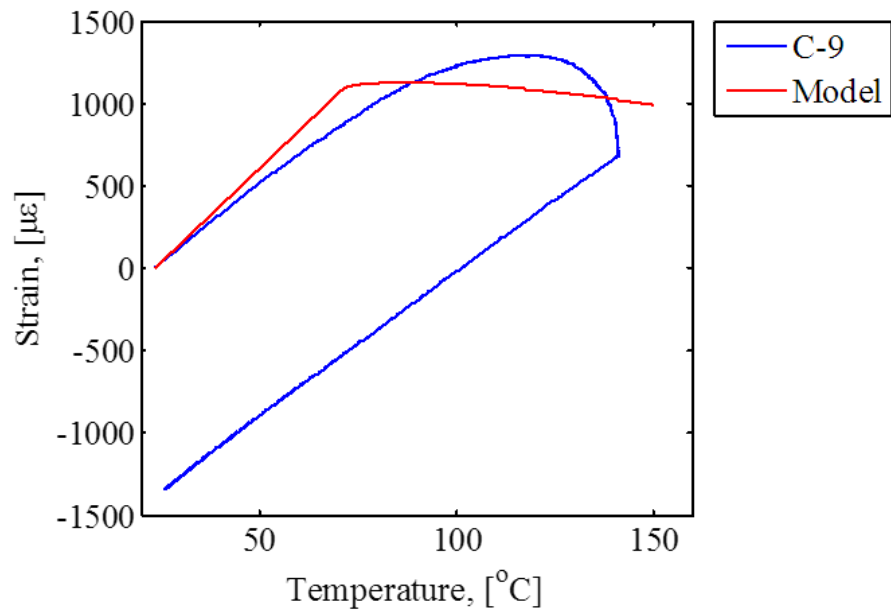


Figure 4.21: Plot of C-9's average strain on its first cycle compared to the SMA composite model results for an Al-NiTi composite of 7.9% NiTi material and the inclusion of an initial stress of 350 MPa.

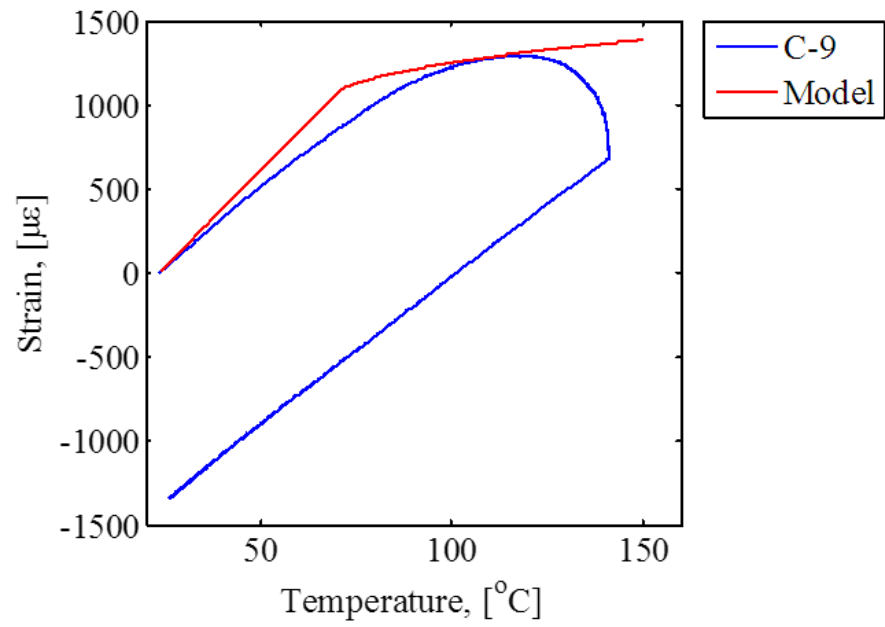


Figure 4.22: Plot of C-9's average strain on its first cycle compared to the SMA composite model results for an Al-NiTi composite of 6.4% NiTi material and the inclusion of an initial stress of 350 MPa.

4.2 Thermal Diffusivity

4.2.1 Test Set-Up and Procedure

Thermal diffusivity is the measurement of how quickly heat is passed through an area of material. Here, the flash method was used to determine the diffusivity of the material [9, 10]. In this method, a sample of known size is excited by a short pulse of energy on one side; on the opposite side the time it takes for a fluctuation in the heat signature to occur and the amplitude of the signature change is recorded, Figure 4.23. For this study, an Anter Flashline-5000 Diffusivity Meter, Figure 4.24, was used (Anter is now owned by TA Instruments). Specifically, the Flashline-5000 uses a high speed xenon discharge tube for producing the energy pulse, while an indium antimonide infrared detector is used to measure the output on the opposite end of the sample. The Flashline-5000 was used to perform tests on UAM 6061-T6 aluminum in all three directions, Figure 4.25, and on a 6061-T6 Al-pseudoelastic NiTi composite in the out-of-plane direction, Figure 4.26.

To carry out the test, each sample was machined to fit into the 7mm x 7mm, molybdenum sample adapter. The machining process first involved milling to get the samples square and to the approximate size. Cutting the samples to size was done by the low-speed, rotary saw, where Figures 4.27 and 4.28 are the UAM aluminum and Al-NiTi composite diffusivity samples, respectively. With the samples cut to size, they were coated with graphite using a spray on application method. One sample was tested at a time. The diffusivity of each sample was measured at seven different temperatures: 75°C, 100°C, 125°C, 150°C, 200°C, 225°C, and 250°C. At each temperature, three pulses were performed to obtain three responses.

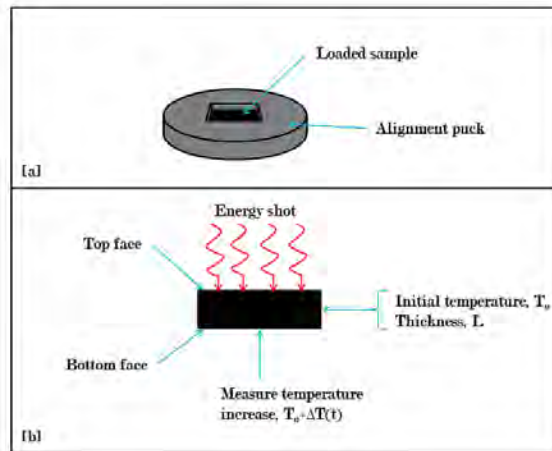


Figure 4.23: Illustration of how the flash method for the determination of thermal diffusivity works.



Figure 4.24: Anter Flashline-5000 Thermal Diffusivity Meter used to perform the thermal diffusivity tests.

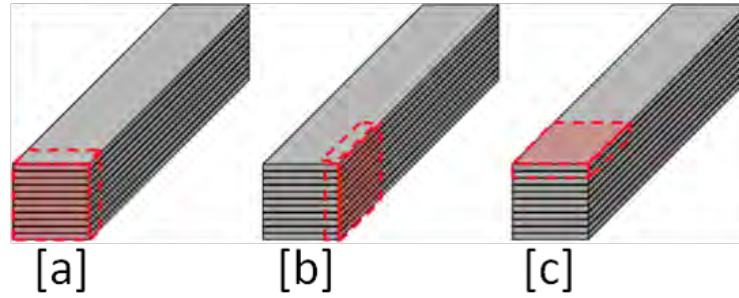


Figure 4.25: Rendering of UAM Al thermal diffusivity samples as cut from a larger UAM Al piece, where a, b, and c are the rolling, transverse, and out-of-plane directions respectively.

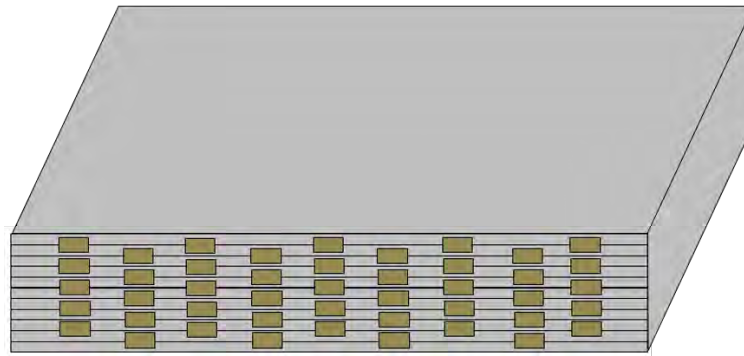


Figure 4.26: Rendering of UAM Al-NiTi thermal diffusivity sample in the out-of-plane direction.

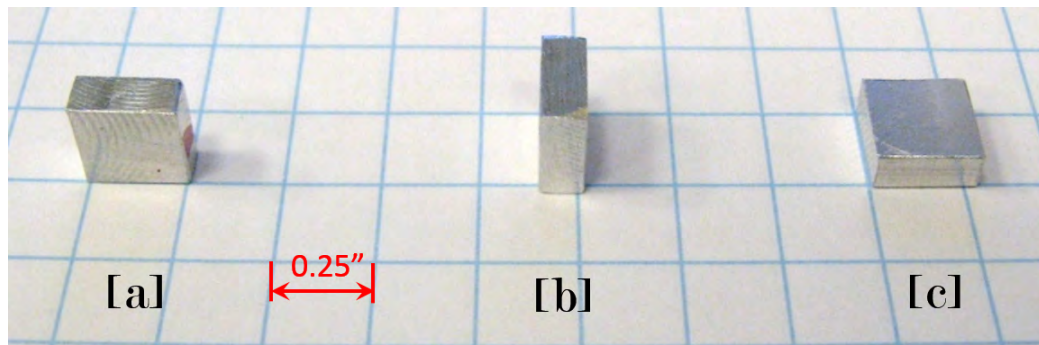


Figure 4.27: UAM 6061-Al samples cut and machined for thermal diffusivity testing- where a, b, and c are the rolling, transverse, and out-of-plane directions respectively.

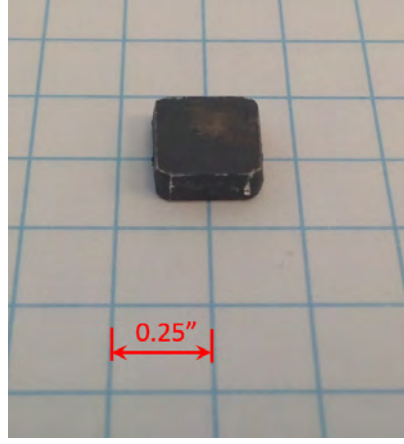


Figure 4.28: UAM Al-NiTi thermal diffusivity sample in the out-of-plane direction.

4.2.2 Results

The results of the thermal diffusivity tests on the UAM aluminum samples, Tables 4.3, 4.4, and 4.5 for the out-of-plane, rolling, and transverse directions, respectively, were supplied directly from the diffusivity meter for all three pulses at each temperature. The three responses were then averaged and compared to the theoretical diffusivity of aluminum, $0.74906 \text{ cm}^2/\text{s}$, which was obtained by:

$$\alpha_{\text{theo}} = \frac{k}{\rho c_p} = \frac{180[\text{W}/\text{m} - \text{K}]}{2.70[\text{g}/\text{cm}^3]0.89[\text{J}/\text{g} - ^\circ \text{C}]}, \quad (4.5)$$

where α , k , ρ , and c_p are the theoretical thermal diffusivity, thermal conductivity, density, and specific heat, respectively. The values for the theoretical thermal diffusivity of aluminum were obtained from matweb.com. Using the metric of percent difference, the out-of-plane UAM aluminum samples varied from the theoretical by 2.3%, while the rolling and transverse directions both varied by 3.4%. The percent differences in the rolling and transverse directions are equivalent, which was expected due to the

structure being isotropic in these directions. Overall, the results provide evidence that there is little difference in the thermal diffusivity of 6061 UAM aluminum and a homogeneous sample of 6061 aluminum.

Table 4.3: Thermal diffusivity results and comparison to the theoretical diffusivity for 6061 UAM aluminum in the out-of-plane direction.

Temp, [°C]	Diffusivity, [cm ² /s]				% Diff. from Theo.
	Shot 1	Shot 2	Shot 3	Avg.	
81	0.7436	0.7474	0.7707	0.7539	0.6
114	0.7514	0.7125	0.7605	0.7415	1.0
140	0.7644	0.7269	0.7318	0.7410	1.1
166	0.7379	0.7333	0.7300	0.7337	2.0
217	0.7373	0.7284	0.7069	0.7242	3.3
243	0.7197	0.7237	0.7237	0.7224	3.6
268	0.7141	0.7150	0.7121	0.7137	4.7
Samp. Dim., [mm]	7.112 x 7.137 x 3.099			Avg. % Diff.	2.3

Table 4.4: Thermal diffusivity results and comparison to the theoretical diffusivity for 6061 UAM aluminum in the rolling direction.

Temp, [°C]	Diffusivity, [cm ² /s]				% Diff. from Theo.
	Shot 1	Shot 2	Shot 3	Avg.	
81	0.7640	0.8000	0.7533	0.7724	3.1
115	0.7685	0.7768	0.7768	0.7740	3.3
140	0.7703	0.7486	0.7205	0.7465	0.3
166	0.7231	0.7237	0.7381	0.7283	2.8
217	0.7210	0.7262	0.7144	0.7205	3.8
243	0.7110	0.7085	0.7086	0.7094	5.3
269	0.7179	0.7065	0.7059	0.7101	5.2
Samp. Dim., [mm]	7.214 x 7.214 x 3.019			Avg. % Diff.	3.4

Table 4.5: Thermal diffusivity results and comparison to the theoretical diffusivity for 6061 UAM aluminum in the transverse direction.

Temp, [°C]	Diffusivity, [cm ² /s]				% Diff. from Theo.
	Shot 1	Shot 2	Shot 3	Avg.	
76	0.8028	0.8431	0.7635	0.8031	7.2
110	0.7891	0.7605	0.7885	0.7794	4.0
136	0.7366	0.7456	0.7584	0.7469	0.3
162	0.7057	0.7071	0.7363	0.7164	4.4
213	0.7388	0.7447	0.7363	0.7164	0.8
239	0.7226	0.7300	0.7259	0.7262	3.1
265	0.7288	0.7179	0.7186	0.7218	3.6
Samp. Dim., [mm]	7.061 x 6.985 x 3.052			Avg. % Diff.	3.4

The results of the thermal diffusivity test on the Al-pseudoelastic NiTi composite, Table 4.6, provide an overall average diffusivity value of 0.0449 cm²/s. Comparing this result to the theoretical values for NiTi and aluminum, 0.048 cm²/s and 0.74906 cm²/s respectively, the composite is 6.5% different than the theoretical value of the NiTi's diffusivity. The results therefore show that the composite's thermal diffusivity in the out-of-plane direction is highly dependent upon the NiTi material. This dependence is a resultant of the NiTi fibers encompassing 41.7% of the area in the direction of the heat flow as shown by

$$P_{\text{area,NiTi}} = \frac{n_f w_f}{w_{\text{comp}}} \times 100 = \frac{9(.014)}{.302} \times 100 = 41.7\%, \quad (4.6)$$

where $P_{\text{area,NiTi}}$, n_f , w_f , and w_{comp} are the area percentage of NiTi material, number of NiTi fibers within area, cross-sectional width of the NiTi fibers, and the cross-sectional width of the composite.

Table 4.6: Thermal diffusivity results for an Al-pseudoelastic NiTi composite with 14.0% austenitic NiTi material.

Temp, [°C]	Diffusivity, [cm ² /s]			
	Shot 1	Shot 2	Shot 3	Avg
73	0.0399	0.0419	0.0364	0.0394
108	0.0429	0.0415	0.465	0.0436
133	0.0451	0.0403	0.0433	0.0429
159	0.0421	0.0441	0.0424	0.0429
210	0.0512	0.0501	0.0532	0.0515
236	0.0542	0.0518	0.0493	0.0518
261	0.0426	0.0393	0.0438	0.0419
Samp. Dim., [mm]	7.671 x 7.671 x 2.642			

4.3 Electrical Resistivity

4.3.1 Test Set-Up and Procedure

The electrical resistivity was also an area of testing within this study. To determine the electrical resistivity, the four-probe method was used. To perform this method, a long sample of known length, width, and thickness is connected with four leads, two on each end. The two outermost leads are connected to a current source, while the inner leads are connected to a voltmeter. In this test, a Keithley 6221 AC and DC Current Source and a 2182A Digital Nanovoltmeter were used to perform the tests. Five measurements were taken at each of 11 different supplied currents. The measurements were recorded using LabView. Using the four-probe test method, the electrical resistivities of 3003-H18 aluminum, UAM 3003-H18 aluminum in the out-of-plane direction, and composite P-2 in the rolling direction were measured.

4.3.2 Results

The results of the measurements for the three samples were analyzed using MATLAB to first determine the resistance of each. The resistance was solved for by fitting a line to the voltage versus current data, where the slope of the fitted line was the resistance for each sample in accordance with Ohm's Law, Figures 4.29, 4.30, and 4.31. From the resistance, the resistivity was calculated through use of

$$\rho = \frac{Rwt}{l}, \quad (4.7)$$

where ρ is the resistivity, R is the resistance, and w , t , and l are the width, thickness, and length of the sample, respectively, Table 4.7. Because the electrical resistivity is the inverse of electrical conductivity, the results of the resistivity tests indicate the tested materials would all have electrical conductivity values on the order of $10\text{e6 } \Omega^{-1} \cdot \text{m}^{-1}$.

Table 4.7: Resistivity results for 3003-H18 aluminum tape, UAM 3003-H18 aluminum in out-of-plane direction, and composite P-2 in rolling direction.

Sample	Resistance, [Ω]	Dimensions, [mm]			Resistivity, [n Ω ·m]
		Width	Thickness	Length	
3003-H18 Al (Tape)	5.94e-4	23.93	0.15	60.27	35.91
3003-H18 Al (Out-of-Plane)	1.35e-5	9.68	9.52	24.25	51.17
P-2	5.58e-4	4.95	0.76	42.57	49.41

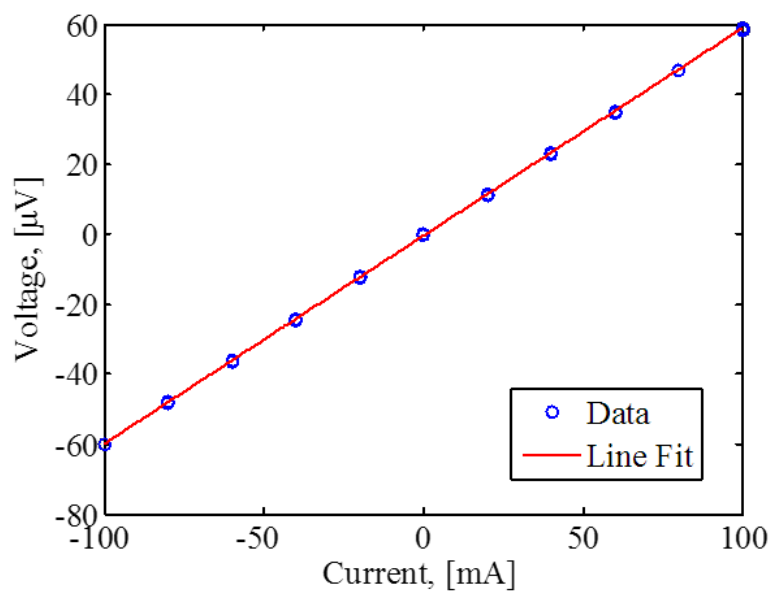


Figure 4.29: Voltage versus current and fitted curve for 3003-H18 Al tape.

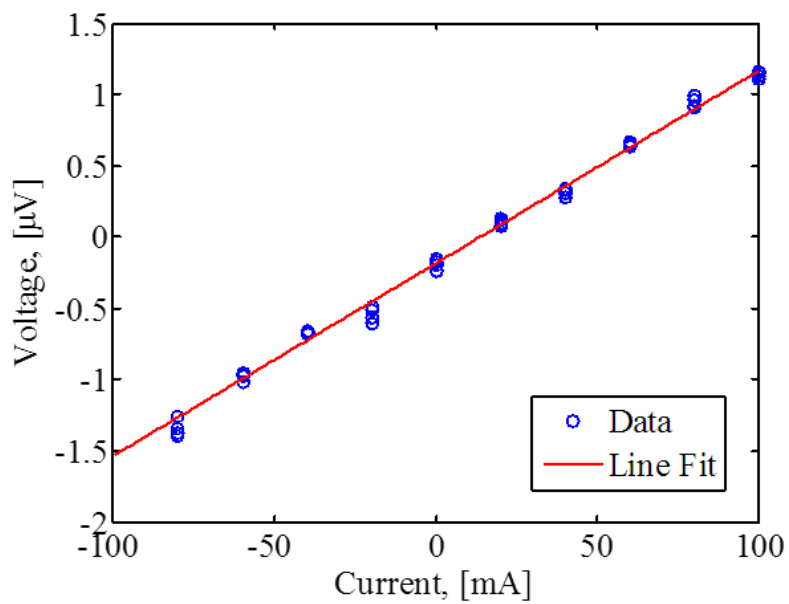


Figure 4.30: Voltage versus current and fitted curve for UAM 3003-H18 Al in the out-of-plane direction.

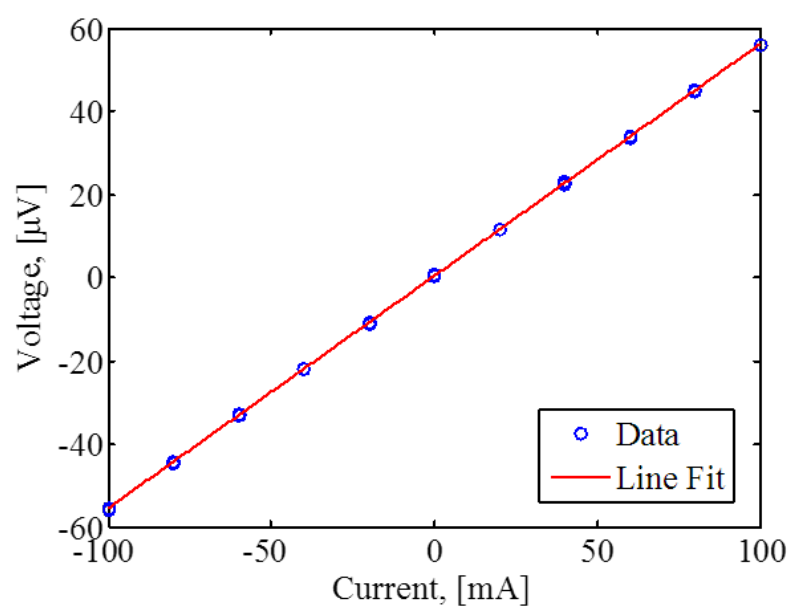


Figure 4.31: Voltage versus current and fitted curve for Al-NiTi composite P-2.

CHAPTER 5

CONCLUSION

5.1 Summary of Work

Within this study several accomplishments were made in the development of composites, specifically multi-layer MMCs with SMA fibers fabricated via UAM. This work demonstrated that these composites can be designed through the use of an analytical SMA composite model developed by Hahnlen. Through use of this model, the performance of a produced MMC with SMA fibers can be predicted before the manufacturing of said composite through the application of basic property values for both the matrix material and the fibers to be embedded. The properties of the fibers within this work, pseudoelastic NiTi and shape memory NiTi material, were obtained through isothermal tensile tests and differential scanning calorimetry tests. By obtaining the performance results from the model, the geometric cross-section for the MMC could be produced.

Knowing the cross-sectional dimensions for the composite aided in developing a detailed process for fabricating both the pseudoelastic NiTi and the shape memory NiTi composites. The methods for producing of the Al-NiTi composites in this work began with the designing and machining of two custom base plates as well as two

ribbon transfer fixtures with detachable ribbon clamps. Through the utilization of these plates, fixtures, clamps, and the addition of the UAM's CNC milling system, the MMC manufacturing process with the OSU UAM system is more repeatable and streamlined. Using these new production methods, the state-of-the-art of UAM MMCs was expanded to include multi-layer composites in both a small coupon sample form and a larger form capable of spanning distances up to 27.18 cm (10.7"). At times however, welding defects still remained a factor in the production of the larger builds.

Testing was conducted on the coupon sized composites developed in this work to determine the coefficient of thermal expansion, thermal diffusivity, and electrical resistivity. The CTE testing procedures were performed on both the Al-NiTi composites containing pseudoelastic NiTi ribbons and those containing the shape memory NiTi ribbons. The CTE tests resulted in transformation of only one composite manufactured with pseudoelastic NiTi fibers, P-2. DSC testing of these composites provided evidence that the prestress within the embedded material was recovered before CTE testing commenced, as both the samples of the embedded pseudoelastic NiTi and free pseudoelastic NiTi material transformed to austenite between -20°C and 20°C. CTE testing of the Al-shape memory NiTi composites provided measurements of decreased CTE for two different composites within their first cycle, with values of $9.6 \times 10^{-2} \mu\epsilon/^\circ\text{C}$ and $6.1 \mu\epsilon/^\circ\text{C}$ for composites C-7 and C-9, respectively. Micrographs of C-7's and C-9's cross-sections were taken to determine the cause of failure after the first cycle. The results of the cross-sections indicate that milling defects and cracks aided in the failure of C-7 after the first cycle, while partial failure of the fiber-matrix interface led to the inability of C-9 to perform as desired after the heating portion of the first cycle.

Thermal diffusivity measurements were conducted on 6061 UAM aluminum in the out-of-plane, rolling, and transverse directions using the flash method through the use of an Anter Flashline-5000 Thermal Diffusivity Meter. The outcomes of the tests were that the UAM aluminum’s thermal diffusivity did not vary by more than 3.4 percent difference from the theoretical thermal diffusivity of 6061 aluminum, $0.74906 \text{ cm}^2/\text{s}$. In addition to the thermal diffusivity tests being conducted on the 6061 UAM Al, the tests were also conducted on a sample of Al-NiTi composite in the out-of-plane direction. The Al-NiTi composite yielded an average diffusivity value of $0.0449 \text{ cm}^2/\text{s}$ for a cross-section that was approximately 41.7% NiTi by area.

Finally, electrical resistivity tests were performed on 3003-H18 Al tape, UAM 3003-H18 Al in the out-of-plane direction, and P-2 in the rolling direction. The resistivity tests were carried out using the four probe method and resulted in resistivity values of $35.91 \text{ n}\Omega\cdot\text{m}$, $51.17 \text{ n}\Omega\cdot\text{m}$, and $49.41 \text{ n}\Omega\cdot\text{m}$ for the 3003-H18 Al tape, UAM 3003-H18 Al in the out-of-plane direction, and P-2 in the rolling direction respectively.

5.2 Future Work

Following this study, some additional work can still be accomplished in the area of multi-layer, thermally-invariant, MMCs produced via UAM. Specifically, further research can be conducted in the following areas:

- Modeling
 - Expansion of the modeling capabilities from a numerical model to a FEA model. Through the expansion of the model to an FEA platform, understanding of how both the thermal and mechanical stresses and strains

propagate through the composite would aid in part fabrication and eventually structures.

- Manufacturing

- This study has shown that it is possible to create multilayer MMCs, but defects, such as cracks and mis-welds are still encountered in this process. Work to resolve these defects would be vital to not only improving MMCs, but any components fabricated via UAM. Additional study of the geometries of the composites to mitigate these defects would also be vital to enhanced performance and reliability of the composites.
- Development into automating the detwinning and embedding process of the fibers would aid in the fabrication process, as well as reduce any errors associated with the current manual process. This would also help commercialization of MMCs fabricated via UAM.

- Testing

- Continued testing to determine the thermal diffusivity of Al-UAM composites in the rolling and transverse directions. By continuing to study the thermal diffusivity, three-dimensional models may be developed to help better predict the performance of these composites. If better models are developed in the various directions, then fabrication of advanced structures will become possible.

- Previous studies in the area of MMCs with SMA fibers included dynamic testing of single-layer composites. Continuation of these tests on multi-layer composites would help to broaden the understanding of how these composites perform in dynamic conditions.
- Test ways to mitigate the addition of a prestress in the consolidated material to ensure the ability to manufacture components that perform according to the design based on the composite model.

BIBLIOGRAPHY

- [1] Ferdinando Auricchio and Robert L. Taylor. Shape-memory alloys: modelling and numerical simulations of the finite-strain superelastic behavior. *Computer Methods in Applied Mechanics and Engineering*, 143(12):175–194, 1997.
- [2] David E. Bowles and Stephen S. Tompkins. Prediction of coefficients of thermal expansion for unidirectional composites. *Journal of Composite Materials*, 23:370–388, 1989.
- [3] L. C. Brinson. One-dimensional constitutive behavior of shape memory alloys: Thermomechanical derivation with non-constant material functions and redefined martensite internal variable. *Journal of Intelligent Material Systems and Structures*, 4:229–242, 1993.
- [4] Sheng Dong and Marcelo J Dapino. Piezoelectrically-induced ultrasonic lubrication by way of poisson effect. In *SPIE Smart Structures and Materials+ Nondestructive Evaluation and Health Monitoring*, pages 83430L–83430L. International Society for Optics and Photonics, 2012.
- [5] Yasubumi Furuya, Atsuchi Sasaki, and Minoru Taya. Enhanced mechanical properties of tiny shape memory fiber / al matrix composite. *Materials Transactions, JIM*, 32(3):224–227, 1993.
- [6] R. Hahnlen. *Characterization and Modeling of Active Metal-matrix Composites with Embedded Shape Memory Alloys*. PhD thesis, The Ohio State University, Columbus, OH, 2012.
- [7] Ryan Hahnlen and Marcelo J. Dapino. Thermomechanic behavior of low cte metal-matrix composites fabricated through ultrasonic additive manufacturing. In *Proceedings of the ASME 2012 Conference on Smart Materials, Adaptive Structures and Intelligent Systems*, 2012.
- [8] ASTM International. F2516, standard test method for tension testing of nickel-titanium superelastic materials. *Annual Book of ASTM Standards*, 2007.

- [9] ASTM International. E2585, standard practice for thermal diffusivity by the flash method . *Annual Book of ASTM Standards*, 2009.
- [10] ASTM International. E1461, standard test method for thermal diffusivity by the flash method . *Annual Book of ASTM Standards*, 2013.
- [11] S. Jin and H. Mavoori. Low-thermal-expansion copper composites via negative cte metallic elements. *JOM*, 50(6):70–72, 1998.
- [12] CY Kong and RC Soar. Fabrication of metal–matrix composites and adaptive composites using ultrasonic consolidation process. *Materials Science and Engineering: A*, 412(1):12–18, 2005.
- [13] CY Kong, RC Soar, and PM Dickens. Ultrasonic consolidation for embedding sma fibres within aluminium matrices. *Composite Structures*, 66(1):421–427, 2004.
- [14] C. Liang and C.A. Rogers. One-deminsional thermomechanical constitutive relations for shape memory materials. *Journal of Intelligent Material Systems and Structures*, 1:207–234.
- [15] FL Matthews and RD Rawlings. *Composite materials: engineering and science*. Chapman & Hall, London, 1994.
- [16] Mel M. Schwartz. *Composite Materials Properties, Nondestructive Testing, and Repair*, volume 1. Prentice Hall, Inc., 1st edition, 1997.
- [17] John A. Shaw. Simulations of localized thermo-mechanical behavior in a niti shape memory alloy. *International Journal of Plasticity*, 16:541–562, 2000.
- [18] P. Sittner, R. Stalmans, and M. Tokuda. An algorithm for prediction of the hysteretic responses of shape memory alloys. *Smart Material Structures*, 9:452–465, 2000.
- [19] American Welding Society. *AWS Welding Handbook*, volume 9. American Welding Society, 9th edition, 2001.
- [20] M.R. Sriraman, S.S. Babu, and M. Short. Bonding characteristics during very high power ultrasonic additive manufacturing of copper. *Scripta Materialia*, 62:560–563, 2010.
- [21] Koshi Takenaka. Negative thermal expansion materials: Technological key for control of thermal expansion. *Science and Technology of Advanced Materials*, 13, 2012.

- [22] K. Tanaka and R. Iwasaki. A phenomenological theory of transformation superplasticity. *Engineering Fracture Mechanics*, 21(4):709 – 720, 1985.
- [23] K Tanaka and S Nagaki. A thermomechanical description of materials with internal variables in the process of phase transitions. *Ingenieur-Archiv*, 51(5):287–299, 1982.
- [24] Kikuaki Tanaka, Shigenori Kobayashi, and Yoshio Sato. Thermomechanics of transformation pseudoelasticity and shape memory effect in alloys. *International Journal of Plasticity*, 2(1):59 – 72, 1986.
- [25] Minoru Taya. Strengthening mechanisms of metal matrix composite. *Material Transactions, JIM*, 32:1–19, 1991.
- [26] Vishay Precision Group. Gage series - stress analysis gages: Technical data. Website: <http://www.vishaypg.com/docs/11506/gageser.pdf>, 2010.
- [27] Vishay Precision Group. General purpose strain gages - linear pattern. Website: <http://www.vishaypg.com/docs/11071/031cf.pdf>, 2010.
- [28] Vishay Precision Group. Precision strain gages. Website: <http://www.vishaypg.com/docs/50003/precsg.pdf>, 2010.
- [29] Vishay Precision Group. Tech note tn-153-1: Measurement of thermal expansion coefficient using strain gages. Website: <http://www.vishaypg.com/docs/11063/tn5131tn.pdf>, 2010.
- [30] Karthik Guda Vishnu and Alejandro Strachan. Phase stability and transformations in niti from density functional theory calculations. *Acta Materialia*, 58:745–752, 2010.
- [31] D. White. Ultrasonic object consolidation, 02 2003.
- [32] Paul J. Wolcott. Toward load bearing reconfigurable radio frequency antenna devices using ultrasonic additive manufacturing. Master’s thesis, The Ohio State University, Columbus, OH, 2012.

APPENDIX A

CHARACTERIZATION OF NITI MATERIAL

The NiTi materials within this study underwent a characterization process in order to determine the material parameters that fed into the Al-NiTi performance model. Without knowledge of these parameters, accurate design and construction of the composites would not have been possible. Isothermal tensile tests and differential scanning calorimetry tests were the two tests used to conduct the characterization of both the pseudoelastic and shape memory NiTi ribbons.

A.1 Isothermal Tensile Tests

Isothermal tensile tests for this study were carried out using a 2224 N (500lbf) table top load frame, Figure 3.7. The load frame was equipped with an environmental chamber that had both heating and cooling capabilities. An initial sample of the material to be characterized was loaded into the load frame, with approximately 150 mm (5.90") between the grips in accordance with ASTM F 2516-07 [8]. Following the procedure outline in this standard, the ribbon was first loaded until failure to ensure the characterization tests did not involve loads too great for the material to recover. The strain rates for the tests were determined by calculating an effective diameter for the ribbons based on their cross-sectional area through the use of,

$$D_{\text{eff}} = \sqrt{\frac{4A_f}{\pi}}, \quad (\text{A.1})$$

where D_{eff} and A_f are the effective diameter and fiber area, respectively. Using the calculated effective diameter in conjunction with Table 1 of the standard, the strain rate could be determined.

Following the test to failure, another sample of ribbon was secured in the load frame with the same grip spacing as was used on the failure test. Again, this sample was loaded in tension, but only to a load just above the transformation load, as determined by the failure test results, and was then unloaded. This cycle was performed a minimum of three times at each temperature considered. These tensile tests were performed at multiple temperatures between -100°C and 110°C, with a minimum number of temperatures being four. The results of these tests provided stress versus strain curves for the NiTi material at each of the tested temperatures, Figure A.1.

A.2 Differential Scanning Calorimetry

Differential scanning calorimetry tests were conducted on both the pseudoelastic NiTi and the shape memory NiTi in their free stress states. For the tests, sections of each of the ribbons were cut down to fit into the aluminum measurement pans. The amount of material within each pan was over 10 mg to ensure accurate measurements using the TA Instruments 2920 Differential Scanning Calorimeter. For each sample, the sample pan was measured in reference to an empty aluminum pan. Each sample was tested with liquid nitrogen cooling and nitrogen purge gas, as was done for the sample testing in Chapter 4. The temperature profile for which the tests were conducted started below -100°C and went to 150°C at a rate of 5°C per minute.

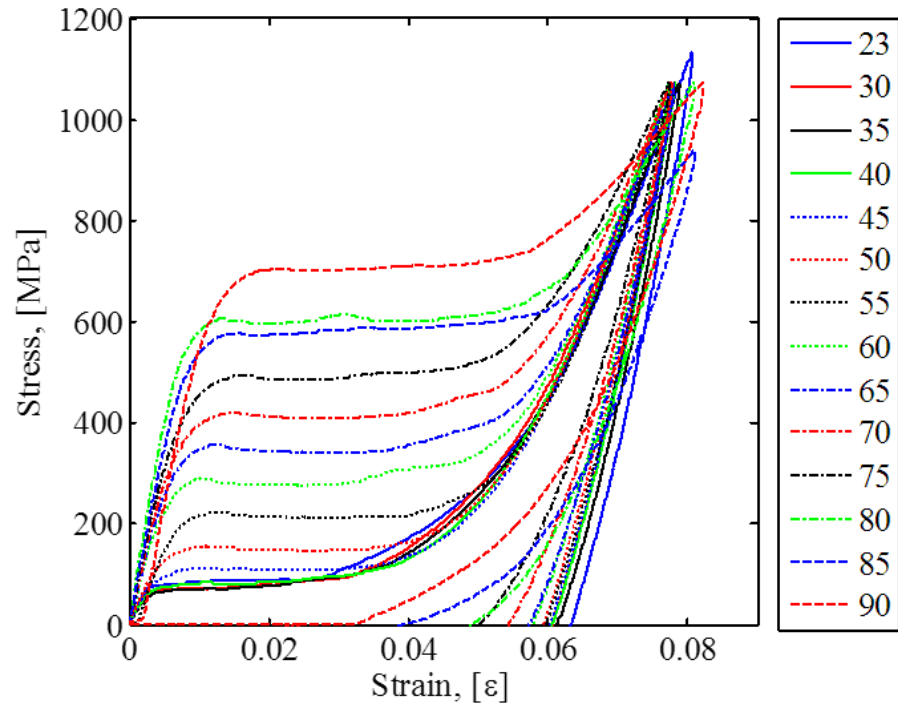


Figure A.1: Example of stress versus strain as a result of data analysis from a isothermal tensile tests at various temperatures. Result of SMA material is shown.

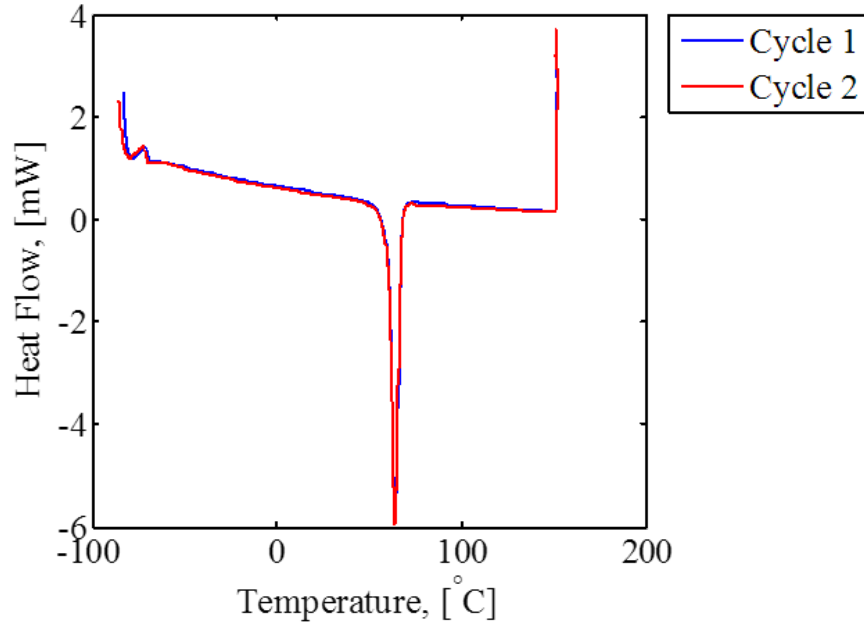


Figure A.2: Example of heat flow per mass versus temperature plot as the result of differential scanning calorimetry tests. SMA material is shown.

The results of these tests provided data curves for the heat flow per mass versus temperature, Figure A.2.

A.3 Phase Diagram Development

The results of both the isothermal tensile tests and the DSC tests were used to create a phase diagram for each of the NiTi materials used in this study. Using the results of the isothermal tensile tests, regression analysis was performed over each region of the data results, which included: initial loading, transformation to detwinned martensite, loading of detwinned martensite, and unloading of detwinned martensite. If the material was being tested was above the austenite finish temperature, regression analysis was performed on two additional regions, transformation to

austenite and unloading of austenite. These last two regions were not well defined for the shape memory material above A_f , as the material failed to recover the majority of the strain necessary to transform the material to detwinned martensite. Despite this issue, points were still obtained for the stresses associated with A_s for the 85° and 90° isothermal tensile tests.

The results of the regression analysis were then plotted on the corresponding stress versus strain curves, Figure A.3. The intersection of these regression lines at the various transformation points, Figure A.4, were then determined and plotted on a stress versus temperature plot, where the temperature component of the coordinates corresponded to the temperature at which the isothermal tensile test was conducted. With all the data points for each of the transformations on the stress versus temperature plot, regression analysis was used on each of the data sets, Figure A.5. The result of the linear regression provided the stress influence coefficients, C_M and C_A , for both the martensite and austenite lines, respectively. Additional averaging of two coefficients was done if the linear regression resulted in two unique values for the start and finish transformation lines. If isothermal tensile tests were performed below the martensite finish temperature, two additional lines for the critical starting and finishing stresses were determined, Figure A.6. Because the slope of these lines are zero, only the y-intersect values were utilized from the regression analysis.

With the stress influence coefficients determined, the results of the DSC tests were analyzed to determine the transformation temperatures at zero stress. To carry out this analysis, linear regression was performed over four different regions: the initial heating, start of transformation, end of transformation, and continuation of heating. As with the isothermal tensile tests, these lines were then plotted with the test data.

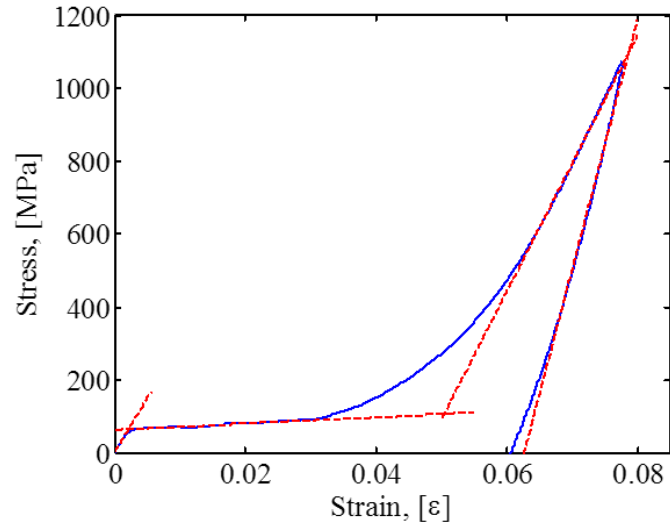


Figure A.3: Example of stress versus strain plot after regression analysis conducted on the various regions of the curve. SMA material at 30°C cycle temperature shown.

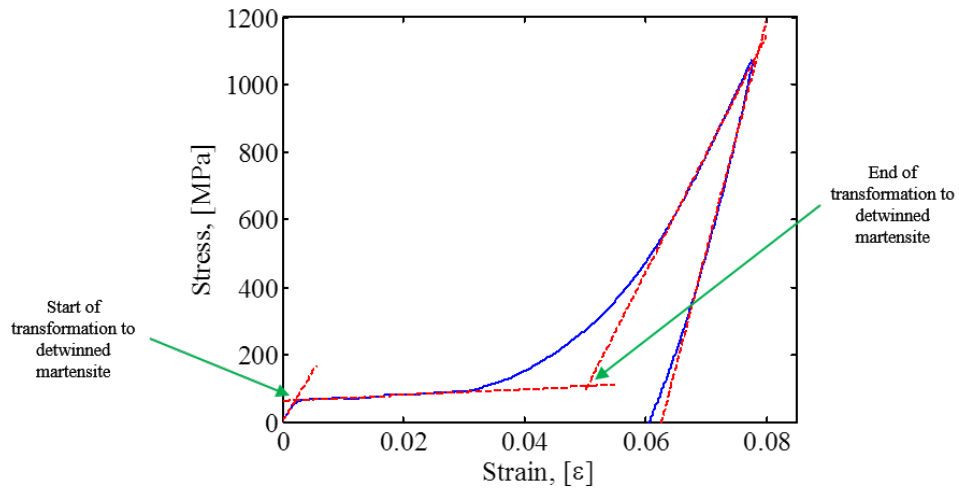


Figure A.4: Example of transformation points gathered from the intersection of regression lines on a stress versus strain plot. SMA material at 30°C cycle temperature shown.

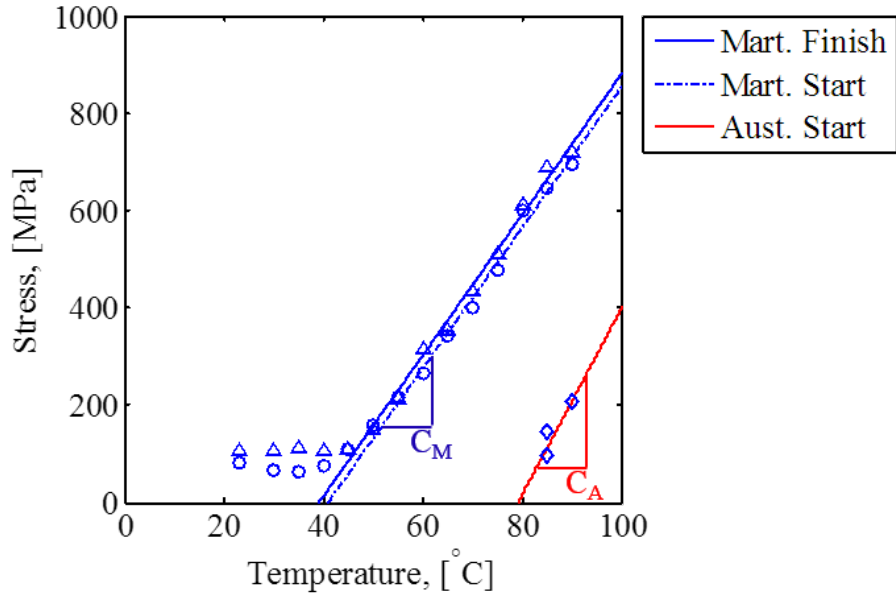


Figure A.5: Example of the determination of the stress influence coefficients from the stress versus temperature plot produced using the collected transformation data of the isothermal tensile tests. SMA material is shown.

The intersection of these lines then provided the transformation temperatures at zero stress, Figure A.7. To produce the phase diagrams, the results of the isothermal tensile tests were then combined with the results of the DSC tests, so that the lines for the transformations were plotted using the stress influence coefficient values while intersecting the temperature axis at the zero stress transformation temperatures. By performing this process twice, once for the pseudoelastic NiTi material and again for the shape memory NiTi material, two phase diagrams were developed, Figures A.8 and A.9. However, because of the low transformation temperatures of pseudoelastic NiTi material, the critical starting and finishing stresses were unable to be determined.

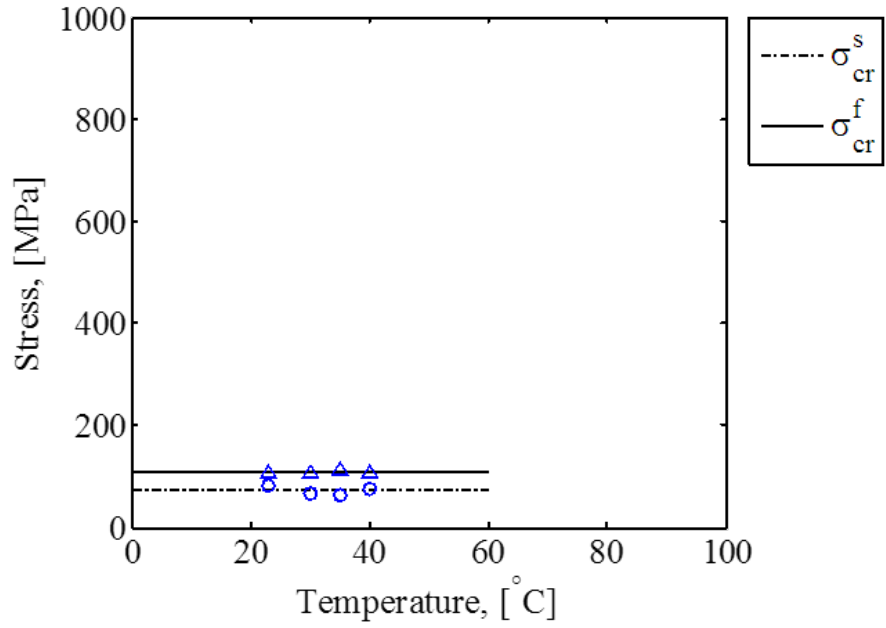


Figure A.6: Example of the determination of the critical starting and finishing stresses from the stress versus temperature plot produced using the collected transformation data of the isothermal tensile tests. SMA material is shown.

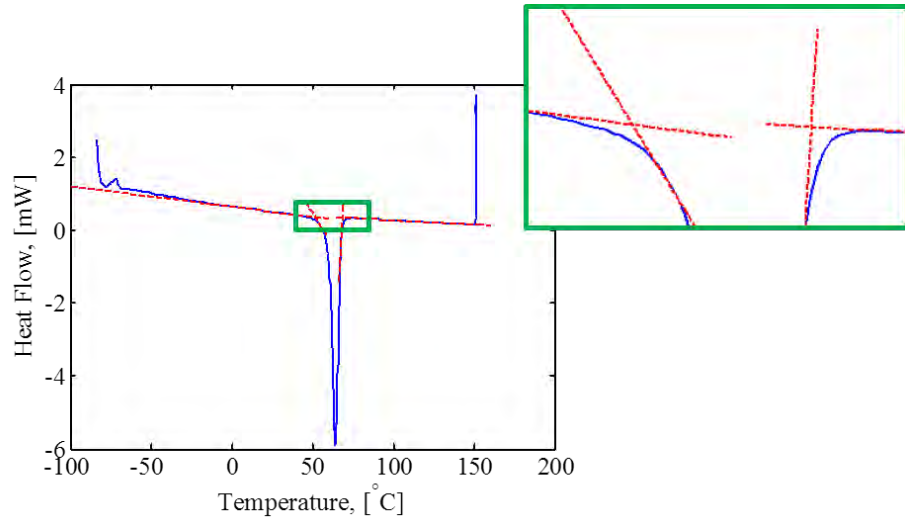


Figure A.7: Example of using regression analysis to determine the transformation temperatures of NiTi material at zero stress. SMA material is shown.

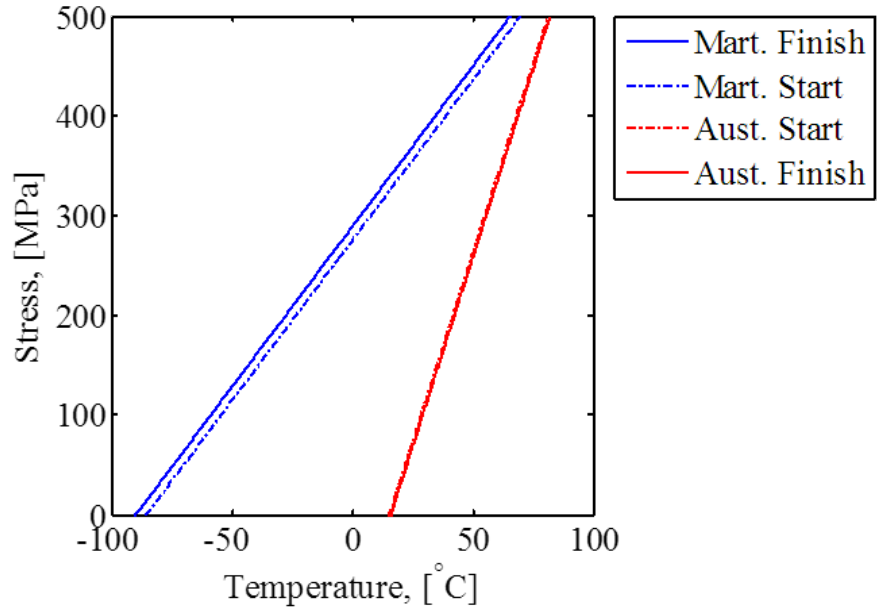


Figure A.8: Pseudoelastic NiTi material phase diagram produced via the characterization process outlined in Appendix A.

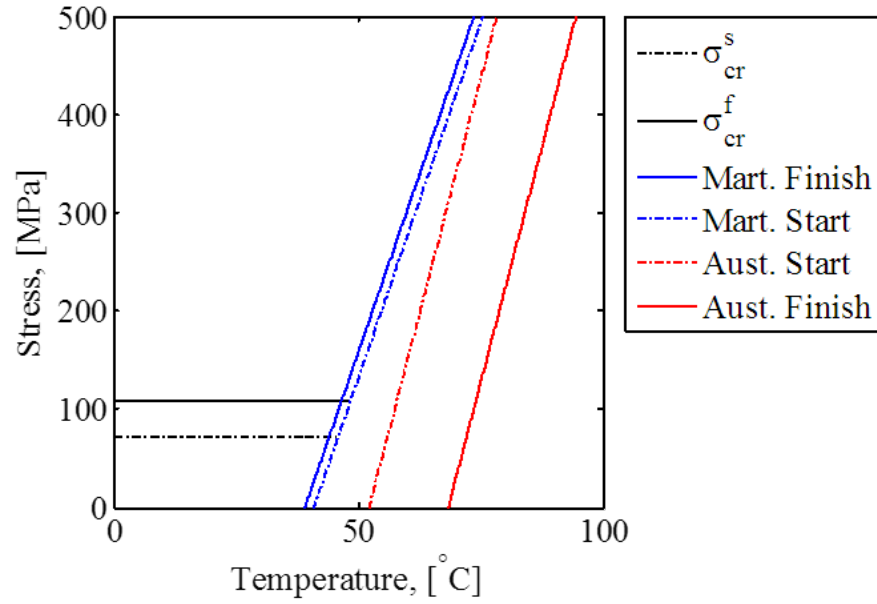


Figure A.9: Shape memory NiTi material phase diagram produced via the characterization process outlined in Appendix A.

APPENDIX B

MECHANICAL DRAWINGS OF PARTS AND FIXTURES

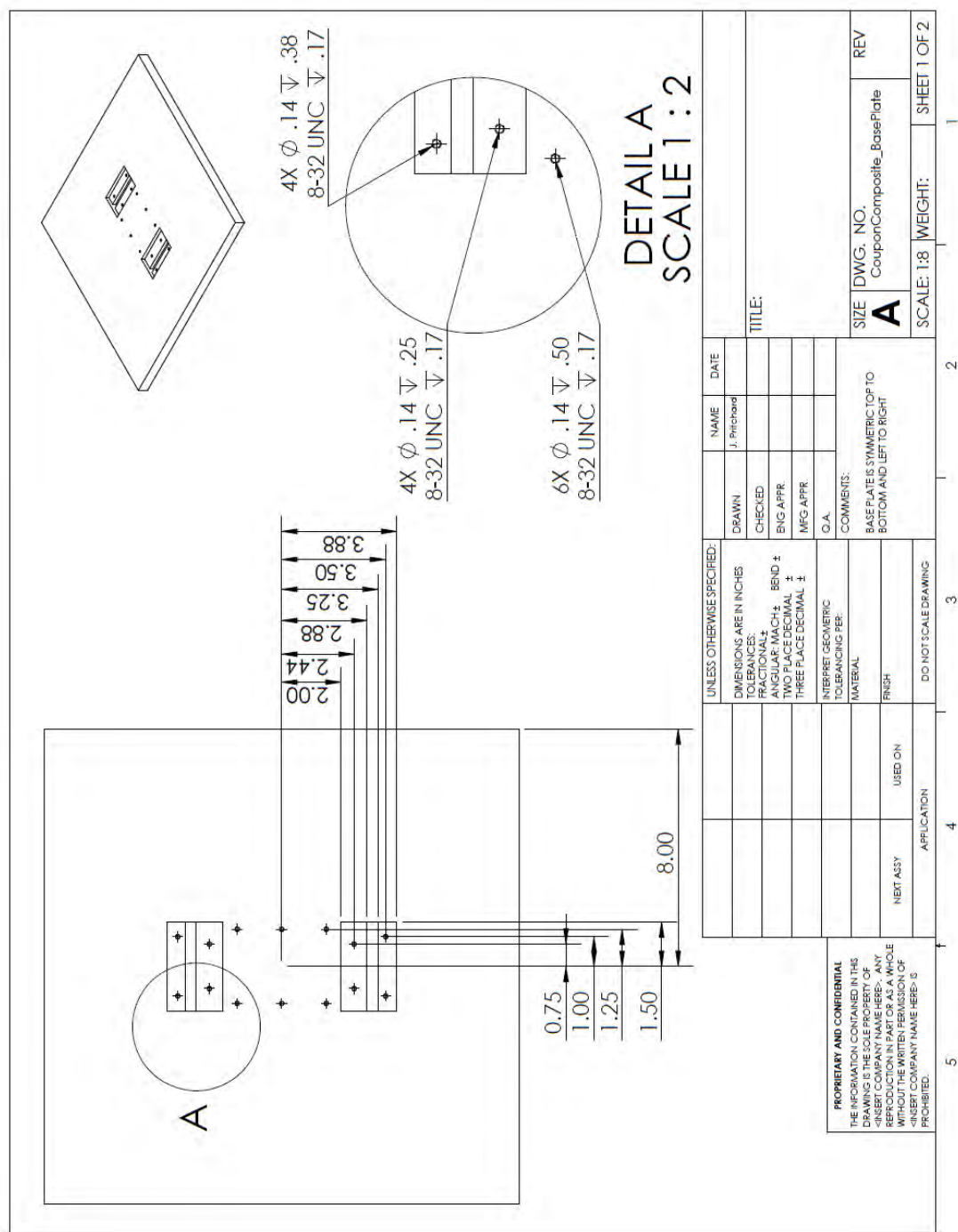


Figure B.1: Dimensional drawing of base plate for producing coupon samples. Sheet 1 of 2.

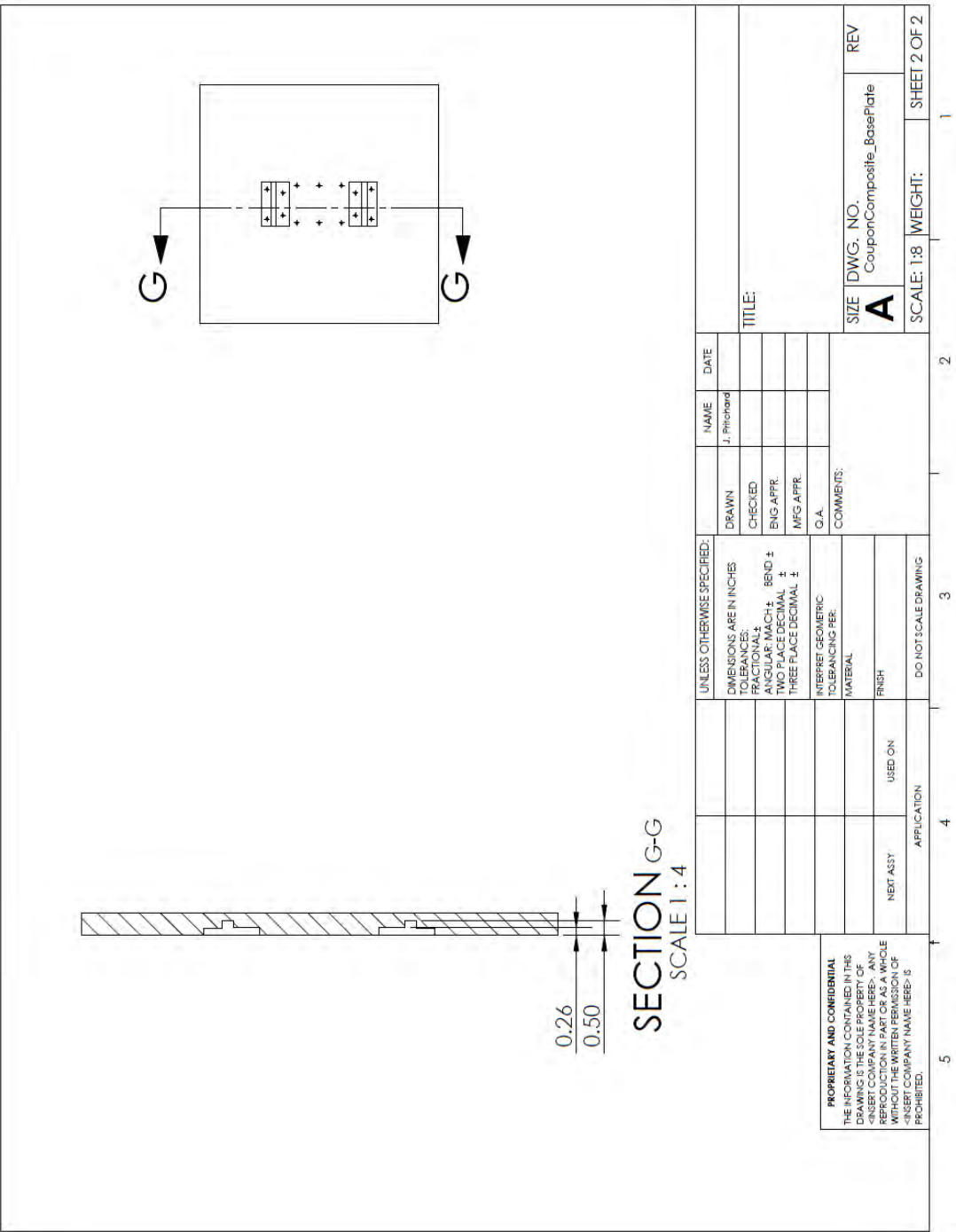


Figure B.2: Dimensional drawing of base plate for producing coupon samples. Sheet 2 of 2.

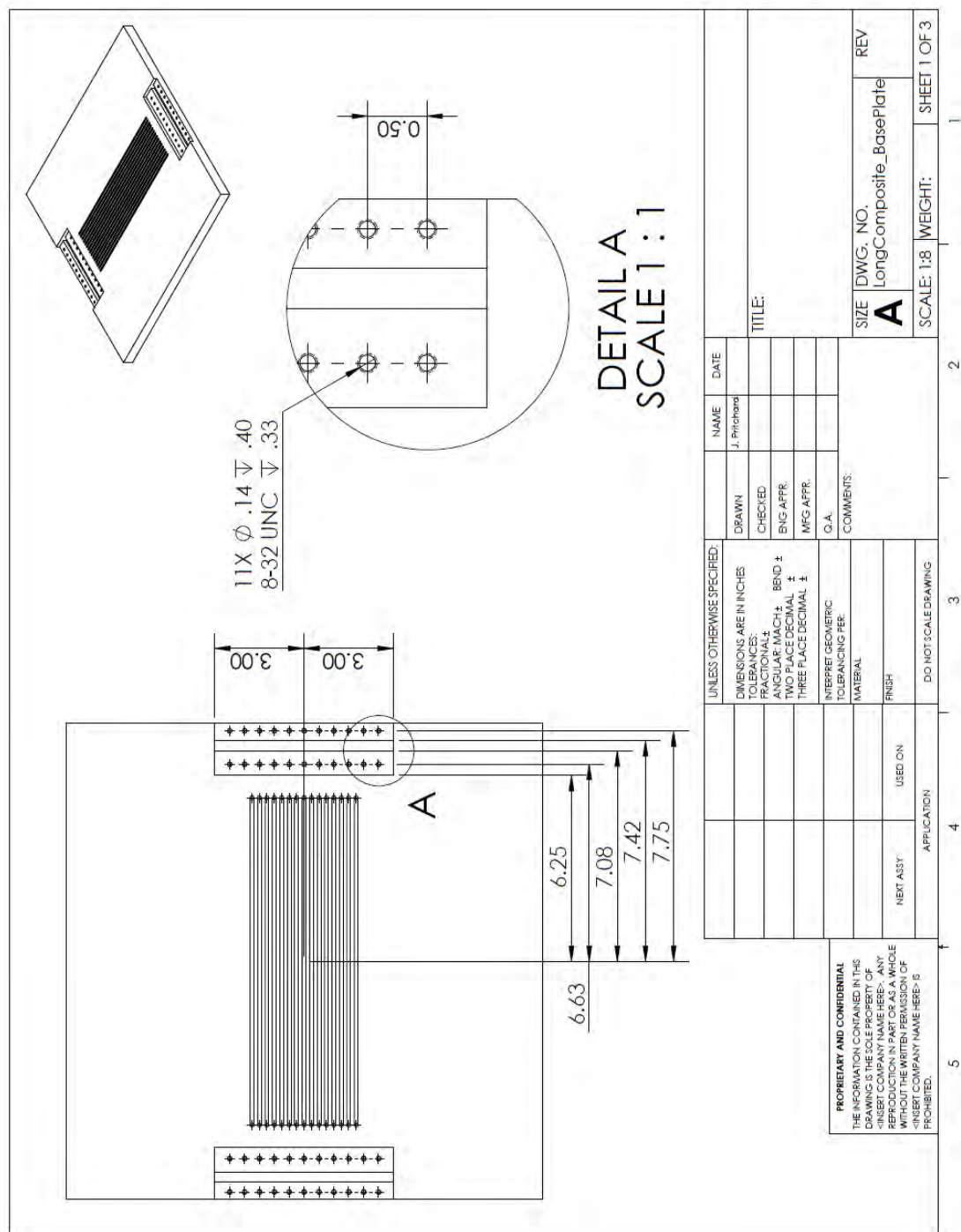


Figure B.3: Dimensional drawing of base plate for producing large geometry samples. Sheet 1 of 2.

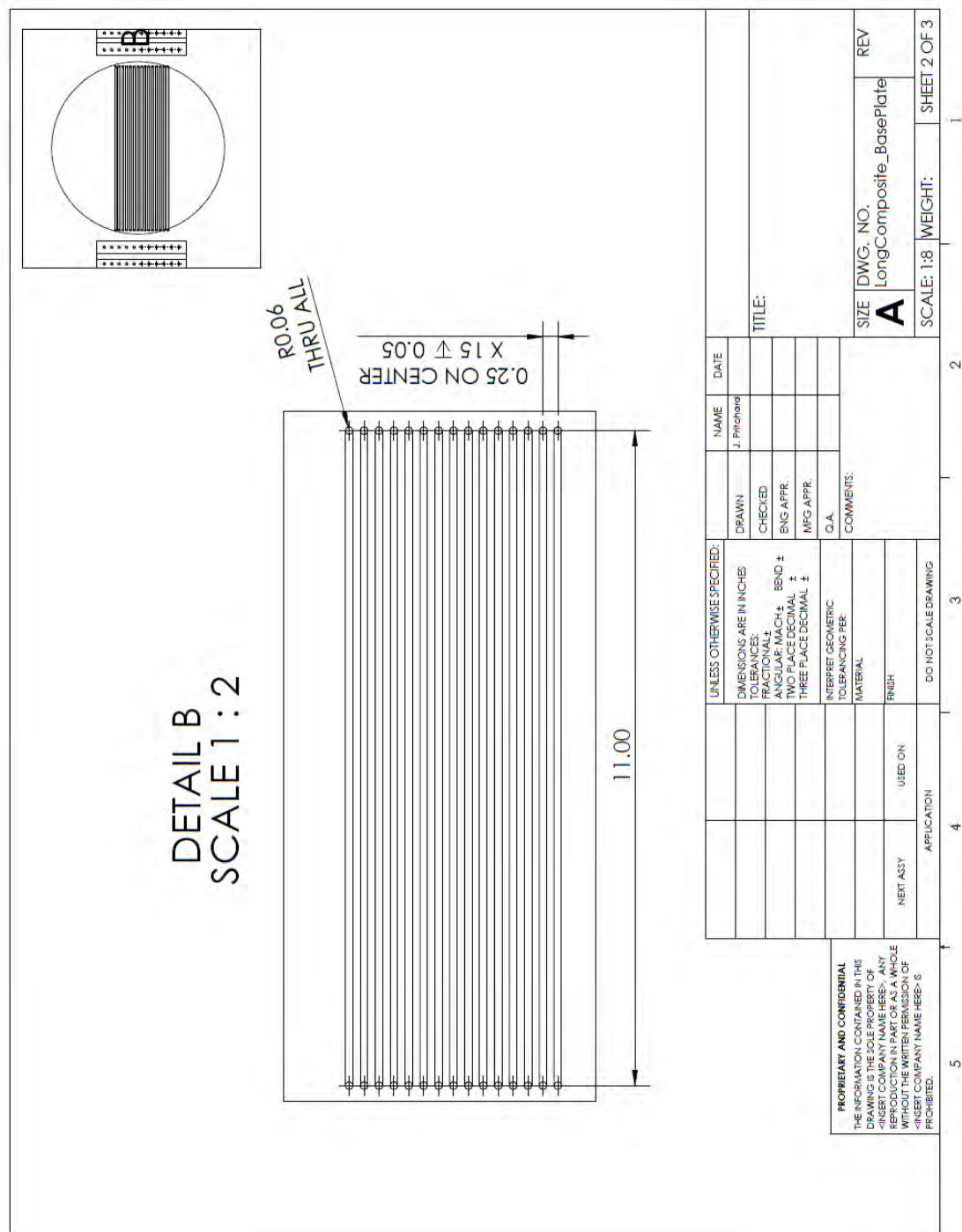


Figure B.4: Dimensional drawing of base plate for producing large geometry samples.
Sheet 2 of 2.

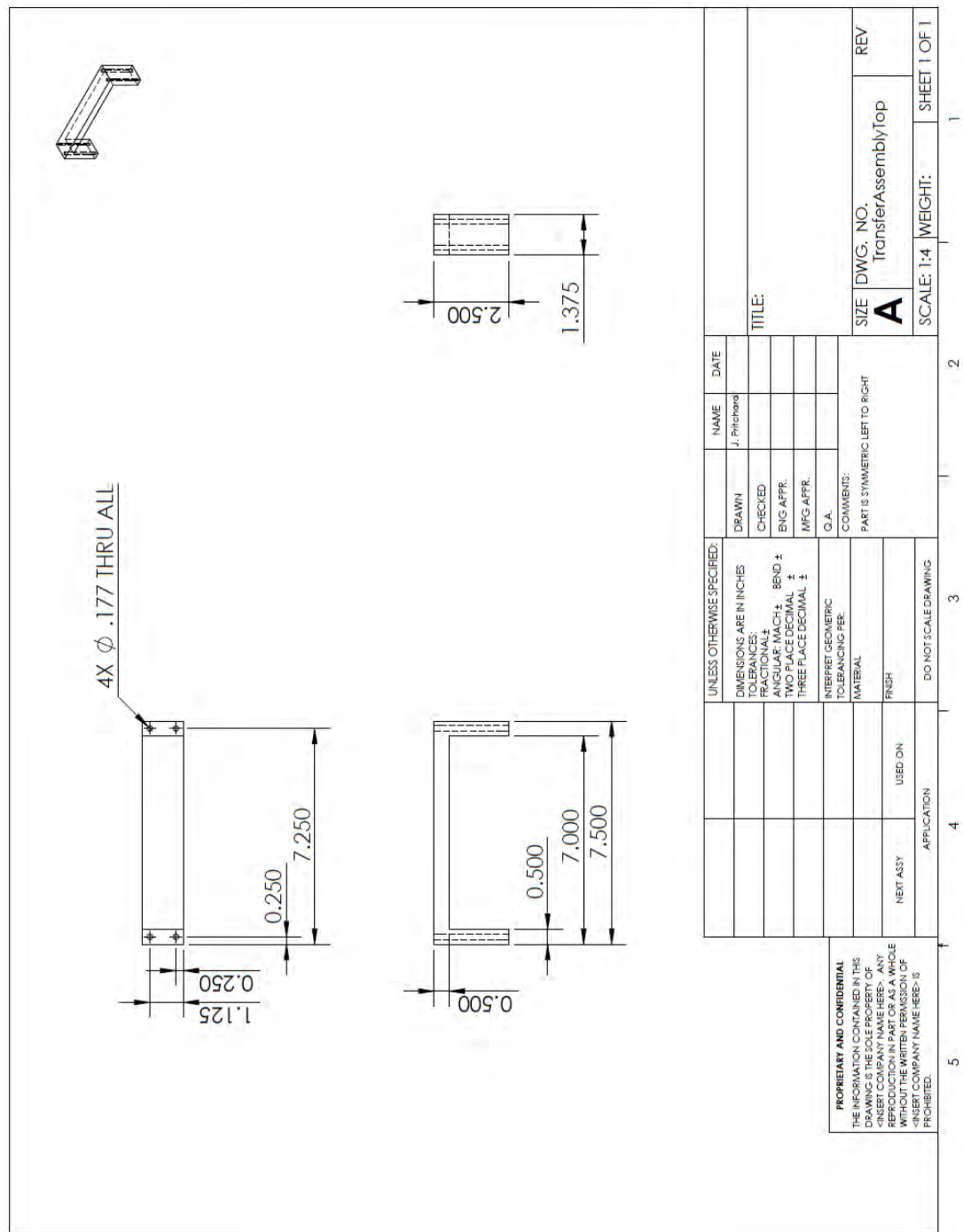


Figure B.5: Dimensional drawing of coupon size transfer assembly backbone.

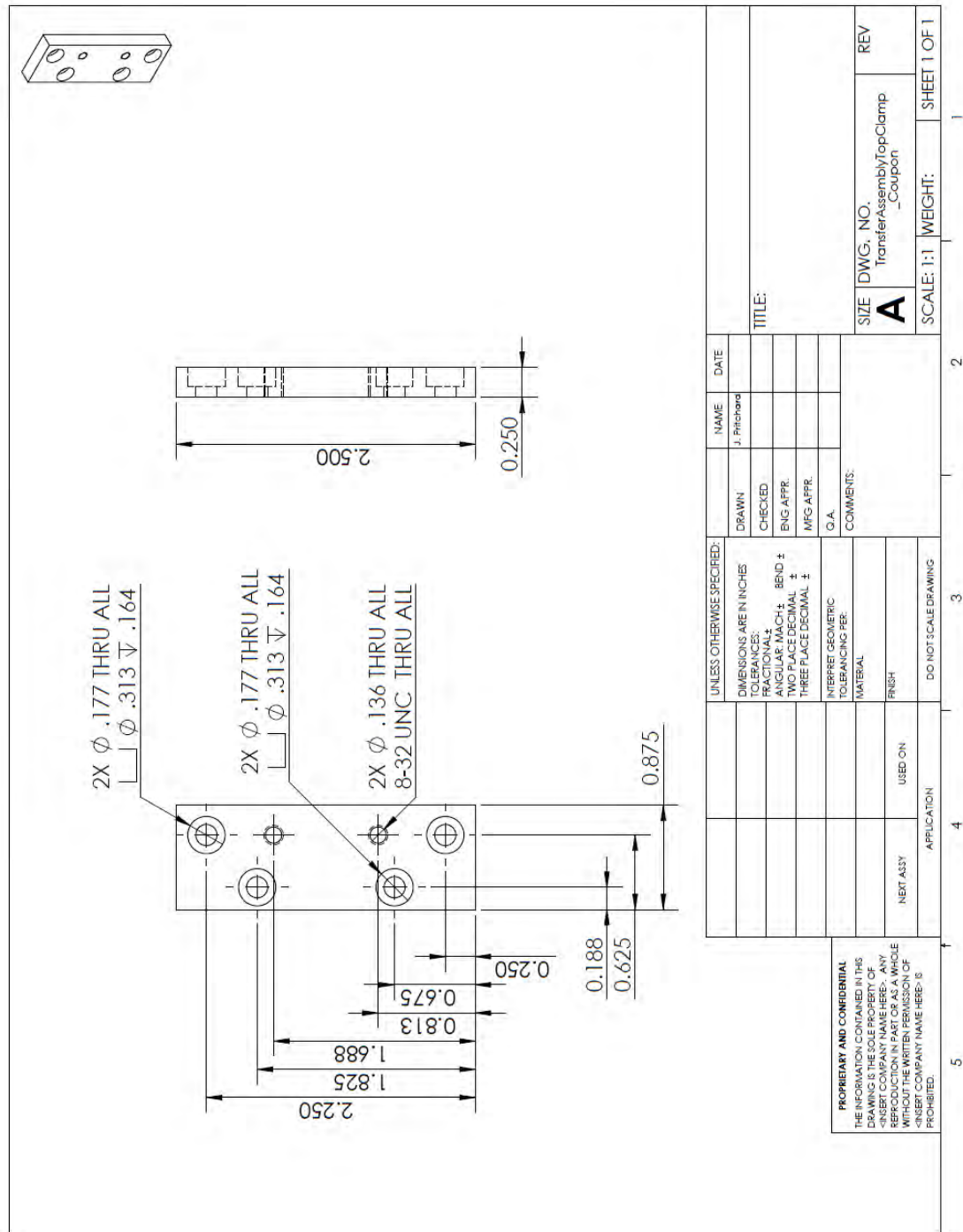


Figure B.7: Dimensional drawing of upper ribbon clamp used in coupon size transfer assembly.

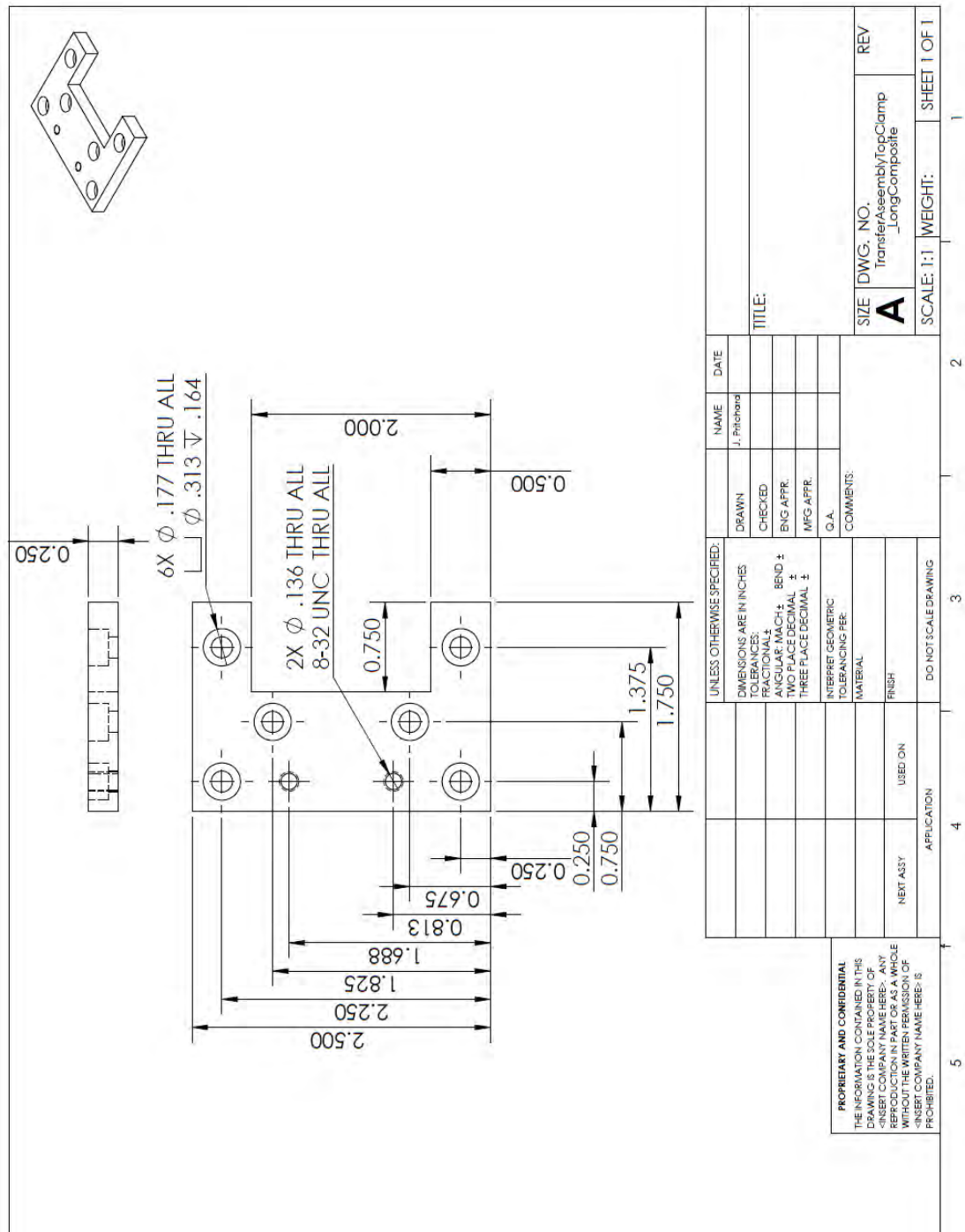


Figure B.8: Dimensional drawing of upper ribbon clamp used in large geometry transfer assembly.

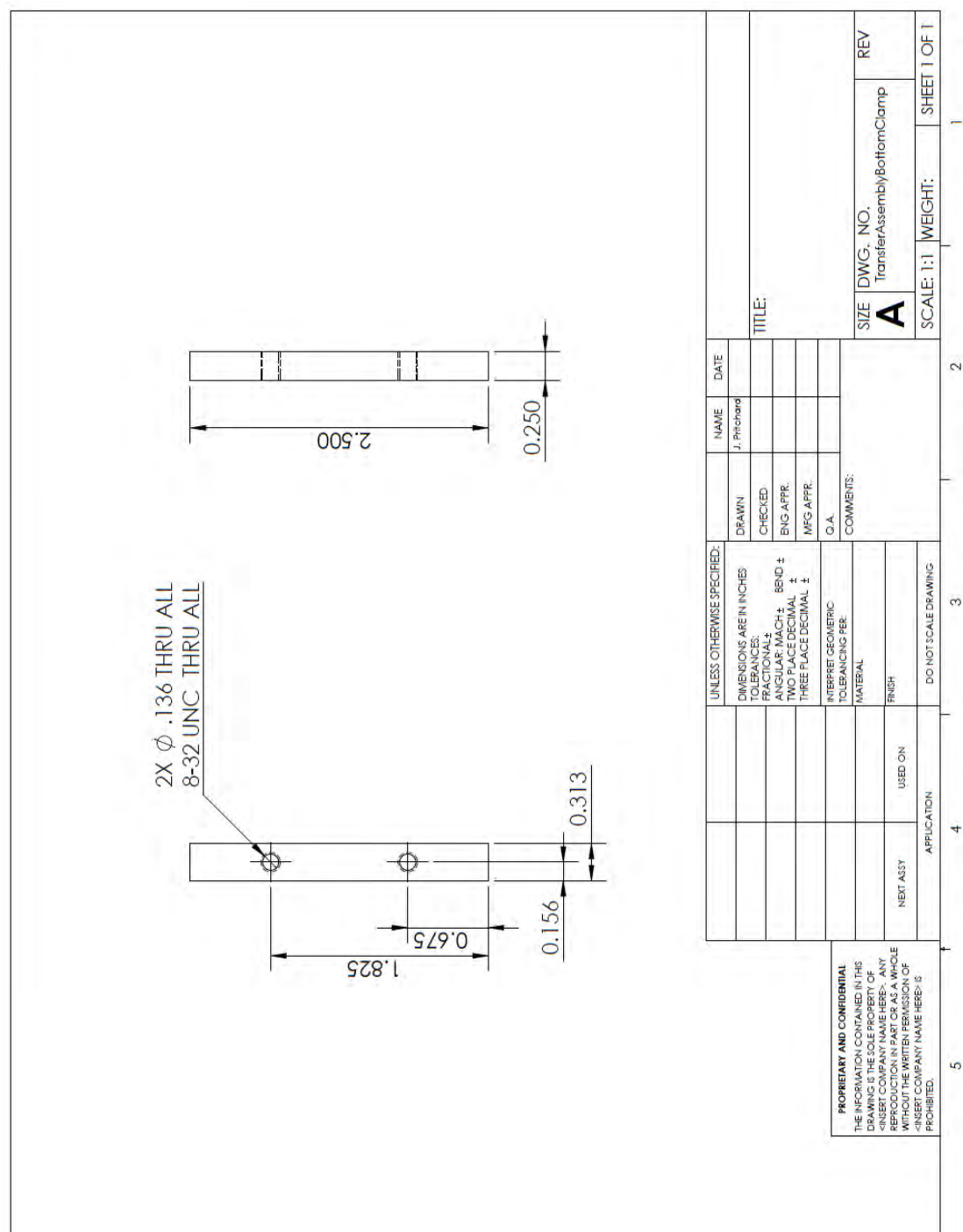


Figure B.9: Dimensional drawing of bottom ribbon clamp used in both coupon size and large geometry transfer assemblies.

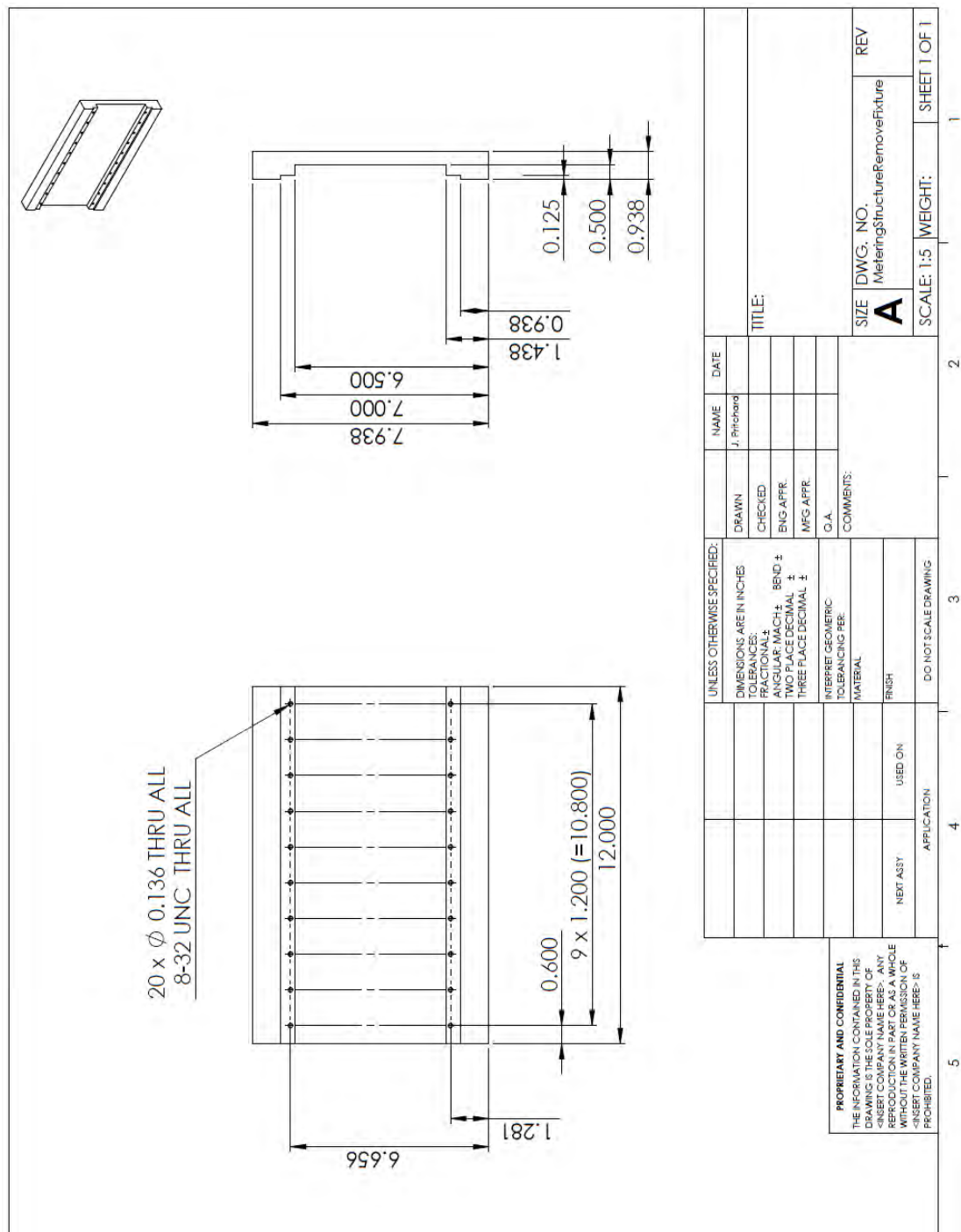


Figure B.10: Dimensional drawing of fixture design to assist in the removal of the build plate from the large geometry samples.

APPENDIX C

COEFFICIENT OF THERMAL EXPANSION TEST RESULTS

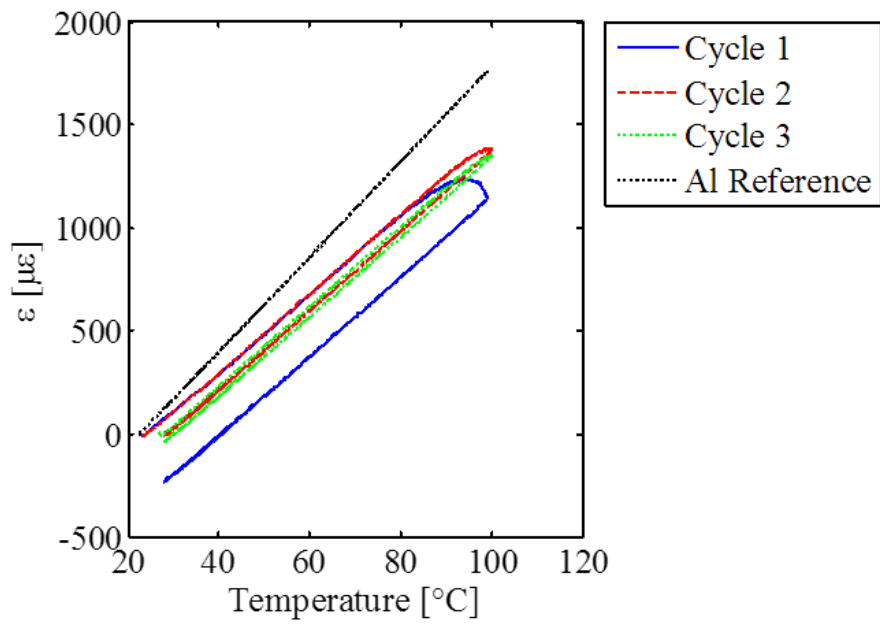


Figure C.1: Plot of strain versus temperature results for bottom strain gage during CTE test of P-1.

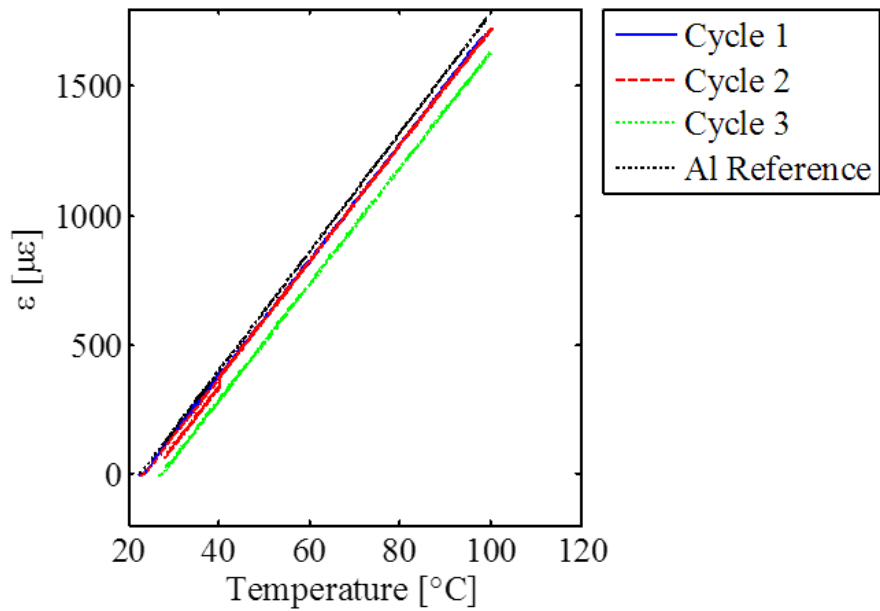


Figure C.2: Plot of strain versus temperature results for top strain gage during CTE test of P-1.

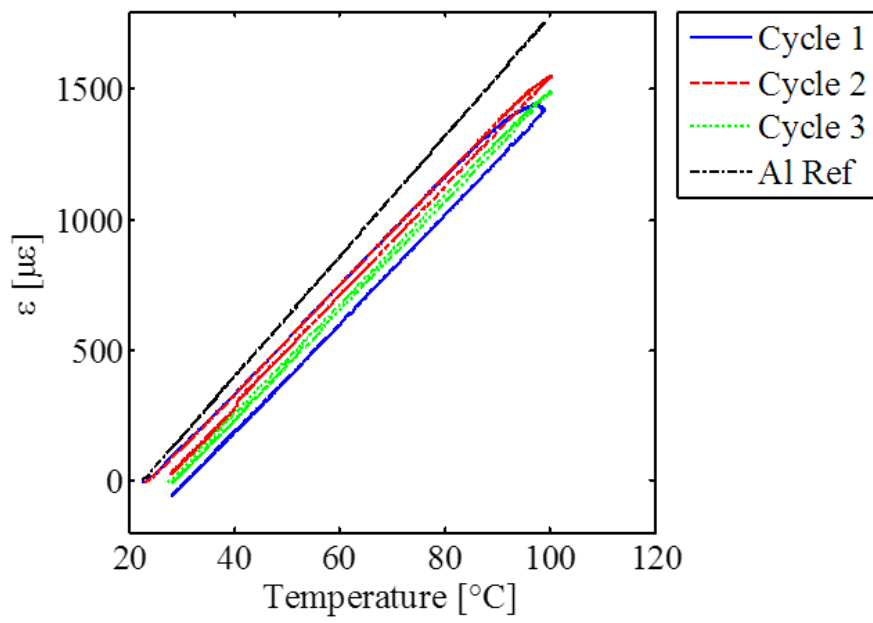


Figure C.3: Plot of the average strain versus temperature results from the CTE test of P-1.

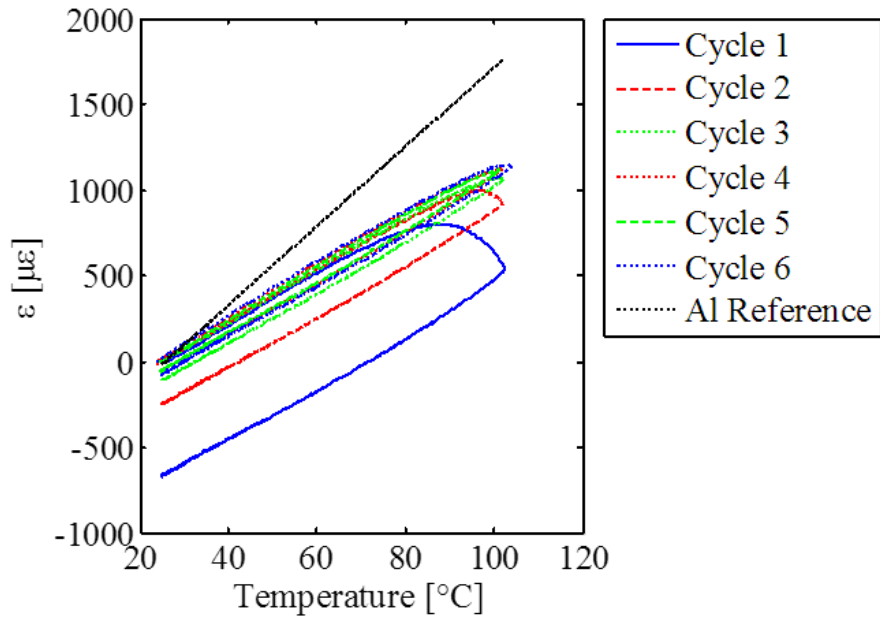


Figure C.4: Plot of strain versus temperature results for bottom strain gage during CTE test of P-2.

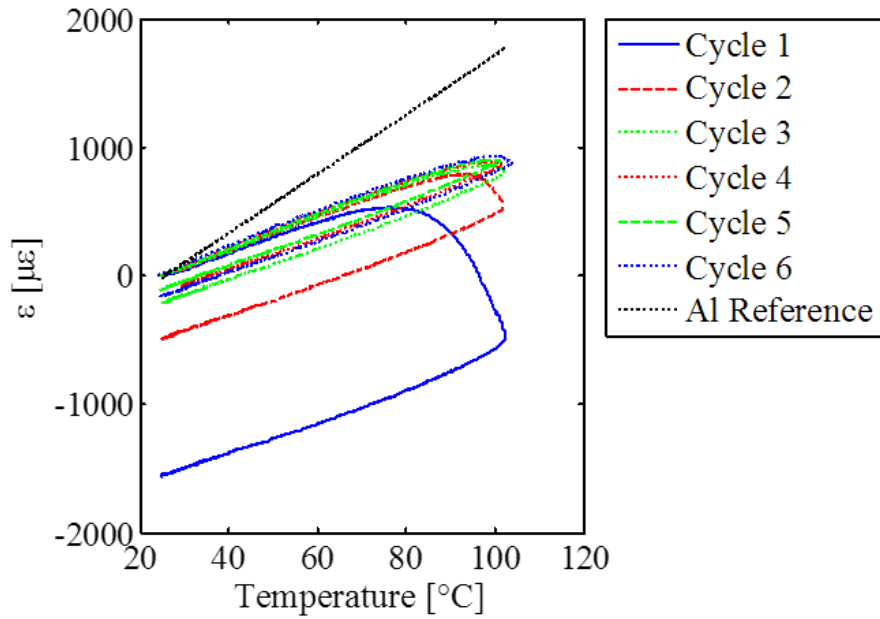


Figure C.5: Plot of strain versus temperature results for top strain gage during CTE test of P-2.

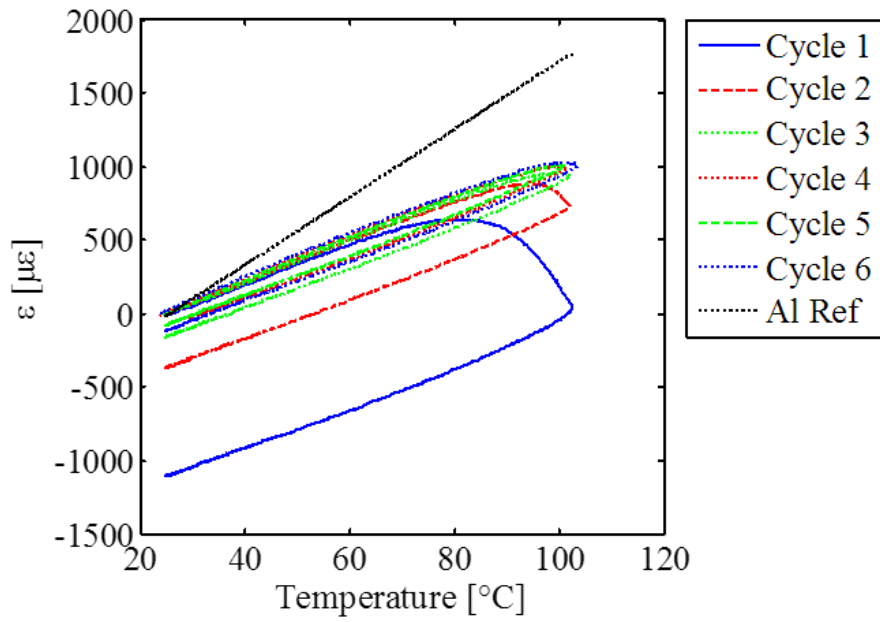


Figure C.6: Plot of the average strain versus temperature results from the CTE test of P-2.

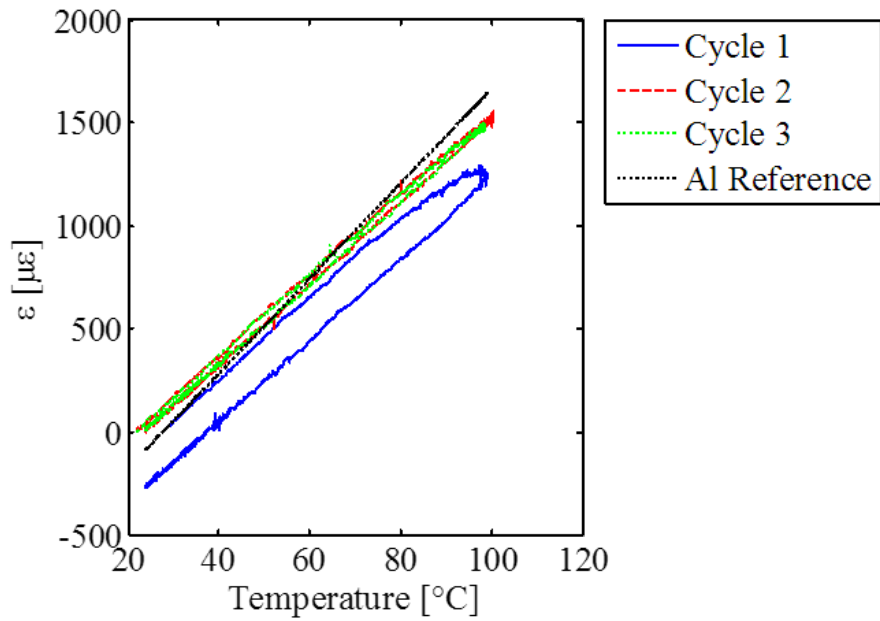


Figure C.7: Plot of strain versus temperature results for bottom strain gage during CTE test of P-4.

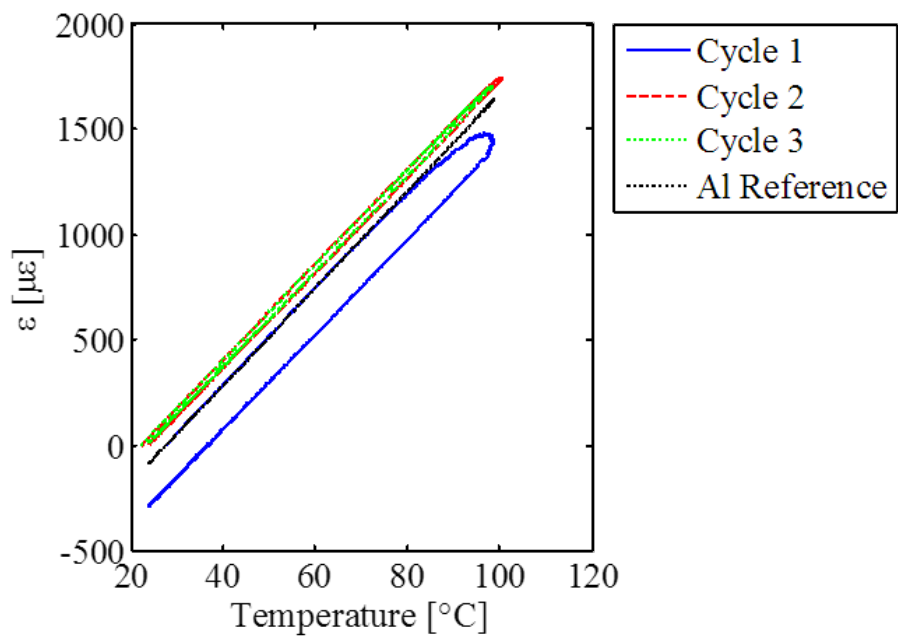


Figure C.8: Plot of strain versus temperature results for top strain gage during CTE test of P-4.

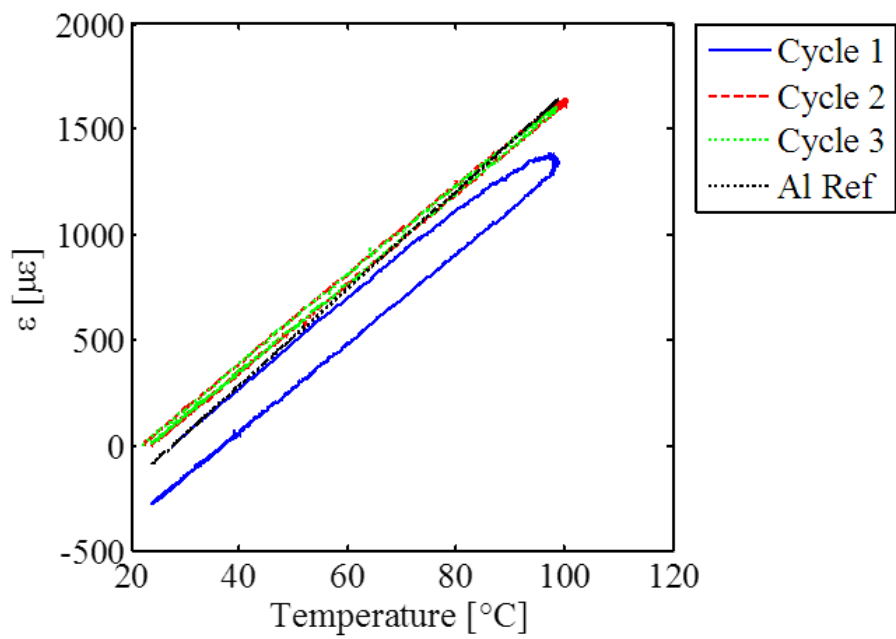


Figure C.9: Plot of the average strain versus temperature results from the CTE test of P-4.

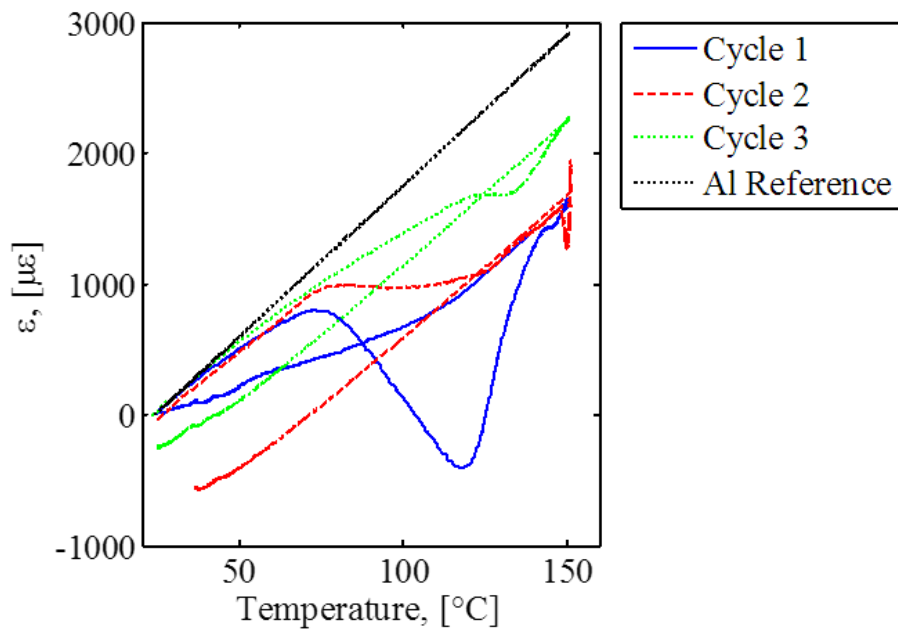


Figure C.10: Plot of strain versus temperature results for bottom strain gage during CTE test of C-7.

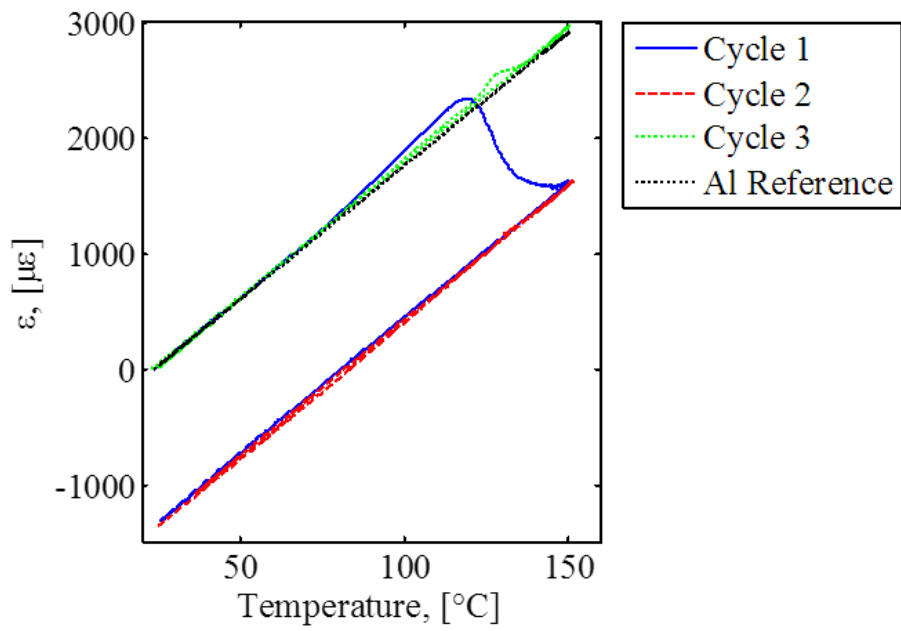


Figure C.11: Plot of strain versus temperature results for top strain gage during CTE test of C-7.

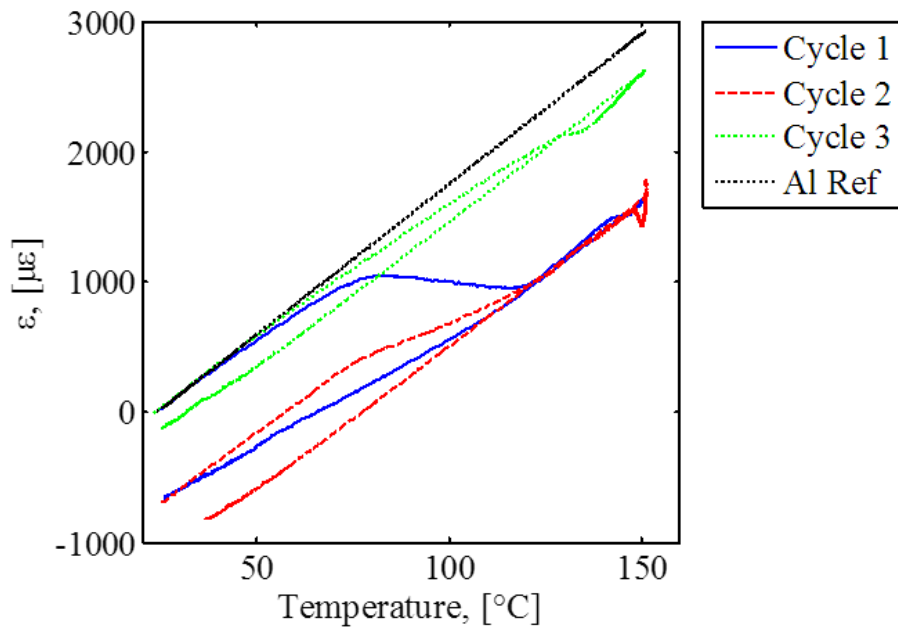


Figure C.12: Plot of the average strain versus temperature results from the CTE test of C-7.

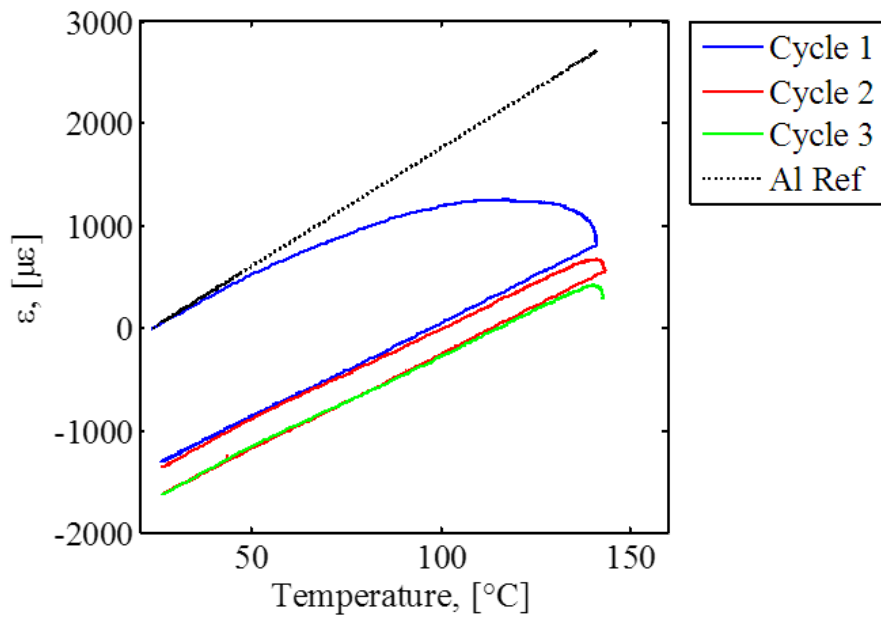


Figure C.13: Plot of strain versus temperature results for bottom strain gage during CTE test of C-9.

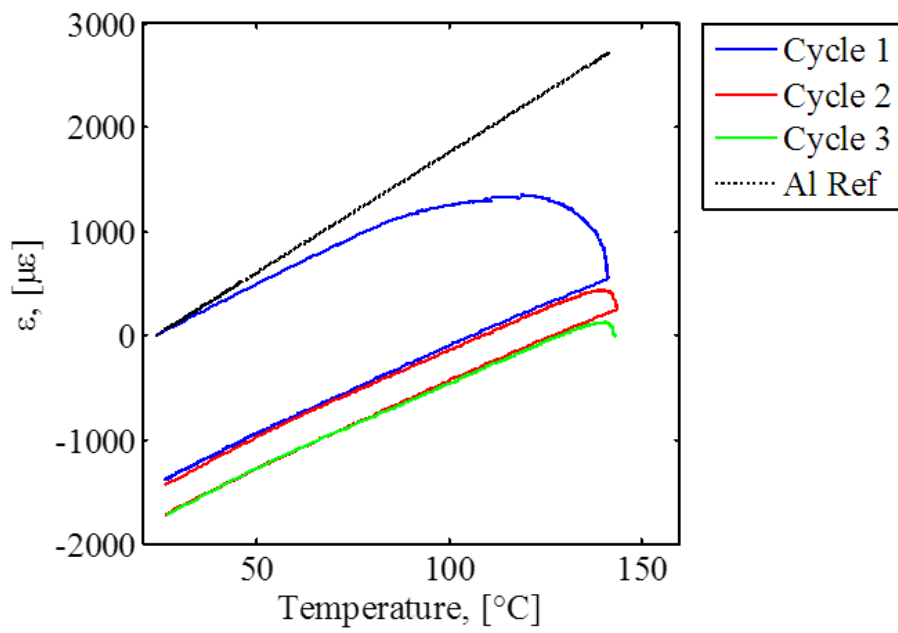


Figure C.14: Plot of strain versus temperature results for top strain gage during CTE test of C-9.

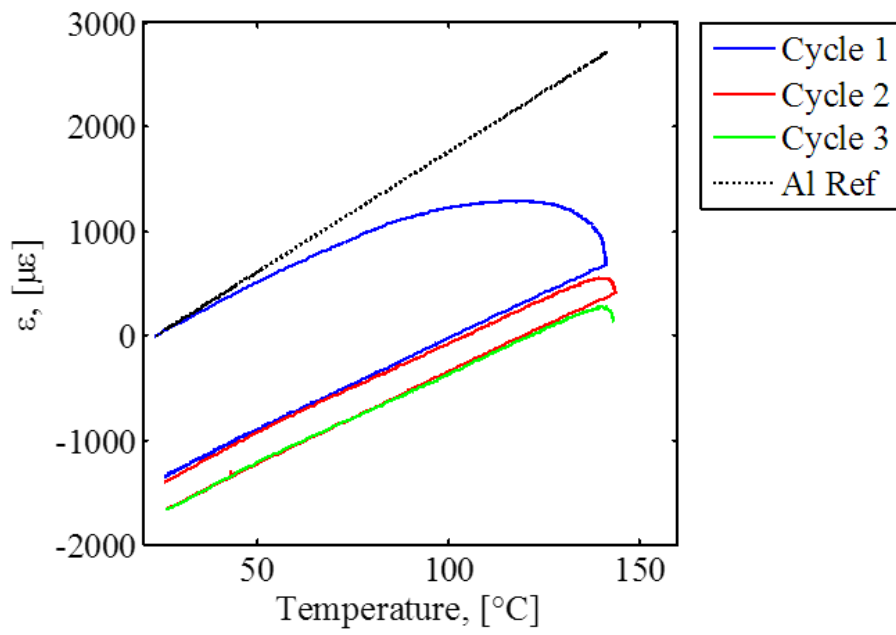


Figure C.15: Plot of the average strain versus temperature results from the CTE test of C-9.